UNIVERSITE D'AIX-MARSEILLE

ECOLE DOCTORALE: Physique et Science de la Mateière (ED 352)

LABORATOIRE LASER PLASMAS ET PROCEDES PHOTONIQUES

Thèse présentée pour obtenir le grade universitaire de docteur

Spécialité : Optique, Photonique et Traitment d'image

Artem DANILOV

Design, characterisation and biosensing applications of nanoperiodic plasmonic metamaterials

Soutenue le 11/04/2018 devant le Jury compose de :

HDR	Tatiana ITINA	Univ. Jean Monnet (France)	Rapporteur
Dr. habil.	Arkadi CHIPOULINE	TU Darmstadt (Germany) / Skoltech (Russia)	Rapporteur
HDR	Pierre-François BREVET	Univ. Claude Bernard Lyon 1 (France)	Président du Jury
HDR	Nicolas BONOD	Institute Fresnel, AMU (France)	Examinateur
IR	Igor OZEROV	CINaM, AMU (France)	Examinateur
HDR	Andrei KABASHIN	LP3, AMU (France)	Directeur de thèse
Prof.	Alexander GRIGORENKO	Univ. of Manchester (UK)	Co-Directeur de thèse

Numéro national de thèse/suffixe local : 2017AIXM0001/001ED62

Acknowledgement

I would like to thank Aix-Marseille Université and the whole LP3 collective for a wonderful 3 years of my life. Especially, my supervisor and head of this research, Prof. Andrei Kabashin for making this opportunity real. My colleagues Anton Popov and Ph.D. Gleb Tselikov for valuable endless discussions. I convey my gratitude to the co-director of this thesis, Prof. Alexander Grigorenko from Condensed Matter Physics group, University of Manchester. I owe a big thanks to my school physics teacher Dr. Sc. I. N. Gorbaty, who inspired my curiosity for nature investigations. I am indebted to Moscow Institute for Physics and Technology for my solid background and intensive training. I am grateful to my ex-colleagues from NT-MDT company for valuable constant communications and gained experience, especially to Igor Arkov, Sergey Mit'ko, Sergei Zayats and Ph.D. Dmitry Kozodaev.

And finally, I am immensely grateful to my parents Gennady and Elena for bringing me to this world and supporting my upbringing along with many relatives with a great unconditional support.

I also acknowledge AMIDEX foundation ("Académie d'Excellence" program, project "Plasmonic metamaterials for ultrasensitive biosensing", ANR-11-IDEX-0001-02) for financial support of this work and LASERLAB-EUROPE for granting me with collaboration trips to FORTH.

Contents

...the "paradox" is only a conflict

between reality

and your feeling of what reality "ought to be"

Richard Phillips Feynman

Introduction

First notable developments of optics were done in antiquity. Greek philosophers speculated about the nature of light and did first systematic studies on optics. Humanity discovered burning glasses and knew about reflection law. Legend says that Archimedes used his knowledge of light to create a reflective mirror weapon to destroy Roman ships during the siege of his hometown. Creation of lens (burning glass or magnifying glass) made a tremendous impact on optics, allowing one to enlarge optical image to dimensions which could be further detected and studied. This tool has been improved and advanced with time and technological progress. Even now modern optical microscopes zooming power is based on objectives – sets of lenses, designed and constructed specifically to enhance multiplication and avoid parasite effects such as aberrations, astigmatism etc. Microscopy is a very useful set of tools invented to study the world at scales which are too small to be examined by an unarmed eye. Antony van Leeuwenhoek[1] is one of the pioneers in microscopy, who was the first to observe red blood cells and bacteria. Microscopy deals with the light-matter interactions. To study the properties of any material, one should probe it by some other known substance. The smaller the size of used probe is, the better and more accurately one can measure properties of the material. The power of optics is based on several important advantages. The size of a light quanta, photon, is one of the smallest known objects. More importantly, energy of photon concludes the energy range of electronic and vibrational transitions in matter. These phenomena lie at the core of our abilities for visual perception and is the reason why experiments with light are very close to our intuition. Light is also fascinating because it manifests itself in the forms of waves and particles, especially in the optical scale. While long wavelength radiation (radiofrequencies, microwaves) is well described by wave theory, short wavelength radiation (X-rays) demonstrates mostly particle properties. These two worlds meet in the optical range. Classic light theory was mostly developed in the XVIII and XIX centuries, when concepts of polarization, diffraction and dispersion were introduced. Later, researchers understood that optical resolution cannot be improved infinitely. The resolution limitation arises when the probe size becomes comparable with the studied objects. The lower edge is set by the diffraction limit and it does not allow to focus light to dimensions smaller than roughly one half of the wavelength ($\sim$250 nm). This classic theory of resolution was formulated by Abbe and Rayleigh. However, new approaches have been developed to push further the diffraction limit (UV optics, confocal microscopy, light sheet microscopy) or to even break it (near-field microscopy).

Today we live in the Era of the nanoworld. During the last decade nanoscience and nanotechnology developed vastly, finding applications in many completely different fields. Originally driven by advantages of miniaturization and integration of electronic circuits for the computer industry, this approach is utilized everywhere now. Confocal fluorescence microscopy has become a key technology in biomedical research, while optical spectroscopy advanced to the levels that it become a powerful tool for different

material atomic and chemical structure identification. Nano-optics emerged as a new field, aimed to explain optical processes at nano-level. The field developed rapidly due to spectacular improvements in nanotechnology, helping to solve tasks for fabrication, manipulations and characterization at nanometer scales. The main aim of nano-optics is to extend optical techniques to length scales beyond the diffraction limit. Many techniques were developed for this purpose, including multiphoton microscopy, higher order harmonics generation, coherent anti-Stokes Raman spectroscopy (CARS). Another promising approach is based on near-field interactions. Near-field optical microscopy was originally introduced in 1928 by Synge[1], who proposed a device, in which a small aperture in an opaque plate is illuminated from one side and placed close to a sample surface. In this case, the illumination spot is limited by the size of the aperture rather than by diffraction. The transmitted light is then collected by a microscope and measured by a photoelectric cell. Moving the aperture over the surface one can create a sub-diffraction image of the sample. Synge's ideas did not attract attention during his life, but later they were reinvented and became a key point of near-field optical microscopy. Modern trend for near-field optics started in early 90s and was boosted by the introduction of such convenient experimental tools as STMs and AFMs, which enabled a high precision control of distance between a scattering probe and a sample. Applications of near-field optics soon covered a variety of areas, from fundamental physics and materials science to biology and medicine. Increased interest to near-field optics resulted in a creation of several independent research fields such as single-molecule spectroscopy or plasmonics.

The term plasmonics refers to the science and technology dealing with collective free electron oscillations in metals. The excitation of plasmons is accompanied by a dramatic localization and enhancement of the electromagnetic field, leading to a generation of a variety of new optical effects at the nanoscale with novel applications in nanoelectronics, optical imaging, biomedicine, telecommunications, photovoltaics, photocalalysis etc. As an example, one can excite surface plasmonic modes over a continuous metal/dielectric interface and the related free electron density charge waves are called surface plasmon polaritons (SPPs). In addition to surface plasmons, in other geometries such as metallic particles or voids of different topologies a different forms of electron plasma excitations are possible. These modes are called localized plasmons (LPs) and are characterized by resonance frequencies that depend on the size and shape of the object to which the plasmon is confined and its complex dielectric constant.

This thesis is related to the employment of plasmonics and plasmonic metamaterials for sensing applications. One of the approaches, developed for this aim is called optical transduction sensing, based on an idea that plasmonic effects are sensitive to the change of dielectric constant of adjacent media. By controlling the value of refractive index of the media near metal surface and studying the optical response of that system, one can quantify the amount of material on the metal surface. Particularly, implementation of such sensor in biosensing may be designed to track specific biomaterial by monitoring biological binding events between a target analyte (antigen, DNA) in analyzed volume and its selective receptor (antibody, DNA capture), fixed on the

sensor surface. Depending on an exact configuration of plasmonic structure, sensing capabilities may be enhanced to the levels there this approach becomes very competitive in a modern field of biosensing applications.

The thesis manuscript consists of 5 Chapters. Detailed description of involved phenomena and theoretical overview can be found in Chapter 1. Chapter 2 describes scientific equipment and instruments, which were used in this thesis. Chapter 3 represent the first part of my research devoted to the explanation and analysis of novel Plasmon Surface Lattice Resonances (PSLRs) over a nanoperiodic metamaterials based on arrays of Au nanoparticles. Conditions of excitation and properties of PSLR in direct and ATR geometries are studied in detail. It was also shown that the employment of these resonances in biosensing application dramatically improves the level of sensitivity profiting from phase properties of light and novel functionalities. A difference between classic SPR-based approach and a PSLR-based system is demonstrated by a detailed comparison of their sensitivity capabilities. Chapter 4 introduces a concept of 3D plasmonic metamaterial, based on a Ag covered woodpile-assembly-based photonic crystal. The results show a presence of new delocalized plasmonic mode, which enhances sensitivity capabilities. In contrast to 2D arrays, the spectral sensitivity in 3D arrays becomes independent on the period of the structure and is comparable with the sensitivity of the best plasmon transducers. Finally, Chapter 5 is devoted to the development of a tool, based on an apertureless Scanning Near-Field Optical Microscopy (aSNOM) for direct visualization of near-field propagation from plasmonic nanostructures. This information can be used to enable Surface Enhanced Raman Spectroscopy (SERS) as a parallel channel, in addition to the optical transduction sensing platform.

Chapter 1

Theoretical and literature background

CONTENTS

1.1 Electromagnetism

Despite dual wave-particle nature of the light, optical properties at nano-level can be described mostly via wave theory based on Maxwell's equations. Each of these equations follows from a direct experimental observation of some physical phenomena. Discovered by a group of independent researchers and then assembled by Maxwell into a single set, these equations present a solid description of electromagnetism:

$$\nabla \cdot \mathbf{D} = \rho \tag{1.1a}$$
$$\nabla \cdot \mathbf{B} = 0 \tag{1.1b}$$
$$\nabla \times \mathbf{E} = -\frac{\partial \mathbf{B}}{\partial t} \tag{1.1c}$$
$$\nabla \times \mathbf{H} = \mathbf{j} + \frac{\partial \mathbf{D}}{\partial t} \tag{1.1d}$$

where **E** stands for the electric field, **D** the electric displacement, **H** the magnetic field, **B** the magnetic induction, **j** the current density, and ρ the charge density. ε_0 and μ_0 are permittivity and permeability of vacuum, respectively. The concept of fields was introduced to explain the transmission of forces from a source to a receiver. Fields cannot be measured directly, but they can be detected by effects they produce. Forces are physical observables, while the fields are definitions introduced to explain the problem of the "action at a distance". Since light demonstrates both particle and wave properties, it is logical to search for a suitable solution based on a form of known wave equation. Classic one-dimensional wave equation has a view of:

$$\frac{\partial^2}{\partial x^2} = \frac{1}{a^2}\frac{\partial^2}{\partial t^2} \tag{1.2}$$

where *a* is some constant, related to speed of propagation. By introducing $\Delta = \nabla \cdot \nabla = \nabla^2 = \frac{\partial^2}{\partial x^2} + \frac{\partial^2}{\partial y^2} + \frac{\partial^2}{\partial z^2}$, the required equation for electric field in three-dimensional space is transformed into:

$$\nabla^2 = \frac{1}{a^2}\frac{\partial^2}{\partial t^2} \tag{1.3}$$

Taking into account that $\nabla \times \nabla \times \mathbf{E} = \nabla(\nabla \cdot \mathbf{E}) - \nabla^2 \mathbf{E}$, calculating $\nabla \times \nabla \times \mathbf{E}$ and combining with other Maxwell's equations, one can derive the light wave equation:

$$\nabla^2 \boldsymbol{E} = \frac{1}{c^2}\frac{\partial^2 \mathbf{E}}{\partial t^2} \tag{1.4}$$

where $c = \frac{1}{\sqrt{\varepsilon_0 \mu_0}}$ is a speed of light in free space. The solution of this differential equation linking space and time appears to be a monochromatic wave:

$$\boldsymbol{E}(\boldsymbol{r}, t) = \boldsymbol{E}(\boldsymbol{k}, \omega) e^{i(\boldsymbol{kr} - \omega t)} \tag{1.5}$$

where $\boldsymbol{k}$ – wave vector and ω - an angular frequency. By using this solution in wave equation, one can obtain an intrinsic relation of these two parameters in form of $\boldsymbol{k} = \frac{\omega}{c}$ for a free vacuum wave propagation. Substituting the expression (1.5) for monochromatic wave into the wave equation (1.4), one can obtain Helmholtz equation:

$$\nabla^2 \boldsymbol{E} + \boldsymbol{k}^2 \varepsilon \boldsymbol{E} = 0 \tag{1.6}$$

Maxwell's equations deal with the fields generated by currents and charges in matter, but the origin of these charges and currents is not described. In order to have a self-consistent solution for the electromagnetic field theory, Maxwell's equations must be completed by relations that describe the behaviour of matter under the influence of these fields. These material-related equations are known as constitutive relations. For a non-dispersive linear and isotropic medium they are:

$$\mathbf{D} = \varepsilon \, \varepsilon_0 \mathbf{E} \tag{1.7a}$$
$$\mathbf{B} = \mu \, \mu_0 \mathbf{H} \tag{1.7b}$$

where ε and μ are electric permittivity and magnetic permeability of the medium, respectively. In addition, it is important to describe the property of materials to compensate for external electromagnetic perturbations with **P** – polarizability and **M** – magnetization in a form of:

$$\mathbf{D} = \varepsilon_0 \mathbf{E} + \mathbf{P} \tag{1.8a}$$
$$\mathbf{H} = \frac{1}{\mu_0} - \mathbf{M} \tag{1.8b}$$

In optical regime, $\mu = \mathbf{1}$ for all known natural materials[2], which enables one to simplify related equations correspondingly. Macroscopic optical properties of any material in general and metals in particular could be therefore described by a complex $\varepsilon(\boldsymbol{k}, \omega)$.

1.2 Optics of Metals

The interactions of metals with electromagnetic fields are well described by a classic approach based on Maxwell's equations. This description can be applied even for a few nanometer sized metallic nanostructures without addressing to quantum mechanics. For a wide range of frequencies metal optical responses are well explained by a model of free electron plasma (also known as Drude model) due to a high number of unbound electrons[3]. This approach ignores properties of material inner structure by substituting the real electron mass for an effective m_e. When a harmonic electromagnetic wave is applied, those electrons start to oscillate in response. Electron motion is damped[4] due to mutual electron collisions, electron-phonon interactions and scattering from structural lattice defects or grain boundaries and can be expressed as:

$$-\mathrm{e}\mathbf{E} = \mathrm{m}_e \frac{\partial^2 \mathbf{r}}{\partial t^2} + \mathrm{m}_e \gamma \frac{\partial \mathbf{r}}{\partial \mathrm{t}} \tag{1.9}$$

where γ is a characteristic collision frequency, which is inversely proportional to time of free electron gas relaxation $\gamma = \frac{1}{\tau}$. The solution for this equation will be:

$$\boldsymbol{r} = \frac{\mathrm{e}\mathbf{E}}{\mathrm{m}_e(\omega^2 + i\omega\gamma)} \tag{1.10}$$

By inserting macroscopic polarization $P=-n_e e\boldsymbol{r}$ into the equation for dielectric displacement (1.7a), one can obtain following result:

$$\boldsymbol{D} = \varepsilon_0 \left(1 - \frac{\omega_p^2}{\omega^2 + i\omega\gamma}\right)\mathbf{E} \tag{1.11}$$

with the corresponding permittivity of ideal Drude metal:

$$\varepsilon_{FEG}(\omega) = 1 - \frac{\omega_p^2}{\omega^2 + i\omega\gamma} = \left[1 - \frac{\omega_p^2 \tau^2}{\tau^2\omega^2 + 1}\right] + i\left[\frac{\omega_p^2 \tau}{\omega(\tau^2\omega^2 + 1)}\right] \tag{1.12}$$

where $\omega_p^2 = \frac{\mathrm{n}_e e^2}{\varepsilon_0 \mathrm{m}_e}$ is a free electron gas plasma frequency. For real metals Drude free electron gas description is quite accurate for $\omega \ll \omega_p$ and $\omega \ll \gamma$. For larger frequencies $\omega \leq \omega_p$, $\varepsilon(\omega)$ becomes mostly real and no damping occurs. For most metals the density of free charge carriers n_e and their effective mass m_e differ insignificantly and the spectral position of ω_p lies in ultraviolet region. Alkali metals demonstrate good correlation with Drude theory, however for noble metals it fails already at visible frequencies due to the presence of interband transitions. As a result, gold possesses such a fascinating yellow colour, perceptible to human eye. Such a colour contrasts with spectrally uniform grey shades of silver, which looks more suitable for plasmonic effects in the visible range,

showing no losses. However, applications of silver are limited due to its strong oxidation and relatively high reactivity.

In order to consider interband electron transition, Drude theory was modified by Lorentz, who introduced a concept of harmonic oscillator into the motion equation:

$$-e\mathbf{E} = m_e^* \frac{\partial^2 \mathbf{r}}{\partial t^2} + m_e^* \gamma^* \frac{\partial \mathbf{r}}{\partial t} + \alpha \mathbf{r} \tag{1.13}$$

where α is a *spring* or "restoring force constant" of the potential that holds bound electron. m_e^* and γ^* are bound electron effective mass and damping constant, respectively. The resulting contribution of bound electrons can be expressed similarly to (1.12):

$$\varepsilon_{BE}(\omega) = 1 + \frac{\omega_p^{*2}}{(\omega_0^2 - \omega^2) - i\omega\gamma^*} = \left[1 + \frac{\omega_p^{*2}(\omega_0^2 - \omega^2)}{(\omega_0^2 - \omega^2)^2 + \gamma^{*2}\omega^2}\right] + i\left[\frac{\gamma^* \omega \omega_p^{*2}}{(\omega_0^2 - \omega^2)^2 + \gamma^{*2}\omega^2}\right] \tag{1.14}$$

where $\omega_p^{*2} = \frac{n_e^* e^2}{\varepsilon_0 m_e^*}$, n_e^* is a density of the bound electrons and $\omega_0 = \sqrt{\frac{\alpha}{m_e^*}}$.

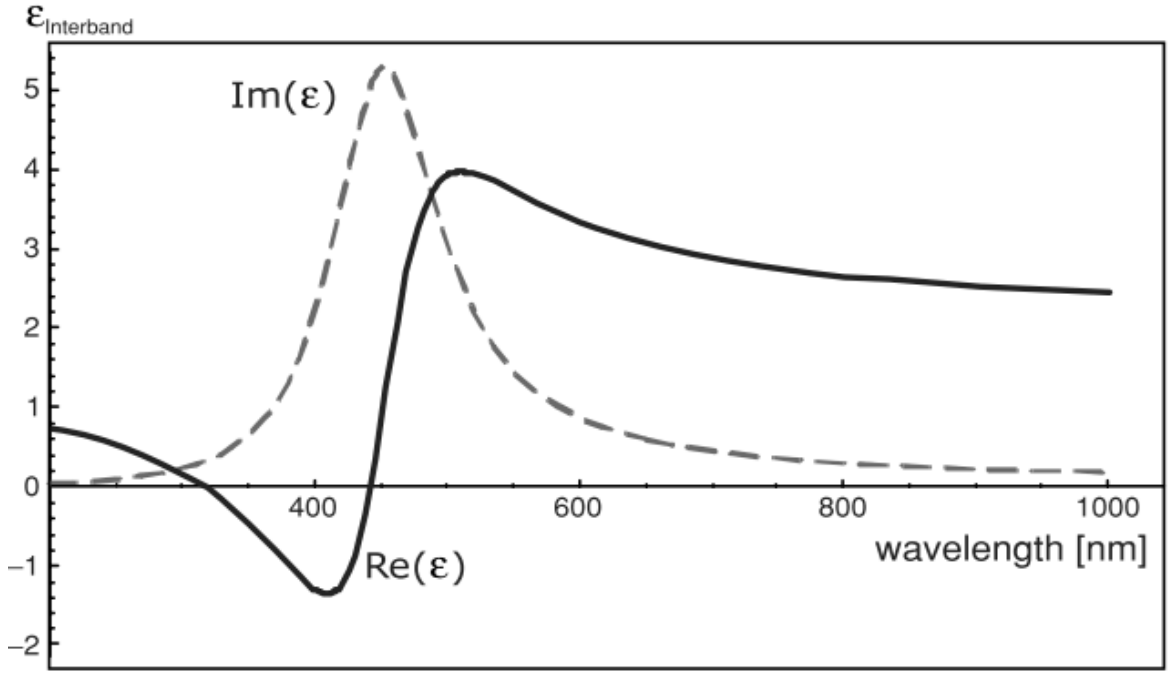

Fig. 1.1 Contribution of the interband transition to the dielectric function of Au. The solid and dashed lines correspond to real and imaginary parts, respectively.
Adopted from ref. [1]

Clear resonance behaviour is shown for imaginary part curve on Fig. 1.1, corresponding to the impact of interband transition. This theory modification is indeed in a good accordance with experimental data. However, it still fails to reproduce dielectric function adequately for the region of higher-energy interband transitions as only a single transition is taken into account.

1.3 Plasmons: bulk plasmons, SPP, LSPR

As was mentioned before, plasmon is a quantum of charge oscillations. Normally, plasmons are somehow excited by some coupling mechanism with an electromagnetic wave or by other plasmonic mode interplay. The majority of the plasmons can be divided into three main groups. First, the bulk plasmon corresponds to a cooperative longitudinal in-phase electron oscillation at plasma frequency – a direct analogue of ideal gas plasma from thermodynamics. Second, the surface plasmon-polariton, which manifests itself as a fading (evanescent) wave, propagating along a flat metal-dielectric interface. And finally, the localized surface plasmon, resulting from an electron cloud oscillation of size-confined metallic object.

1.3.1 Surface plasmon resonance

Surface plasmon polaritons are electromagnetic excitations propagating at the interface between a dielectric and a conductor, evanescently confined in the perpendicular direction. These electromagnetic surface waves arise via coupling of electromagnetic field to oscillations of the conductor's electron plasma[3]. Surface plasmon polaritons can only exist at the interface between a positive-permittivity medium and a negative-permittivity medium. The positive-permittivity medium, often called the dielectric material, can be any transparent material such as air or (for visible light) glass. The negative-permittivity medium, often called the plasmonic medium, may be a

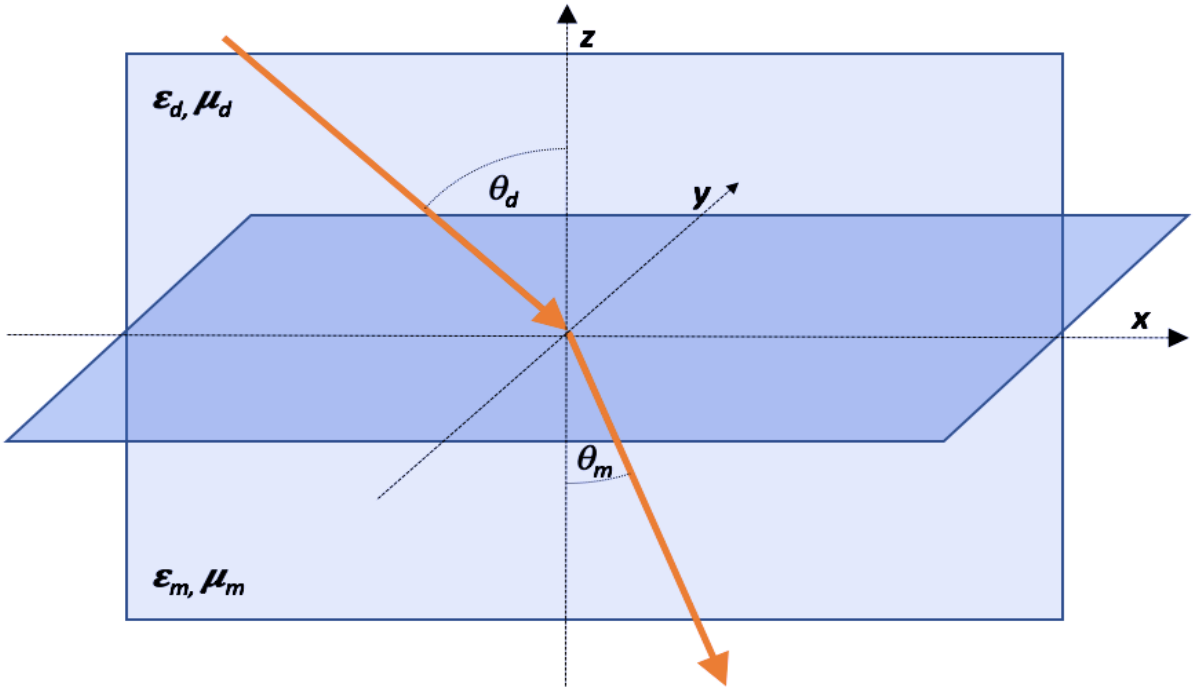

Fig. 1.2 Schematic representation of metal/dielectric interface and refracted wave on it. The interface is defined by Z=0.

metal or other material[4]. Among natural materials only metals and some doped semiconductors[2] possess plasmonic properties in the visible and near-infrared region, due to the abundance of free electrons which leads to a high plasma frequency.

Assume the conditions (Fig. 1.2) when a monochromatic electromagnetic wave propagating in XZ-plane falls on aligned to XY-plane interface of metal/dielectric at Z = 0. Each half-space has uniform ε distribution, thus $\varepsilon(\boldsymbol{r}) = \varepsilon(z)$. SPP propagating wave therefore can be described as $\mathbf{E}(x, y, z, t) = \mathbf{E}(z)e^{i\beta x}$, where $\beta = k_0$ is its propagation. Substituting this expression into Helmholtz equation (1.6), one can get a simplified base equation for SPP:

$$\frac{\partial^2 \mathbf{E(z)}}{\partial z^2} + (k_0^2 - \beta^2)\boldsymbol{E} = 0 \tag{1.15}$$

Resolving differential part directly through Maxwell equations (1.1c and 1.1d) and substituting $\frac{\partial}{\partial t} \rightarrow -i\omega$ due to harmonic time dependence, following set of equations can be obtained:

$$\frac{\partial E_z}{\partial y} - \frac{\partial E_y}{\partial z} = i\omega\mu_0 H_x \tag{1.16a}$$
$$\frac{\partial E_x}{\partial z} - \frac{\partial E_z}{\partial x} = i\omega\mu_0 H_y \tag{1.16b}$$
$$\frac{\partial E_y}{\partial x} - \frac{\partial E_x}{\partial y} = -i\omega\mu_0 H_z \tag{1.16c}$$
$$\frac{\partial H_z}{\partial y} - \frac{\partial H_y}{\partial z} = -i\omega\varepsilon\,\varepsilon_0 E_x \tag{1.16d}$$
$$\frac{\partial H_x}{\partial z} - \frac{\partial H_z}{\partial x} = -i\omega\varepsilon\,\varepsilon_0 E_y \tag{1.16e}$$
$$\frac{\partial H_y}{\partial x} - \frac{\partial H_x}{\partial y} = -i\omega\varepsilon\,\varepsilon_0 E_z \tag{1.16f}$$

Taking into account that the axes are chosen in a way that the wave propagates only in x-direction, one can simplify the set of the equation using $\frac{\partial}{\partial x} \rightarrow i\beta$ and $\frac{\partial}{\partial y} \rightarrow 0$:

$$\frac{\partial E_y}{\partial z} = -i\omega\mu_0 H_x \tag{1.17a}$$
$$\frac{\partial E_x}{\partial z} - i\beta E_z = i\omega\mu_0 H_y \tag{1.17b}$$
$$i\beta E_y = i\omega\mu_0 H_z \tag{1.17c}$$
$$\frac{\partial H_y}{\partial z} = i\omega\varepsilon\,\varepsilon_0 E_x \tag{1.17d}$$
$$\frac{\partial H_x}{\partial z} - i\beta H_z = -i\omega\varepsilon\,\varepsilon_0 E_y \tag{1.17e}$$
$$i\beta H_y = -i\omega\varepsilon\,\varepsilon_0 E_z \tag{1.17f}$$

Two possible self-consistent solutions of the system correspond to TE (for non-zero $H_x, H_z \; and \; E_y$) and TM (for non-zero E_x, E_z and H_y) modes, with wave equations respectively:

$$\frac{\partial^2 E_y}{\partial z^2} + (k_0^2 \varepsilon - \beta^2) E_y = 0 \tag{1.18a}$$

$$\frac{\partial^2 H_y}{\partial z^2} + (k_0^2 \varepsilon - \beta^2) H_y = 0 \tag{1.18b}$$

Now one can separate TM solution equations for dielectric half-space (Z > 0):

$$H_y(z) = A_d e^{i\beta x} e^{-k_d z} \tag{1.19a}$$

$$E_x(z) = i A_d \frac{1}{\omega \, \varepsilon_0 \varepsilon_d} k_d e^{i\beta x} e^{-k_d z} \tag{1.19b}$$

$$E_z(z) = -A_m \frac{\beta}{\omega \, \varepsilon_0 \varepsilon_d} e^{i\beta x} e^{-k_d z} \tag{1.19c}$$

from metallic half-space (Z < 0):

$$H_y(z) = A_m e^{i\beta x} e^{k_m z} \tag{1.20a}$$

$$E_x(z) = -i A_m \frac{1}{\omega \, \varepsilon_0 \varepsilon_m} k_m e^{i\beta x} e^{-k_m z} \tag{1.20b}$$

$$E_z(z) = -A_m \frac{\beta}{\omega \, \varepsilon_0 \varepsilon_m} e^{i\beta x} e^{-k_m z} \tag{1.20c}$$

Continuity of H_y and H_x for z = 0 means $A_d = A_m$ and $k_m \varepsilon_d = -k_d \varepsilon_m$. Inserting $H_y(z)$ into the wave equation (1.18b), following relations can be obtained:

$$k_d^2 = \beta^2 - k_0^2 \varepsilon_d \tag{1.21a}$$

$$k_m^2 = \beta^2 - k_0^2 \varepsilon_m \tag{1.21b}$$

which leads us to the main result of calculations – SPP dispersion relation:

$$\beta = k_0 \sqrt{\frac{\varepsilon_m \varepsilon_d}{\varepsilon_m + \varepsilon_d}} \tag{1.22}$$

Performing the same manipulations for TE mode, it is easy to find that continuity of E_y and H_x leads to $A_d = A_m$ and $A_d(k_m + k_d) = 0$, which is possible only for $A_d = A_m = 0$. This means that SPP mode exist uniquely for TM polarization.

1.3.2 SPP excitation

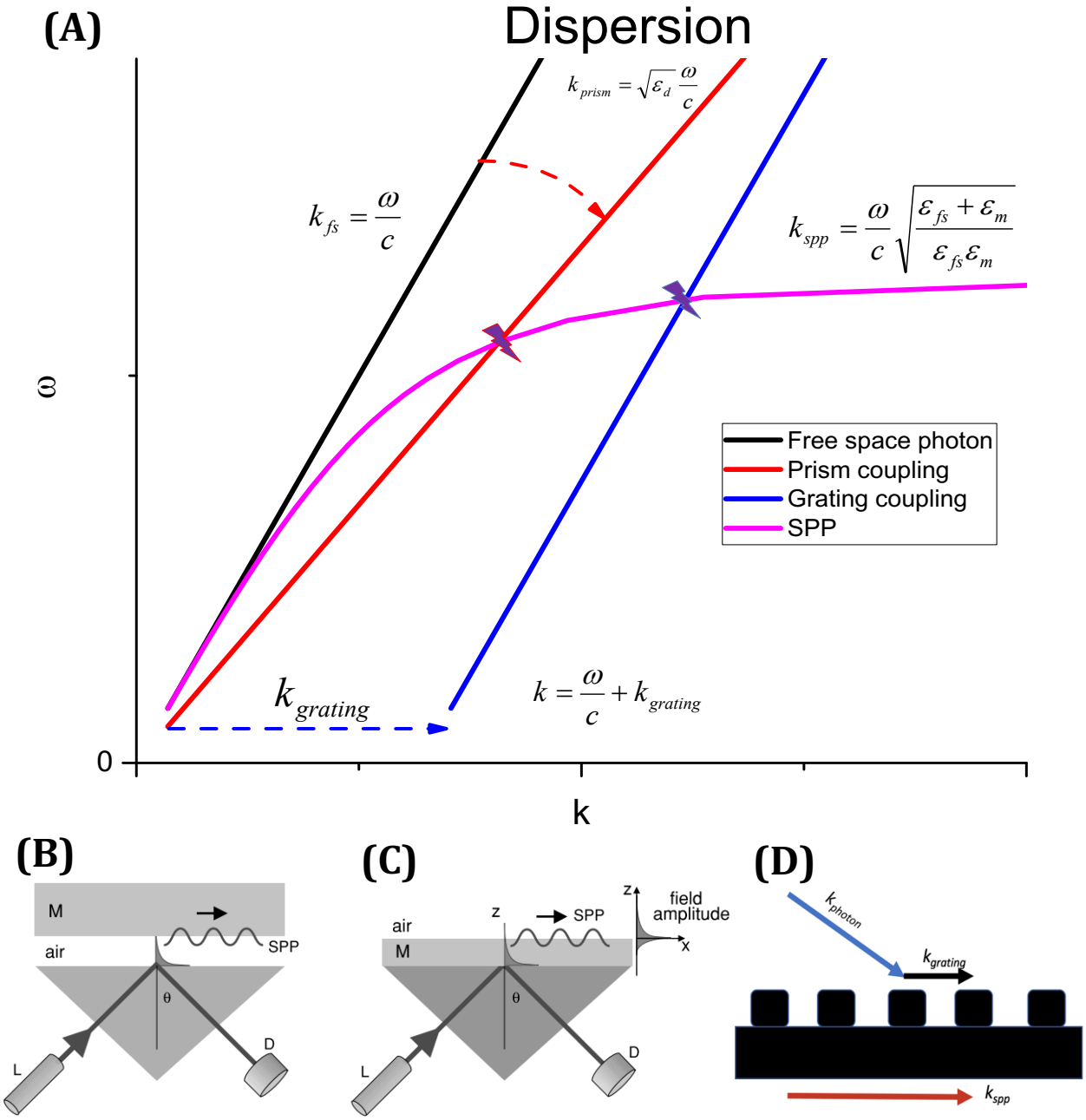

Fig. 1.3 (A) Dispersion matching for SPP coupling approaches. Black line represents propagating free space photon. Red line corresponds to photon, propagating in prism with ε_d . Blue line describes diffractively shifted photon dispersion after interaction with periodic grating. Purple line illustrates surface plasmon; Excitation of surface plasmon polariton. Schematic representation of Otto (B) and Kretschmann (C) configuration. L: laser, D: detector, M: metal layer. Adopted from ref. [1]; (D) Grating coupling. Here, the missing wave-vector for SPP initiation is acquired from periodic lattice.

SPP on a metal-dielectric interface cannot be excited directly from the same dielectric half-space due to the lack of necessary $k_x = k\sqrt{\varepsilon}\, sin\theta < \beta$, ranging from 0 to full k, depending of angle of incidence. In addition, SPP cannot be excited from bulk metal part due to a limited propagation depth and reflectivity. There is a straightforward way to do it by electron bombarding. However, optical excitation offers better capabilities and is more suitable for majority of applications. Several geometries can be used for that purpose, including the employment prism coupling and 3-layer systems. In the latter case, one creates an additional wave-vector by involving a medium with a higher permittivity. In such medium, photon can propagate with a larger wave-vector at the same frequency. Normally, at the interface between these two dielectrics that would result in a beam refraction, until the propagation in a lower permittivity region will not be restricted by absence of a valid far-field medium propagating $\boldsymbol{k} = \frac{\omega}{c}$, resulting in a Total Internal Reflection (TIR) effect. However, one can still use that light for SPP initiation between the metal and the lower permittivity medium by arranging its interface in a close proximity to the higher permittivity medium and considering near-field propagation. In practice, this approach is realized in Otto (Fig. 1.3b) and Kretschmann-Raether (Fig. 1.3c) geometries. Kretschmann-Raether configuration implies a direct contact between prism and thin layer of metal, where exponentially decaying electric field passes through the metallic layer. On the other hand, the Otto's configuration offers near-field transmission through the small dielectric gap between the prism and the metal. As a result of successful coupling, one can observe a minimum in reflected light intensity for a given wavelength. Ideally, material of the prism should provide low absorption and minimal dispersion variation at optical scales, while a symmetrical glass prism geometry is better suited for SPP excitation, keeping source and detector at the same angles with respect to the interface and satisfying required condition for TIR. The Kretschmann-Raether version has become a standard tool for SPP excitation due to simplicity of its experimental realization.

Another popular approach for SPP formation related to employment of periodic diffraction lattices[5]. This approach allows a direct coupling between the dielectric and metal half-spaces. The arrangement should be done in such a way that a non-zero diffraction order propagates along the interface and thus may obtain or loose additional momentum of the grating $\mathrm{k}_g = \frac{2\pi}{\mathrm{a}}$, there a – grating period:

$$\mathrm{k}_{spp} = \mathrm{k}_x \pm \mathrm{k}_g \tag{1.23}$$

1.3.3 Localized surface plasmon

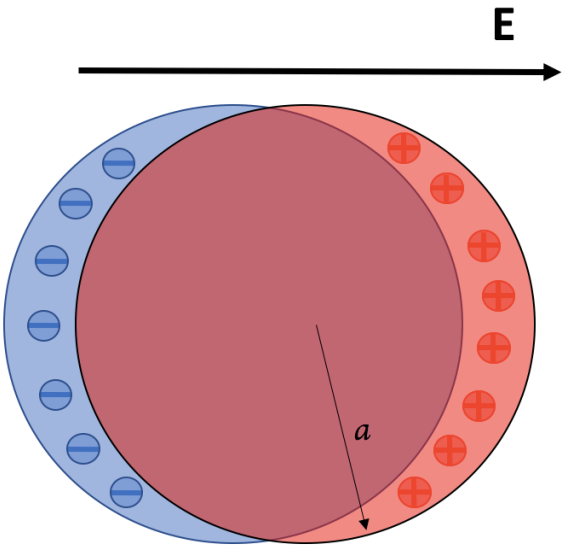

Fig. 1.4 Schematic illustration of localized surface plasmon excitation. Conductivity electron cloud (blue) oscillates over an assemble of positive ion cores (red) of a metallic particle with radius a under the applied field **E**.

In contrast to propagating and dispersive SPP, localized plasmon is a non-propagating excitation of free electron cloud in metallic nanostructures. The effect appears due to nontrivial scattering properties of sub-wavelength sized conductive objects in oscillating electromagnetic field. According to Maxwell's equations, electromagnetic field inside metal should be equal to zero. Curved nanoscale surface of the nanostructure creates an effective restoring force on electrons. This oscillation system can provide a resonance, which is accompanied by near-field amplification inside and outside the nanoobject[3] . The resonance frequency depends on the size, shape, composition and local optical environment of the nanostructure[6,7]. Consider a metallic nanoparticle with a being its diameter and ε_m - complex dielectric permittivity (Fig. 1.4). The particle is located in uniform non-absorbing dielectric media with ε_d and is exposed to harmonic electromagnetic field. Depending on λ/a ratio with λ – excitation wavelength, analytical description might be presented by several approaches. In the case of $a \ll \lambda$, interaction is well described by a quasi-static approximation, assuming that electromagnetic field distribution is identical over the particle.

Skipping formula derivation which could be found elsewhere[1,3], the central result of this approximation can be defined as a dipole moment $p = \varepsilon_0 \varepsilon_d \alpha E_0$ with the polarizability of:

$$\alpha = 4\pi a^3 \frac{\varepsilon_m - \varepsilon_d}{\varepsilon_m + 2\varepsilon_d}. \qquad (1.24)$$

The resonant condition is satisfied by nullifying the denominator:

$$\mathrm{Re}[\varepsilon_m] = -2\varepsilon_d. \tag{1.25}$$

This relationship is called Fröhlich criterion associated with dipole surface plasmon. It is easy to find that for a Drude metal in air environment the Fröhlich criterion is satisfied at $\omega_0 = \omega_p/\sqrt{3}$. Here, the resonance spectral location red-shifts with an increase of a permittivity ε_d of surrounding medium, suggesting nanoparticle employment for sensing applications. In practice, the quasi-static approximation provides reasonably good correlation with experimental results for spherical and ellipsoidal particles having dimensions below 100 nm. It is interesting, that the absorption and scattering efficiencies for such particles are proportional to a^3 and a^6, respectively. Consequently, for larger particles extinction is dominated by scattering whereas for small particles it is associated with absorption. In the case of essentially large particle sizes, scattering is described by Mie theory.

Localized surface plasmon provided by electron cloud oscillations can interact with other plasmonic structures. Suppose a pair of two identical nanoparticles located in a close proximity one to each other. Depending on particle separation distance d, several different types of interactions can occur. For $d < a \ll \lambda$, near-field coupling with d^{-3} distance dependence dominates. Scattering is suppressed, while extreme enhancement of electric field for small inter-particle distances can be used in sensing application such as Surface Enhanced Raman Scattering (SERS)[3]. For larger gaps, far-field dipolar coupling, proportional to d^{-1} plays a key role. Diffractively-coupled localized plasmon resonances present a prominent example of far-field coupled arrays[8,9]. Providing extreme narrowing of resonance feature, these phenomena is now actively used in biosensing.

1.4 Metamaterials

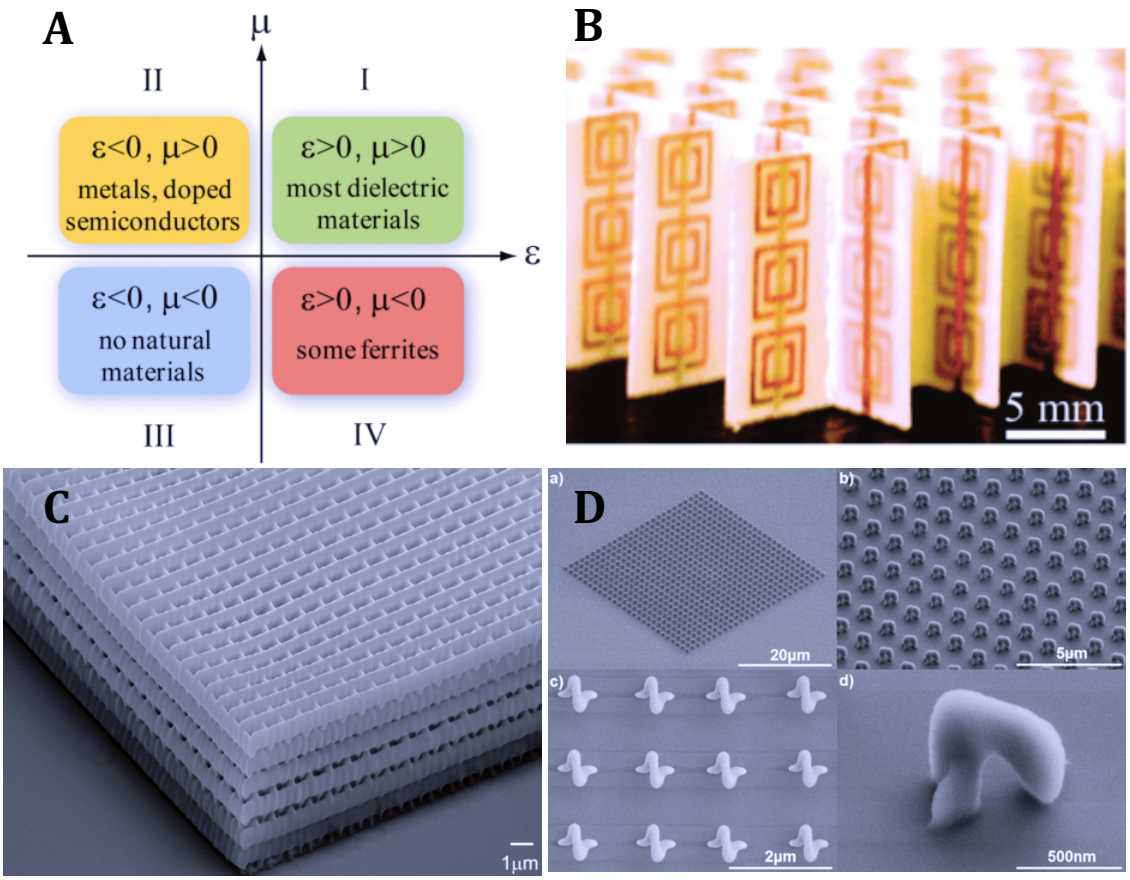

Fig. 1.5 (A) Parameter space of material characterized by optical constants; (B) Artificial negative index material for microwave range. Both adopted from ref. [2]; (C) Woodpile nanoscale metamaterial. Adopted from ref. [10]; (D) Chiral metamaterial nanoarray of spirals, produced by 2PP method. Adopted from ref. [11]

Metamaterials have recently formed a novel hot research topic with thousands of publications annually. Properties of bulk material are essentially determined by its chemical composition and bonds[2]. Metamaterial is defined as a material composed of nanoscale scattering elements (metaatoms), whose size is typically smaller than applied wavelength[3]. When combined and arranged properly (shape, size, geometry and orientation), these united blocks create an artificial material having new properties, which cannot be found in natural materials or chemically synthesized substances. Unique metamaterial properties appear essentially due to the formation of the metaatom ensemble and cannot be obtained from separate metaatom components. The extension of natural properties to new limits lies in term of metamaterial, which comes from Greek "μετά"- beyond. A rapid development of metamaterial field during last decade is largely due to recent improvements of nanotechnology and opportunities for creation nano-constructions and nano-composites at ranges, significantly smaller than light wavelength,

which is a core idea of optical metamaterials operation. Light does not distinguish independent atoms or molecules in the material. Optical response is somehow averaged and material is described by macroscopic parameters, such as permittivity. Essentially, same approach can be applied for metamaterials description via effective permittivity and permeability. The new research area opened up by Pendry *et al* with the creation of negative index metamaterials[10]. Further applications include superlensing, cloaking devices, sensors and a whole bunch of novel functionalities, introduced by implementation of 3D metamaterials[2,11,12].

1.5 Plasmonics in biosensing applications

1.5.1 Biosensing

Biosensing deals with binding events, involving the interaction between selective counterparts such as e.g., antigen – antibody, complementary DNA strands, protein - DNA and other.[13] In general, one biomolecule (the capturing agent) is immobilized on a surface of sensor, allowing to detect its complementary analyte, presented in an analyzed solution. Various labels are normally used to mark the target analyte. The attachment of the label to the sensor surface serves as an indicator of a successful binding event, detected by optical or other techniques. One of the most common modern biosensing techniques is a fluorescence, which employs fluorophores for biomolecules labeling. Although these conventionally established techniques represent valuable and reliable tools, their limitations cannot address new challenges of biological research at submolecular level. It is important to mention, that fluorescence based approaches suffer from photobleaching and are not strictly quantitative[13]. Also, these methods require several time-consuming preparation procedures, which can last hours and even days, while the resulting signal can normally evidence the fact of reaction itself, but not its course, thus complicating the determination of reaction kinetics constants. Finally, by linking to labels, analyte biomolecules are modified from their native state, thus obscuring their natural activity and making high throughput analysis hard to achieve.

1.5.2 Historical survey

The first report of optical transduction effect was protocoled in the very beginning of the XIX century. R. W. Wood studied optical properties of diffraction gratings in 1902 and reported the observation of unknown effect, consisted in the disappearance of some spectral lines in reflection[14]. Placing a grating in a glycerol solution, Wood was able to detect a shift of spectral minimum position. This *anomaly* was theoretically explained by J. Zenneck a few years later by the introduction of a concept of surface plasmon polaritons[15]. In 1968 A. Otto proposed the utilization of attenuated total reflection effect in glass prism for SPP excitation along the metal surface through the thin layer of

dielectric[16]. Later Kretschmann and Raether proposed a modification of Otto's approach using the excitation of SPP through a thin metallic layer placed over a quartz substrate[17]. A successful SPP excitation should satisfy the dispersion relation for SPP propagation along the metal/dielectric interface and is characterized by a combination of two interrelated parameters: the spectral position of an extinction minimum peak and a proper angle of illumination. In late 1970s, surface plasmons were employed for thin film characterization and studies of boundary processes[18].

First implementations of plasmonic effects for sensing applications started in early 1980s[18–21] with the first pioneering work[20] of Liedberg *et al,* who proposed to track recognition/binding events on plane Au surface using Kretschmann-Raether prism geometry. The device benefited from the dependence of SPP environmental conditions and the fact that RI of saline solution is different from that of most biological species. The proposed sensor was then transformed to a commercially available unit BIACORE[21]. A strong demand from biological research and industries to such technology has then led to other successful commercial realizations of SPR based sensors, including AutoLab, Biosensing Instrument, ICx Nomadics[22] and Hofmann Sensor system etc[23]. By now SPR has become a leading technology for label-free studies of biomolecular interactions, which proved its efficiency for studies of numerous interactions.

1.5.2 SPR biosensing

Having a significantly easier experimental realization with no need for precise layer positioning, Kretschmann-Raether geometry became a standard for SPR-based sensing applications for a long time. Conventional plasmonic biosensors employ this geometry to excite surface plasmon polaritons over a thin 50-nm gold film in conditions of SPR[3,24–26]. Here, P-polarized light is directed through a glass prism and reflected from a gold film, deposited on its surface. SPR effect leads to a dip in the reflected intensity at a defined angle, whose value is resonantly dependent on RI of a thin 200-300 nm dielectric layer near gold. Biomaterial is immobilized at the surface of a biocompatible thin film coupled to the gold surface. Biomolecular binding events lead to an increase of the thickness of a biomaterial layer, which is accompanied by a change of RI of the medium, contacting the sensor surface. A change of SPP environment due to biomaterial accumulation will result in change of coupling conditions which may be monitored by angular or spectral shift[19,29]. Thus, by monitoring resonance conditions of plasmon excitation over a thin gold film, one can follow individual biological binding events on gold[20,21], which is normally not possible with conventional fluorescence based methods[13]. A great advantage of SPR sensing consists in the absence of a time-consuming labelling step and a simple quantitative assessment of the absolute amount of bound biomaterial, allowing for a real-time detection of binding events and a fast determination of kinetics constants.

1.5.3 LSPR biosensing

Localized surface plasmon resonance is considered as an extension of SPR and is realized by using metallic nanostructures[24,25]. The mirror-like quality of smooth noble-metal films changes dramatically when the metal is separated into sub-wavelength nanoparticles[25], resulting in increased absorbance and scattering properties. Moreover, plasmonic nanoparticles can serve as transducers that convert small changes of local refractive index into spectral shifts of extinction and absorbance spectra. Compared to SPR, LSPR possesses better both lateral and normal spatial resolutions. LSPR shifts can be tuned by optimizing nanostructures characteristics, such as size, shape and composition. The accuracy of the measurements is determined by the quality of the peak, which is characterized by spectral linewidth Full-Width at Half-Maximum (FWHM). Typical FWHM for LSPR over silver nanoprisms, nanodiscs and nanoparticles are around 100-150 nm. Single-nanoparticle sensor offers improved absolute detection limit (total number of detected molecules). Also, they have promising applications for measurements in solution or even inside the cell and tissues. Alternative sensing modalities include nanohole arrays (NHA) [29–34], which showed greater sensitivity in response to refractive index changes.

1.5.4 Sensitivity of SPR and LSPR biosensors

Most of current commercially available SPR devices are based either on tracking of the reflection intensity value for predefined wavelength and at various angles of incidence (angular interrogation), or the spectral position of intensity minimum under a fixed angle of incidence (spectral interrogation). Such SPR biosensors can provide relatively high sensitivity of the order of 2000–4000 nm of spectral resonance shift per refractive index unit change[25]. These amplitude-sensitive interrogations are capable of detecting 1 pg/mm^2 of biomaterial accumulated on the sensor surface[23,28]. Such sensitivity is sufficient for studies of many interactions involving relatively large molecules (antibody-antigen, protein-DNA, DNA-DNA etc[27,28,35]). However, the sensitivity still needs to be greatly improved for the detection of low molecular weight analytes (drugs, vitamins etc.), as well as a larger low copy number analytes (antigens, viruses etc.), which are deadly or pathogenic even in ultra-low quantities[36,37].

Despite a number of undisputable advantages, nanoparticle or nanoarray-based schemes are not able to solve the sensitivity problem. Sensitivity of 2D LSPR nanoscale geometries to refractive index variations is much lower: 200–500 nm/RIU for LSPR and nanoparticle arrays[24,25], 300–400 nm/RIU for nanohole arrays[31,32]. Although the existing LPR methods can detect 100-1000 molecules of relatively large analytes[24,25], the detection limit in terms of the amount of biomaterial accumulated on the surface is, typically, ~1000 pg/mm^2, which is much larger than in the case of SPR[21,28] and in turn is inferior by 3-4 orders of magnitude compared to labelling methods. Limited sensitivity level of 2D periodic plasmonic arrays is related to diffractive nature of coupling light to plasmons,

which links the sensitivity to structure periodicity $\Delta \lambda / \Delta n \sim d$[38], which is typically of the order of hundreds of nm.

Total sensitivity of a SPR biosensor depends on plasmonic transduction modality (SPR, LSPR), experimental setup optical geometry (single- or multi-pass excitations), choice of the detected parameter (intensity, phase) and the level of noises (environmental, instrumental). Generally, the term "sensitivity" in SPR terminology is related to the response of the detected parameter (intensity, angular of spectral position of SPR dip, phase) to a unit change of RI. In addition, it is also critically important to resolve small variation of RI. The resolution of measuring system has a *Limit Of Detection* (LOD), which critically depends on the level of instrumental (electronic and optical noises of the source, detector) and environmental noises (inertial drifts, temperature drift of refractive index) in an individual measurement setup[27]. Current amplitude-sensitive based SPR devices LOD normally is estimated as 10^{-6} - 10^{-5} RIU[27,28].

1.5.5 Phase-sensitive plasmonic biosensors

It was found that the employment of phase properties of reflected light can improve the level of sensitivity under SPR[9,27,39–43]. Having optimal thickness of SPR-supporting film, phase of light can provide orders of magnitude better sensitivity than amplitude characteristics[43,45,48], although such result can be achieved for a relatively narrow dynamic range of measurements[27]. This expectation was based on the existence of a sharp jump in angular or spectral dependence of p-polarized light phase component under SPR in conditions of zero reflection (light darkness) corresponding to the minimum of SPR curve[9,41]. The lower is the intensity within this minimum – the sharper will be a phase jump under SPR. The sharpness of this jump and corresponding phase sensitivity do not follow the periodicity-related limitation rule, but are determined by the quality of resonances and first of all their depth (light darkness in the resonance)[9,45].

Three main reasons of higher sensitivity and, consequently, lower detection limit of phase-sensitive schemes compared to amplitude-sensitive ones were distinguished[42,43]. The main reason is related to a much stronger probing electric field at the point of maximal phase variation compared to the amplitude-based one. Under SPR there is a resonant transfer of energy from a pumping photon to a plasmon at the resonant angle of light incidence (or resonant wavelength). This phenomenon is accompanied by simultaneous amplitude and phase changes for reflected light: a drastic drop of amplitude and a sharp phase jump. The phase jump takes place in the very dip of the SPR curve, whereas maximal amplitude variation is observed on the resonance slopes. Electric field of the plasmon wave finds itself in the adjacent dielectric medium and therefore the plasmon becomes sensitive to its refractive index (or dielectric constant). Thus, a unit change of the dielectric layer thickness on gold (or a change of RI of the medium) causes a change of conditions of plasmon excitation and the response of the plasmon is maximal when the vector of probing electric field is maximal. It is clear that such vector is maximal in the very dip of the SPR curve where maximal change of phase and not amplitude take

places, yielding to much stronger phase response to a unit change of RI. Such electric field enhancement factor results in one order of magnitude larger sensitivity of phase to refractive index variations[42]. The second reason of much lower detection limit is due to a much lower level of phase noises compared to amplitude ones. Indeed, if the detector is adjusted at the maximum of its sensitivity, drifts related to laser source normally present main instrumental noise limiting the LOD of measurements. Lasers usually provide radiation with a very low level of phase noises $\Delta\varphi/\varphi \sim 10^{-6}$, while intensity noises of common lasers are significantly higher (usually at the level of $\approx 10^{-2}$)[42]. Since amplitude noises of laser sources are orders of magnitude higher compared to the phase ones, phase characteristics can potentially provide much lower detection limit. Finally, phase offers much better possibilities for signal averaging and filtering, as well as for image treatment. Phase control implies inherent relative measurement with respect to a reference beam or an unaffected component of the same beam. This makes possible spatial or temporal mapping, depending of geometry of phase-sensitive setup, and a subsequent filtering/averaging using the chosen map. Due to all these reasons, the LOD for phase interrogation methods achieves significant values of 10^{-9} -10^{-8} RIU[27].

1.5.6 Plasmonic metamaterials for biosensing

The concept of plasmonic metamaterials for biosensing[46] was introduced as a way to improve sensitivity of currently available natural materials (Au, Ag) and enable new functionalities, including size-based selectivity, spectral tuneability, extremely strong electric field enhancement and localization near nanoparticles and nanoarrays[25,47] resolution beyond the diffraction limit[48–52]; nano-tweezing[53]. The first sensor-oriented plasmonic metamaterial was based on an array of Au nanorods positioned normally to a supporting glass slide[46]. Such metamaterial made possible the excitation of a new guided mode G over the nanorod matrix in addition to classical transversal and longitudinal plasmonic modes over nanorods. Benefiting from a substantial overlap between the probing field and active biological substance incorporated between the nanorods and a strong plasmon-mediated energy confinement inside the layer, this metamaterial provided an enhanced sensitivity to refractive index variations of the medium between the rods (more than 30,000 nm per RIU change) and could be employed for ultra-sensitive detection of biological binding events in the nanorod matrix. Similar level of sensitivity was later observed on hyperbolic metamaterials[54].

One of the most promising modern sensor-oriented metamaterials is based on arrays of Au nanoparticles capable of supporting ultra-narrow (down to 2-3nm FWHM) diffractively-coupled localized plasmon resonances. The existence of ultra-narrow resonances was first predicted in theoretical works[55–62], then observed in experiment [8], followed by other independent experimental confirmations[63,64]. PSLR produced in conditions of diffraction coupling of LPR are of particular interest for biosensing applications due to their exceptional resonance quality[8,63,64]. To excite PSLR, gold nanoparticles (nanodiscs, nanopillars etc.) having the size of about 100 nm are arranged

in a 2D lattice in such a way that one of diffracted beams, appearing due to the periodicity of this structure, propagates over the array plane and can couple with localized plasmons over individual nanoparticles in far field. Such a coupling leads to a drastic narrowing of resonances in reflected and transmitted light down to several nanometers, comparing to ~ 50 nm for Au thin film SPP-based sensors[26]. In addition, the diffraction coupling gives rise to vanishing of light intensity in resonances, leading to the generation of singularities of light phase[9,45]. When used as a signal parameter to monitor refractive index variations, such phase singularities can be used to lower the detection limit of label-free plasmonic biosensing schemes down to single molecule level[27,39,42].

1.5.7 Plasmonics for SERS

During last decades, optical spectroscopy became extremely popular technique for biochemical analysis. Being a very straight-forward approach for material characterization, this technique does not require expensive equipment or profound expertise from researcher. Raman scattering provides a rich variety of information on the structure and chemical composition of the matter, based on its vibrational fingerprints[65] In essence, Raman scattering is similar in some sense to the amplitude modulation used in broadcasting. Carrier frequency of monochromatic light is modified by inelastic photon scattering, corresponding to molecular bond resonant oscillations. As a result, Raman scattered light will consist of sums and differences of the base light and vibration energy frequencies. However, probability of that interaction is extremely small. For instance, a typical cross section of fluorescence is around 10^{-18} cm^2 which is sufficient to resolve single molecule detection[66], while Raman scattering cross section is estimated much lower, typically 10^{-30} cm^2[66]. As a result, long exposition times and high spatial stability of samples are required for reasonably adequate measurements. As a vibrational technique, Raman spectroscopy can bring much more information than fluorescence. In particular, it can give quantitative details about the chemical structure and interaction of a specific molecule, mechanical stress, electronic properties. In addition, Raman does not require employment of fluorophore markers and is considered to be a label free technique.

To surpass small Raman scattering cross-section issues, Surface Enhanced Raman Scattering (SERS)[67] technique was developed. Strong field localization at the edges and along the surfaces of metallic nano-objects may be used to increase amount of Raman scattered and detected light, potentially down to single molecule level. Typical enhancement factors[1] for the Raman signal observed from rough metal substrates as compared to bare glass substrates may vary from 10^6 to 10^7. If the excitation wavelength satisfies localized plasmon resonance conditions for nanostructure, enhancement factor is dramatically increased[68,69] and may be as high as 10^{12}. In particular, Nie and Emory observed maximal enhancement of Raman scattering by 10^{14} on randomly agglomerated nanoparticles assembles for single molecule detection[68]. Current tasks include more complicated geometries with the use of not only metal nanostructures on the surface[70], but also

mobile probes for in vitro and in vivo applications. In particular, SERS probes have already been used for the detection of pH concentration inside various regions of a living cell[71] and even for the detection of glucose *in vivo*[72]. It is worth mentioning, that plasmonic effects for fluorescence spectroscopy enhancement have some limitations. For close distances, excited fluorophore electrons simply transfer it energy to metal via tunneling and no radiation occurs. For a reasonable illumination power, Raman is not a subject for photobleaching. In general, it is more robust, compared to fluorescence and does not suffer from degradation of emitters.

Chapter 2

Experimental techniques and methods

CONTENTS

2.1 Ellipsometry

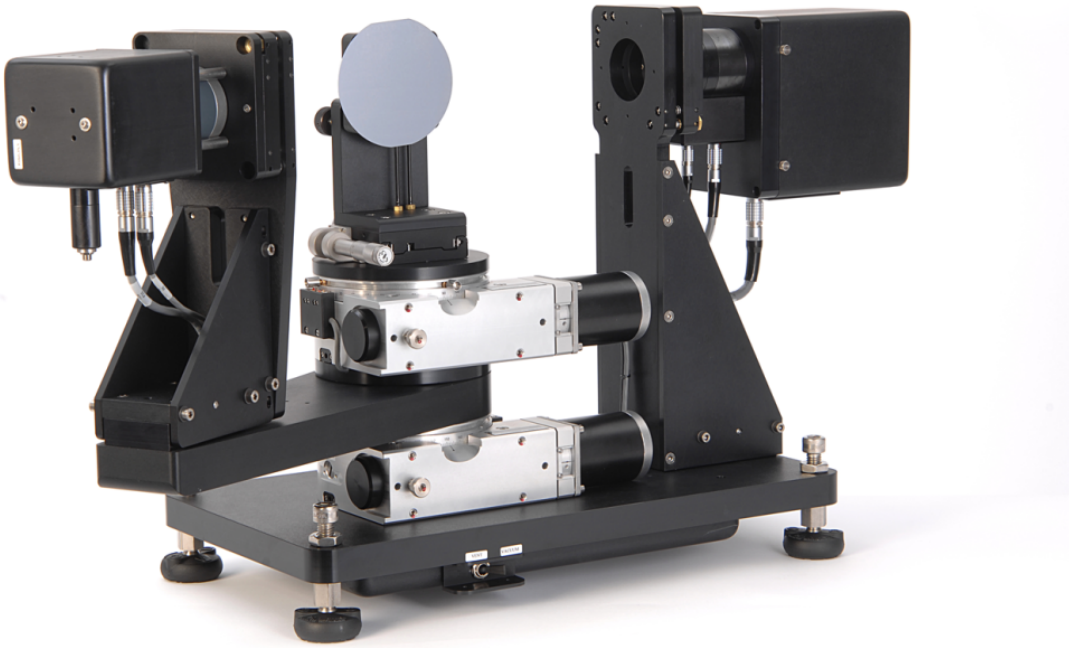

Fig. 2.1 Overview of Woollam M-2000 ellipsometery system, used in this research. Wide-spectra detector and source arms may be adjusted independently from sample position and orientation.

Ellipsometry is an optical technique, initially developed for thin film depth identification. It is based on an idea that differently polarized light interacts differently with the material surface. By monitoring phase-polarization properties of light reflected from a sample, one can determine its optical parameters. Those parameters can be derived through normalized electric field components r_p and r_s (complex quantities), which correspond to the Fresnel reflection field components parallel and perpendicular to the plane of light incidence. Ellipsometry measures the complex reflectance ratio ρ, which is the ratio of r_p over r_s, and can be decomposed into amplitude and phase components:

$$\rho = \frac{\mathrm{r}_p}{\mathrm{r}_s} = tan\Psi e^{i\Delta} \tag{2.1}$$

where the real part *tan(Ψ)* is the amplitude ratio upon reflection, and the imaginary part Δ is the phase shift (difference between the phase of the r_p and r_s components). Measured parameters can then be routinely converted to more the conventional r_p and r_s. This approach is very sensitive, since ellipsometry measures the ratio of the two reflection coefficients and thus insensitive to random noise sources.

Most of experimental data in this thesis was obtained with Woollam M-2000 ellipsometer (Fig. 2.1), which makes possible independent relative displacement of sample and both source and detector arms. Available optical spectra range lies between 270 nm and 1700 nm, using Xenon lamp as an illumination source. Parallel light beam is slightly focused through low-NA objective into a small spot around 50 um and afterwards collected by a detector via similar low-NA objective. The flexibility of experimental setup enables to arrange not only a direct sample illumination geometry, but also prism coupling techniques geometries including Kretschmann-Raether type. Sensitivity measurements performed with home-made liquid cell in both configurations, which made possible precise control of sample environment with liquid input and outlet ports.

2.2 Scanning Probe Microscopy

2.2.1 Brief overview

Scanning Probe Microscopy (SPM) is a modern research technique used for surface analysis. Invented in 1981 by G. Binnig and H. Rohrer as Scanning Tunnelling Microscopy (STM), SPM evolved to a powerful tool for topography imaging, magnetic and electric material property characterization. Core of the technology lies in ability for nano-manipulations with precision down to angstroms due to utilization of piezoelectric positioners. The probe may be manufactured from different materials and formed in various shapes, depending on research requirements. However, one of the main benefits of SPM design is a possibility to surpass optical resolution, so the probe size normally is below 50-100 nm and can achieve extreme values as low as several nm for whisker types. Probe positioning is controlled through closed feed-back loop. Depending on utilized feed-back mechanisms, most SPM devices may be divided into STM and Atomic Force Microscopy (AFM). STM feed-back is based on tunnel current between the conducting sample and conducting probe. AFM is not restricted by conductivity issues as it is based on mechanical interaction sensing of Van der Waal forces, represented by Lennard-Jones potential. In AFM tip is attached to a small lever and is illuminated by a tracking laser. Lever surface reflects the laser beam to the quadrupole photodiode detector which converts displacement of probe-lever (cantilever) system into currents and thereby may be processed by electronics. Probe collects surface information by raster point-by-point scanning.

Fig. 2.2 NT-MDT SPECTRA. Atomic force microscope combined with optical confocal spectrometer

2.2.2 Optical resolution limit

Photon is a convenient tool for research, as it is fast, easy to manipulate and detect. Photon is also very small and can carry more structural information about researched objects, than unarmed eye can perceive. However, Heisenberg uncertainty principle defines finite dimensions for the light. This restriction becomes significant for highly focused light beam at $\sim\lambda/2$, there confocal microscopy fails to improve resolution beyond the diffraction limit. A photon cannot resolve objects, smaller than its own size. In reciprocal space notation, light dispersion does not allow to transmit waves in free space with spatial frequencies $k > \omega/c$. Structural information for objects whose size is comparable with $k < \omega/c$ can be carried in far-field by homogeneous propagating modes. The rest exponentially decays in space and are called evanescent waves or near-field. Near-field is confined to matter borders, which are defined by optical constants. However, subwavelength structural information it holds does not necessarily lost. By some means

near-field can be captured and transported to detector. The central idea of near-field optical microscopy is to retain spatial frequencies associated with evanescent waves thereby increasing the bandwidth of spatial frequencies.

2.2.3 Scanning Near-field Optical Microscopy

A concept of near-field microscopy was introduced by O'Keefe in 1956[73] and experimentally confirmed in microwave regime by Ash & Nicholls in 1972[74]. Invention of SPM in 80s proposed researchers an affordable tool for evanescent waves investigation. Combination of optical techniques with SPM opens up a wide range of new opportunities. SPM precision in nano-positioning allows to arrange focal spot composition with nano-objects and perform nano-manipulations. Variety of SPM-based SNOM techniques can be divided into two parts[75]: aperture SNOM and apertureless or scattering SNOM. Optical design of aperture-type SNOM differs from a confocal set-up by implementation of sub-diffraction sized aperture located in close a proximity to analyzed sample, which separates source and detector optical parts. Commonly, the aperture is formed by metallic coating on the sides of sharply pointed optical fiber or cantilever tip with etched hole. The resolution of that configuration is limited because the effective diameter of an aperture cannot be smaller than twice the skin depth of the involved in coating metal. Which is 6-10 nm for good metals at optical frequencies, resulting in 20 nm of aperture size. This is a principal restriction, however for routine measurements aperture diameter is usually kept between 50-100 nm for reasonable signal-to-noise ratio (SNR). On the other hand, apertureless SNOM offers an alternative solution. Near-field does not freely propagate in space, but it can still interact with other matter. AFM tip apex may be simplified to a particle, which can play role of near-field retransmitter, conveying information from near-field to the far-field. Under appropriate illumination, a particle is surrounded by a strongly enhanced field over a distance of roughly the size of the particle, which basically represents an electric dipole. Scattering SNOM offers better near-field detection efficiency and, at least in principle, is not limited in resolution[1,76,77]. The down-side of this approach is a presence of background scattering from the tip and sample in diffraction limited focal spot region.

Schematic illustration is presented on Fig. 2.3. The cantilever tip is illuminated by a focused laser beam so that scattered light is recorded by a detector. Tip apex radius of curvature $a \ll \lambda$ determines mechanical and optical lateral resolution which is typically, 20 nm. Having tip permittivity ε_t, tip apex polarizability may be described as:

$$\alpha = 4\pi a^3 \frac{(\varepsilon_t - 1)}{(\varepsilon_t + 2)} \tag{2.2}$$

AFM tip is constantly oscillating so the gap $z \ll \lambda$ between the tip and probing sample with permittivity ε_s is sinusoidally varied, resulting in a strong modulation of the near-

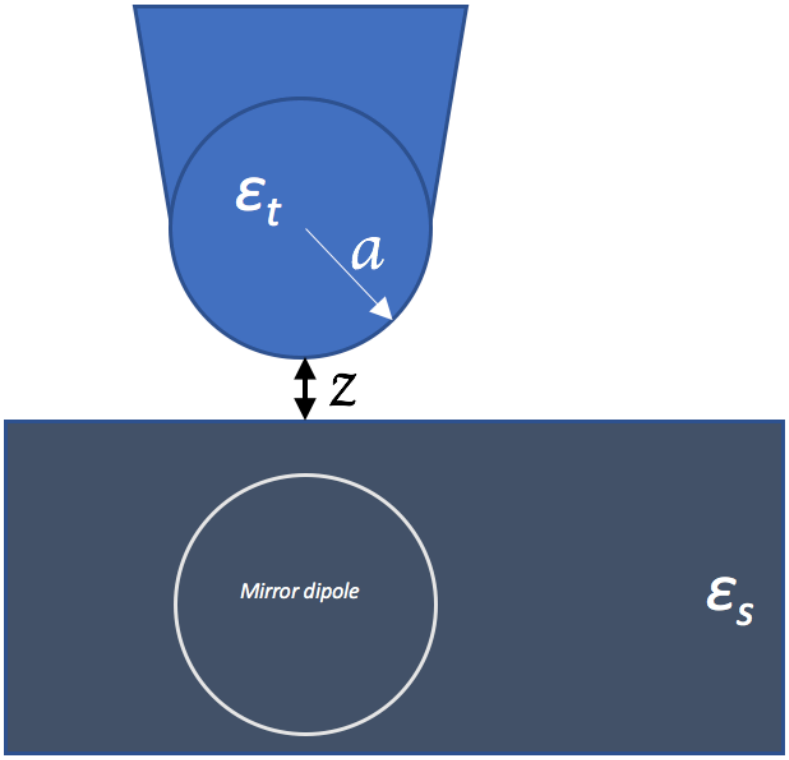

Fig. 2.3 Schematic illustration of SNOM principles. A tip with permittivity ε_t with apex of curvature a is placed over s sample with permittivity ε_s with a gap z between them. Tip apex initiate a mirror dipole in sample, which takes significant effect on overall system polarizability.

field scattering. In quasi-static approximation, near-field interaction may be calculated considering point mirror dipole model with polarizability $\alpha\beta$, where:

$$\beta = \frac{(\varepsilon_s - 1)}{(\varepsilon_s + 1)} \tag{2.3}$$

is the dielectric surface response function of the sample. The mirror's dipole field is inversely proportional to the 3rd power of distance z. Effective polarizability of tip-sample system includes both dipoles polarizabilities:

$$\alpha_{eff} = \frac{\alpha(1+\beta)}{1 - \frac{\alpha\beta}{16\pi(a+z)^3}} \tag{2.4}$$

Scattered from the coupled dipole system field E_s may be obtained from incident near-field E_i, as they are connected by effective polarizability:

$$E_s \propto \alpha_{eff}(1/z^3)E_i \tag{2.5}$$

However, as was pointed out earlier detected light consist not only of scattered near-field, but also from a massive amount of background scattering from the tip and sample inside

the focal cone. One of the approaches to separate sub-diffraction consistent from normal is to demodulate the detector signal at higher harmonic of tip oscillation. In general, the signal may be decomposed into Fourier series. In case of small modulation amplitude $\Delta z \ll a$, the Fourier coefficients are proportional to the n-th z-derivative of α_{eff}.[77,78].

Clearly, sample image contrast will depend on ε_s and ε_t. Highly conductive tips greatly increase scattered fracture of near-field, compared to dielectric ones.[77] Beside sub-diffraction optical characterization and chemical recognition, SNOM may be used for direct near-field imaging of plasmons.

Chapter 3

Diffractively coupled plasmonic surface lattice resonances of 2D nanoparticle array metamaterial

CONTENTS

3.1 Introduction

The employment of diffractively coupled LPR looks very promising for the improvement of performance of plasmonic biosensors as such resonances can be very narrow. However, conditions of implementation of these resonances, also referred as Plasmonic Surface Lattice Resonances (PSLR) in general are not always compatible with biosensing arrangement implying the placement of the nanoparticles between a glass substrate and a sample medium (air, water). In particular, the excitation of diffractively coupled PSLR is critically dependent on refractive index of the media surrounding a nanoparticle array. When the array is illuminated under normal incidence of light, the excitation of PSLR typically requires uniform surrounding, i.e. the match of refractive index of the substrate and that of the medium contacting the particles[64], although certain narrowing of resonances is possible via a proper choice of size and geometry of nanoparticles[63,79]. On the other hand, the excitation of PSLR becomes possible under oblique incidence of light on the array structure and the monitoring of optical parameters in reflected light[8,45]. In all cases, direct geometry of PSLR excitation is not fully compatible with biosensing experimental arrangement, as it implies light direction through a sample liquid leading to a dependence of PSLR parameters on bulk RI fluctuations inside the flow cell.

In this chapter, I present a first systematic study of conditions of excitation and properties of PSLR over arrays of glass substrate-supported single and double Au nanoparticles (~100-200 nm) in direct and Attenuated Total Reflection geometries[43,80]. Assessment of their sensitivity capabilities in spectral and phase interrogations with respect to variations of the adjacent sample dielectric medium refractive index (RI) is performed. Obtained data unambiguously show that spectral sensitivity correlate with the periodicity of the structures and exceptionally high phase sensitivity, which makes them very promising candidates for biosensing applications. Results of these work were published in [Th-1], [Th-3] and [Th-6].

3.2 Materials and methods

3.2.1 Sample preparation

High-quality regular and homogenous square arrays of gold nanoparticles were produced by e-beam lithography (LEO-RAITH and PIONEER-RAITH) on a clean microscopic glass substrate covered by a thin Cr sublayer. A double layered resist was used to improve lift-off (80 nm of 495 kD PMMA cast from a 3 wt% solution in anisole for the bottom resist layer and 50 nm of 95 kD PMMA cast from a 2 wt% solution in anisole for the top layer). Bare (without Cr seed layer) borosilicate glass substrates (WBO-251 from UQG Optics) successively coated by a single layer of PMMA (from Allresist, Germany) diluted in ethyl-lactate at 2%) is used for nanofabrication. Second layer of a conductive polymer (SX AR PC 5000/90.2 from Allresist) is applied in order to prevent the charging of the dielectric substrates during e-beam exposure. After developing in 1:3 MIBK:isopropanol solution, rinsing the samples in deionized water and drying under clean nitrogen flow, 3-5 nm of Cr (to improve adhesion) was deposited and 80-90 nm of Au by evaporation using electron beam or Joule effect (Auto 306 tool from Edwards). Then the excessive metal deposited onto the areas protected by the resist was removed from samples by the lift-off procedure in ultrasonic bath of pure ethyl-lactate. The typical array size was 0.2×0.2 mm^2. The samples on a clean glass substrate were obtained from the samples fabricated on a 5 nm Cr sublayer in which the Cr sublayer has been wet-etched after the fabrication procedure. Typical Scanning Electron Microscopy images of single and double nanodot arrays are shown in Fig. 3.2.

3.2.2 Methodology of measurements

Measurements were performed using Woollam M-2000on ellipsometer (Fig. 3.1, details in Chapter 2.1). In direct configuration, weakly focused beam of ellipsometer illuminated sample through the cover glass, which restricted the solution inside the flow cell and prevented system from leaking. Then, the beam passed through the solution, reflected from the sample and reached the detector via similar optical path. For ATR configuration, the bottom side of the sample was mounted to the ground slope of a glass regular prism via optical immersion oil, this matched RI of glass. A gap for liquid flow was provided with rubber O-ring, fixed between the sample from one side and a fixed cover glass from the other. Weakly focused light beam of the source refracted on one slope of the prism, crossed prism insides, passed through the tiny layer of immersion oil and the sample substrate cover slip and then finally, reflected from the nanoarray. Incident and reflection beam paths were adjusted to be symmetrical with respect to the prism orientation. Device analyzed intensities of differently polarized light and phase shift between them. Reflection spectra dependency from angle of illumination were recorded.

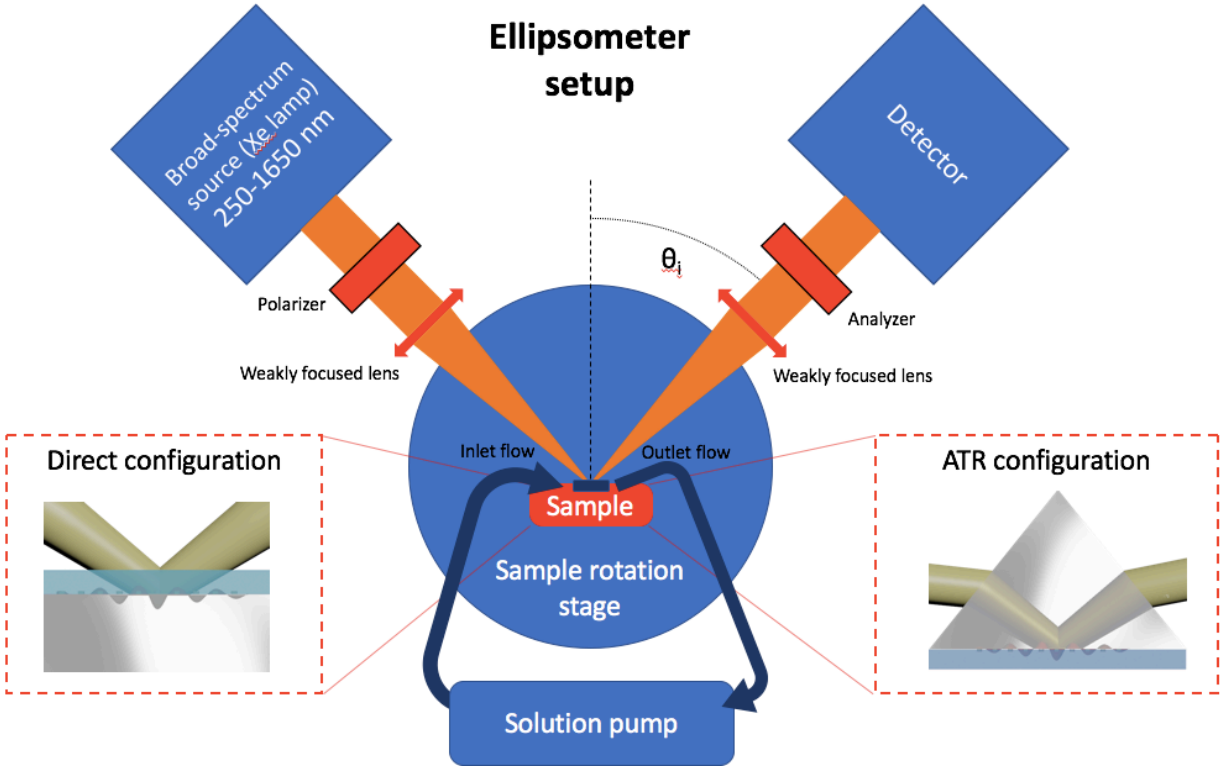

Fig. 3.1 Schematic representation of ellipsometer-based experimental setup for optical transduction sensing.

Data repeatability showed negligible variation of peak spectral position for each analyzed mixture, compared to system spectral resolution.

3.2.3 Sensitivity assessment

In these experiments, the sensitivity of plasmonic metamaterial transducers was evaluated by using a model, which simulated changes of bulk refractive index of the aqueous medium contacting nanoparticle arrays, similarly to how it was done in previous studies[9,46,81]. A set of ethanol-water mixtures of different concentrations were prepared for evaluation of sample sensing capabilities. Ethanol has excellent solubility in water and does not affect the quality of glass-supported nanoparticle arrays. Since ethanol has slightly higher refractive index compared to water (1.3614 compared to 1.333 for 589 nm wavelength at room temperature), its progressive addition to aqueous solutions provides nearly linear increase of refractive index of the liquid. The mixtures were pumped though the liquid flow cell, as shown in Fig. 3.1.

3.2.4 Applicability for biosensing

To assess the applicability of plasmonic metamaterial structures to biosensing, another well-calibrated protocol based on the Streptavidin-Biotin affinity model[24] was used. Glass slides with gold nanoparticle arrays were incubated for 24 hours in 1 mM of

3:1 ethanolic solution of 1-octanethiol (1-OT) and 11 – Mercaptoundecanoic acid (11-MUA) purchased from Sigma-Aldrich leading to the formation of a self-assembling monolayer with 10% surface coverage of carboxylate binding sites[24]. Since the active surface of each nanodot was equal to $\sim 10^4$ nm^2 such a procedure led to 2,000 active sites per nanodot. After incubation, the nanodots were rinsed with ethanol and dried in flowing nitrogen. Then, 1 mM biotin (Sigma-Aldrich) in 10 mM Phosphate-Buffered Saline (PBS) solution was linked to surface carboxyl groups using 1-ethyl-3-[3-dimethylaminopropyl] carbodiimide hydrochloride (EDC) coupling over a 3-hour period. Taking into account ~1-5% efficiency of EDC coupling[24], up to 20-100 biotin molecules attach to each nanodot. Finally, the biotin-covered nanodots were exposed to 10pM Streptavidin (SA, Sigma-Aldrich) solutions in 10mM PBS for 3 hours. Samples were finally rinsed with 10 mM PBS and water to remove all unspecifically bound molecules.

3.3 Conditions of excitation and properties of PSLR in direct and ATR geometries

Under normal light illumination PSLR can be normally excited only under symmetric environment surrounding nanoparticle metamaterial arrays[64], which prevents the implementation of biosensing schemes as the substrate and tested media typically have essentially different RI ($n_{sub} \sim 1.5$ compared to $n_{wat} = 1.33$ and $n_{air} = 1$).

However, this problem can be solved, e.g., by employing oblique light incidence[8,45]. In this case, PSLR can be efficiently excited even under asymmetry of optical environment, but they split into two modes corresponding to the coupling of localized plasmons via diffracted waves propagating in the tested medium or the substrate (Fig. 3.2a). The reason of this splitting is the following: for any regular nanoparticle array, diffracted beam disappears when it crosses the boundary between ambient medium (air or water) and the substrate due to the impossibility of transition between media having essentially different light dispersion. As a result, the diffracted beam is cut-off at Rayleigh cut-off wavelength (diffraction edge). In the case when a medium/substrate interface is present, there should be two cut-off wavelengths. One of them corresponds to the disappearance of the medium diffraction modes (when the diffraction wave crosses the sample boundary from air/water to the substrate) and other one is related to crossing the boundary in the opposite direction. Such two Rayleigh cut-off wavelengths for air/substrate interface can be presented as follows[8]:

$$\lambda_R^{air} = a/m(n_{air} \pm sin\theta),\ \lambda_R^{sub} = a/m(n_{sub} \pm sin\theta) \qquad (3.1)$$

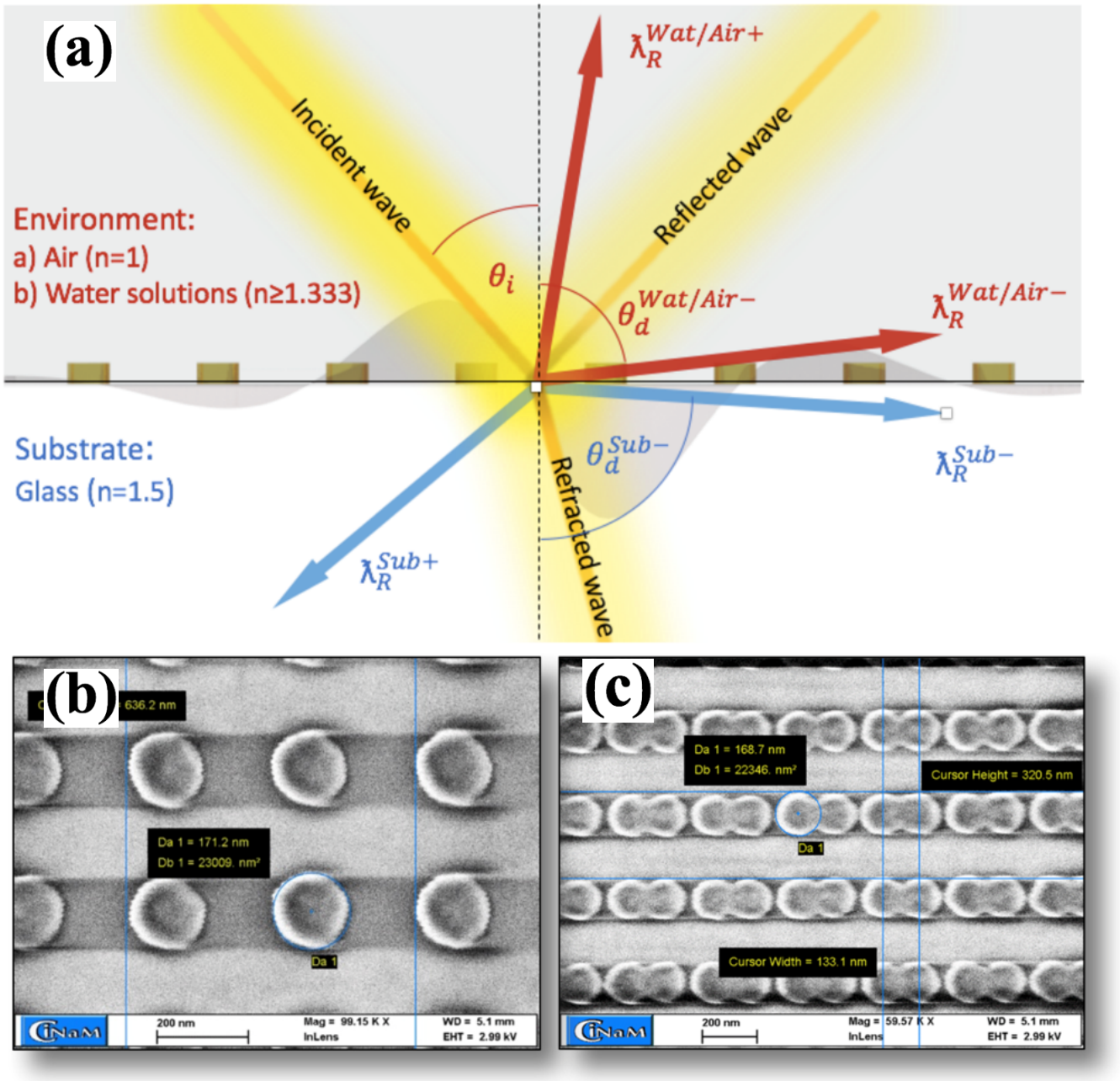

Fig. 3.2 (a) Schematics of excitation of diffractively coupled plasmonic surface lattice resonances over a metal nanoparticle array. When metal nanoparticles are arranged in a periodic lattice, they may scatter light to produce diffracted waves. If one of the diffracted waves then propagates in the plane of the array, it may couple localized plasmon resonances associated with individual nanoparticles leading to the generation of PSLR with a very narrow lineshape. In the presence of a substrate, this phenomenon takes place at Rayleigh cut-off frequencies for the medium (λ_R^{air} or λ_R^{wat}) and substrate (λ_R^{sub}); Typical Scanning Electron Microscopy images of single (b) and double (c) nanoparticle arrays used for the excitation of PSLRs.

where a is a period of the structure, m is integer, θ is the angle of incidence, n_{sub} is substrate RI. Similarly, for water/substrate interface Rayleigh cut-off wavelengths will be:

$$\lambda_R^{wat} = a/m(n_{wat} \pm sin\theta),\ \lambda_R^{sub} = a/m(n_{sub} \pm sin\theta) \qquad (3.2)$$

The effect of splitting of resonances can be easily seen in experiments. Fig. 3.3 presents spectral dependencies of ellipsometric parameters Ψ and Δ for light reflected from a 320-nm period metamaterial arrays: an array of single 163 nm (Fig. 3.3 a, d) and an array of double 134-nm (Fig. 3.3 b, e) gold particles having ~50 nm separation, contacting with air and water media, respectively. As shown in the Fig. 3.3, the resonances are indeed split into distinct medium- and substrate-related modes indicated as $PSLR_{air}$/$PSLR_{wat}$ and $PSLR_{sub}$, respectively, and they correlate with Rayleigh cut-off wavelengths λ_R^{air} / λ_R^{wat} and λ_R^{sub}, which are indicated as vertical yellow lines on the spectra. It should be noted that for single nanoparticle arrays diffractively coupled PSLRs match Rayleigh cut-off wavelengths (Fig. 3.3 a, d), while for double nanoparticle arrays the position of PSLRs can remarkably shift from these wavelengths (Fig. 3.3 b, e) due to near-field coupling in the nanoparticle dimer structure. PSLR typically appear in reflection as narrow Fano-shape dips over a positive background spectrum[8,45,82], presenting the combination of reflected and scattered light from glass-supported nanoparticle array system. However, when measured by ellipsometry and presented as a function of ellipsometric reflection Ψ, which describes a ratio of amplitudes of p- and s- components upon reflection $\tan\Psi = \frac{|R_p|}{|R_s|}$, the resonances can appear as both minima ($PSLR_{air}$ for single and double nanoparticle arrays, (Fig. 3.3 a, b) and maxima ($PSLR_{wat}$ for double nanoparticle arrays, Fig. 3.3e; $PSLR_{sub}$ for single and double nanoparticle arrays, Fig. 3.3 a, e). It is obvious that negative or positive polarity of $PSLR_s$ in $\Psi(\lambda)$ spectrum is determined whether resonant dips take place for p- or s-polarized component of light, respectively, or whether the substrate reflection is added to or subtracted from the reflection produced by the array. In general, the width and shape of PSLR critically depend on a variety of factors, including nanoparticle size, geometry of the unit cell (single or double particles), and refractive index of the environment. In addition, the emergence of different modes and their intensity strongly depend on the angle of light incidence. Here, different structures appear to provide optimal resonance characteristics under different conditions. As an example, the single 163-nm particle array provides a very distinct medium-related mode under its contact with air medium (Fig. 3.3a), while the same mode is almost absent in the case of its contact with water ambience (Fig. 3.3d). The substrate-related mode for this sample demonstrates the opposite tendency, as it appears to be much more pronounced in the case of water medium. As another example, the double 134-nm particle array provides much more pronounced medium-related mode under its contact with water medium (Fig. 3.3 b, e), while the substrate-related mode shows the opposite tendency. As shown in figure insets presenting some resonances at a magnified scale, the width of PSLR is also strongly dependent on array parameters and range from a few nm FWHM to 20-25 nm FWHM. In all cases, the implementation of ultra-narrow and high quality resonances

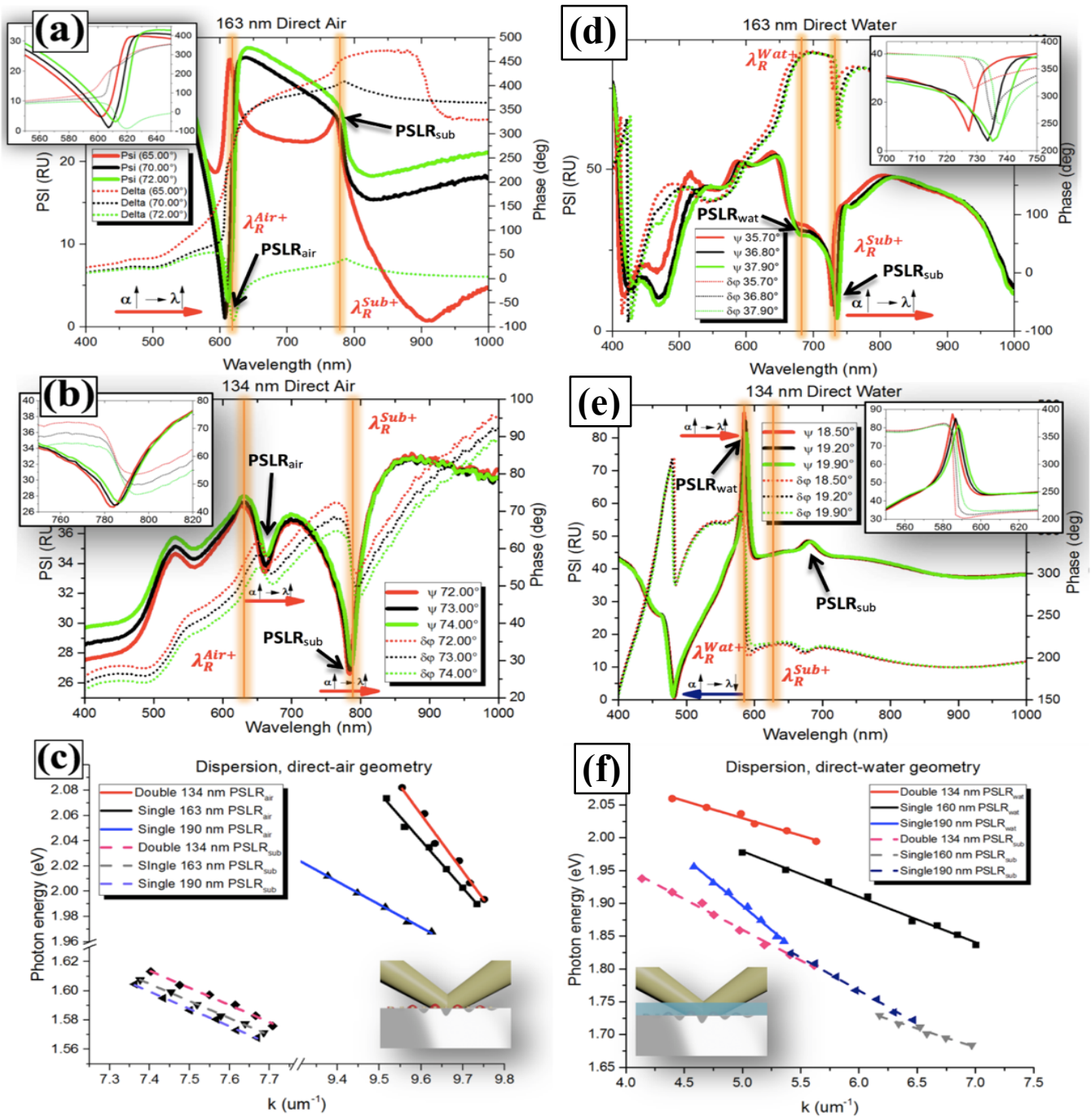

Fig. 3.3 Spectral dependencies of ellipsometric reflectivity Ψ (solid) and phase Δ (dashed) for a 320-nm period arrays of glass-supported gold nanoparticles contacting with air ((a) and (b)) and water ((d) and (e)) media under different angles of their illumination in direct geometry: (a) and (d) for single 163-nm particle array; (b) and (e) for double 134 nm particle array with the distance between the nanoparticles 50 nm. Vertical yellow lines show positions of Rayleigh cut-off wavelengths associated with diffraction edges for air, water and substrate media (λ_R^{air}, λ_R^{water} and λ_R^{sub}, respectively). The insets show some resonances at magnified scale. Dispersion curves describing conditions for the generation of resonances (combinations of the resonance angle of incidence and wavelength) constructed on the basis of experimental data for air-, water- and substrate-related modes $PSLR_{air}$ ((c), solid), $PSLR_{wat}$ ((f), solid) and $PSLR_{sub}$ ((a) and (f), dashed).

requires the optimization of array structures and their adaptation for concrete biosensing architectures and environments (air, water). Fig. 3.3 (c, f) show optical energy dispersion $E(k_x)$, which is constructed on the basis of experimental data (combinations of the resonance angle of incidence and wavelength). In fact, such dispersion summarizes conditions of excitation of medium and substrate modes in direct geometry for air and water environments, respectively. One can find that the dispersion curves $E(k_x)$ for both medium ($PSLR_{air}$, $PSLR_{wat}$) and substrate ($PSLR_{sub}$) modes have a characteristic descending course, which is related to a delocalized nature of diffractively coupled plasmon surface lattice resonances[83–86].

One of critically important characteristics of resonant phenomena is related to light intensity in the very minimum of the resonance (light darkness). If the intensity approaches to zero, it can lead to singularities of phase of reflected light[41], which can be used to strongly improve the sensitivity of plasmonic biosensing[39,40,46]. As follows from Fig. 3.3, all PSLRs are accompanied by phase jumps, shown by dashed curves, in the very minima/maxima of the resonance. For example, the generation of air mode $PSLR_{air}$ for single 163 nm particle array (Fig. 3.3a) and water mode $PSLR_{wat}$ for double 134 nm particle array (Fig. 3.3b), manifested as a dip and peak in $\Psi(\lambda)$ dependence, respectively, is accompanied by extremely sharp phase jumps at the resonance points with a total phase variation around 180 degrees. One can note that the generation of sharp phase jumps at resonant peaks and not dips does not contradict to the previous explanations of phase topological properties[9,41]. Indeed, the appearance of PSLR as peaks in spectral dependence for $\Psi(\lambda)$ is explained by a particular way of presentation of ellipsometric data, as reflectivity of s-polarized component finds itself in the equation denominator. In normal reflection, this resonance should obviously appear as a minimum for s-polarized component.

The experiments showed that all phenomena related to the excitation of PSLR over essentially asymmetric substrate medium interface can be efficiently reproduced in ATR geometry implying the illumination of the nanoparticle arrays from the glass substrate side. Furthermore, characteristics of such PSLR can be advantageous compared to the direct geometry. Fig. 3.4 show the excitation of PSLR in ATR geometry using the same arrays: single 163 nm particle array (Fig. 3.4 a, d) and double 134 nm particle array (Fig. 3.4 b, e) under their contact with air and water environments, respectively. Here, similarly to direct geometry, one can observe ultra-narrow PSLR modes near Rayleigh cut-off wavelengths, while the resonances equally appear as minima (e.g., $PSLR_{air}$ and $PSLR_{wat}$ for single 163 nm particle and double 134 nm particle arrays) or maxima ($PSLR_{sub}$ for the 163 nm particle array contacting air, and $PSLR_{sub}$ for the double 134 nm particle array contacting water). As in the case of direct geometry, PSLRs are generated exactly at Rayleigh cut-off wavelengths for single nanoparticle arrays (Fig. 3.4 a, d), while for double nanoparticle arrays the position of PSLR can be much shifted (Fig. 3.4e). The width and quality of resonances also critically depends on nanoparticle size, geometry of unit cell (single or double particles), refractive index of the environment. As an example, the array

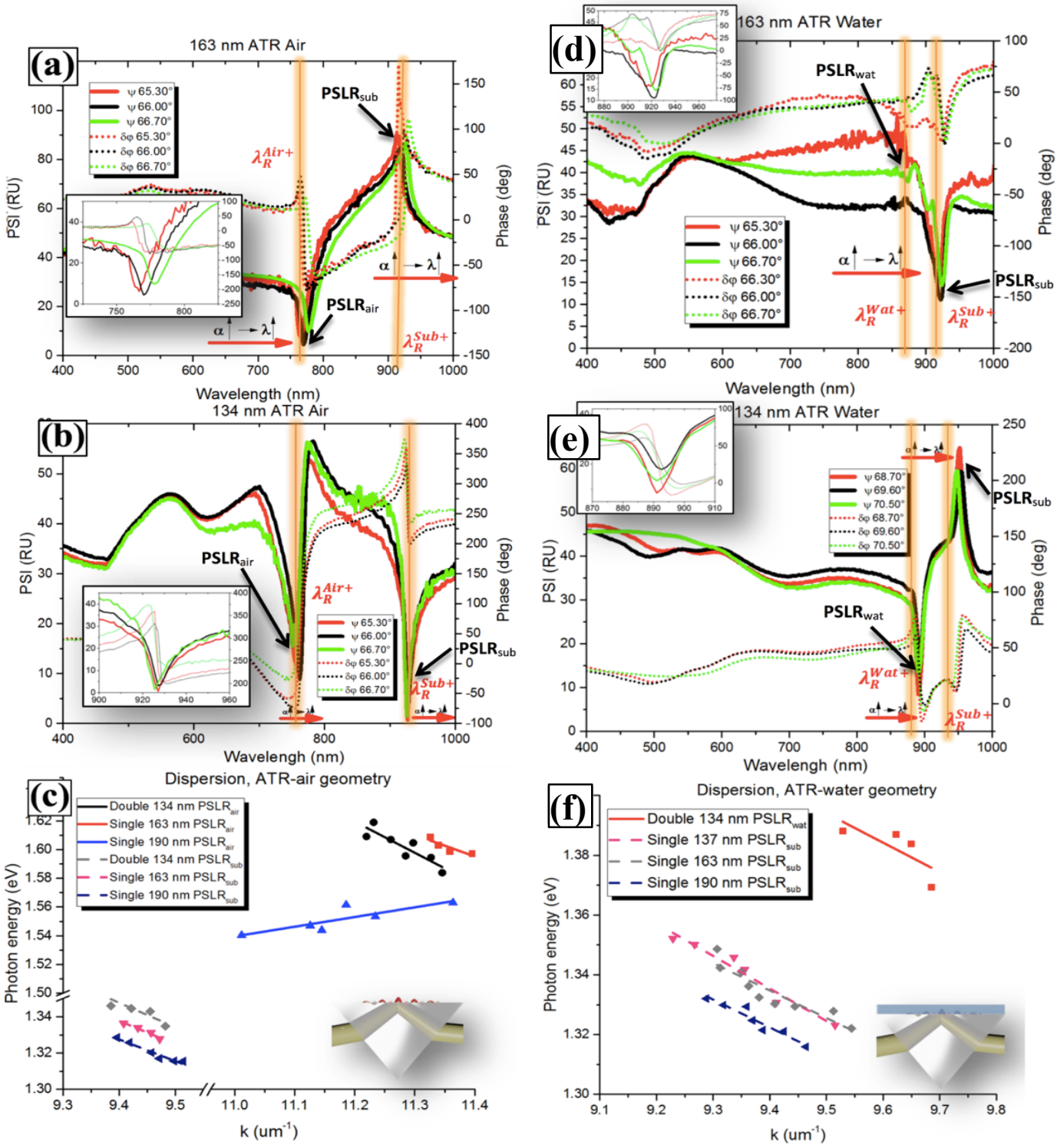

Fig. 3.4 Spectral dependencies of ellipsometric reflectivity Ψ (solid) and phase Δ (dashed) for a 320-nm period arrays of glass-supported gold nanoparticles contacting with air ((a) and (b)) and water ((d) and (e)) media under different angles of their illumination in ATR geometry: (a) and (d) for single 163-nm particle array; (b) and (e) for double 134 nm particle array. Vertical yellow lines show positions of Rayleigh cut-off wavelengths associated with diffraction edges for air, water and substrate media (λ_R^{air}, λ_R^{water} and λ_R^{sub}, respectively). The insets show some resonances at magnified scale. Dispersion curves describing conditions for the generation of constructed on the basis of experimental data for air-, water- and substrate-related modes $PSLR_{air}$ ((c), solid), $PSLR_{wat}$ ((f), solid) and $PSLR_{sub}$ ((a) and (f), dashed).

of single 163-nm particles demonstrates a prominent medium related mode under its contact with air (Fig. 3.4a), while this resonance is very weak under the contact of this structure with water ambience (Fig. 3.4d). Based on statistics of PSLR excitation in ATR geometry using various samples, one can conclude that single nanoparticle arrays demonstrate much better medium resonances under their contact with air ambience, while double nanoparticle arrays can provide high quality medium-related resonances for both air and water ambiences. As shown in insets to Fig. 3.4, the widths of PSLR in the ATR geometry are in average smaller compared with this parameter in direct geometry and can range from a few nm to 15-20 nm FWHM. Similarly, to the case of direct geometry, the generation of PSLRs is accompanied by sharp phase features and the sharpness of phase jump is determined by the depth of resonances. As an example, very sharp phase features with total phase variation close to 180 Deg. are observed for medium related mode $PSLR_{air}$ using single 163 nm particle array (inset of Fig. 3.4a) and for $PSLR_{air}$, $PSLR_{wat}$ using double 134 nm particle arrays (insets of Fig. 2.5b, Fig. 2.5e). As shown in Fig. 2.5 (c, f) optical dispersion $E(k_x)$ curves for medium ($PSLR_{air}$ and $PSLR_{wat}$) and substrate ($PSLR_{sub}$) modes demonstrate the same descending trend as it was observed in direct geometry. It should be noted that arrays of single 190-nm particles reveal a negative dispersion for $PSLR_{air}$ mode, which could be related to too large size of gold nanoparticles and possible involvement of complex plasmon modes (e.g., quadrupole ones).

Thus, ATR geometry makes possible the excitation of ultra-narrow diffractively coupled plasmonic surface lattice resonances over arrays of gold nanodots contacting both air and water ambiences, while characteristics of these resonances can be optimized by a proper selection of array parameters. The analysis shows that PSLR excited under ATR can be even narrower than relevant resonances under direct geometry.

3.4 Sensitivity of $PSLR_s$ to local environment

Ultimate biosensing experiment implies the functionalization of the plasmonic nanoparticles and immobilization of a sensor recognition element on them[24,25,87]. A target analyte (affinity partner) comes from aqueous ambience and is supposed to bind to the recognition element leading to an increase of refractive index of a thin layer around the nanoparticles, while a relevant change of conditions of PSLR excitation (spectral, phase) enables one to monitor the RI increase caused by the biological interaction. In this case, the resulting response of biosensor system is determined by both optical sensitivity of the plasmonic transducer to RI variations and the efficiency of the recognition element. Since the main objective of this work is related to the development of optical transducer based on PSLR, a physical model is used to simulate RI changes in order to simplify the analysis and avoid artificial facts related to the performance of the recognition element. To simulate the increase of RI of water ambience, aqueous solutions of ethanol of different concentrations were pumped through a flow cell by a peristaltic pump and brought into contact with the nanoparticle arrays, while PSLR were excited in both direct and ATR

geometries. A block containing the metamaterial slide with nanoparticle arrays and the flow cell was put onto the ellipsometer platform and examined.

Figure 3.5a shows spectral shifts of resonances due to changes of refractive index of the aqueous medium caused by the addition of different concentration of ethanol to water for an array of single 190-nm nanoparticles. The refractive index (RI) of the medium increases with the ethanol addition leading to a nearly linear red shift of PSLR. However, sensitivities of medium and substrate-related modes appear to be quite different. Here, the slope of the linear dependence for the medium mode $PSLR_{wat}$ shows the sensitivity of 357 nm/RIU, while the sensitivity of substrate mode is much lower (206 nm/RIU). Statistical analysis of sensitivities of medium and substrate modes for various samples shows that this parameter does not depend whether single or double nanoparticle arrays are used and is in the range of 310-360 nm/RIU and 190-200 nm/RIU for $PSLR_{wat}$ and $PSLR_{sub}$, respectively. In general, sensitivity of medium modes $PSLR_{wat}$ for different samples strongly correlates with the period of structures (320 nm), similarly to other transducers based on diffraction phenomena such as it was observed for surface plasmon polaritons over nanohole thin film arrays[31], while sensitivity of the substrate mode $PSLR_{wat}$ does not show any correlation with the array period and is much lower.

A more complicated situation takes place for sensitivities of medium and substrates modes in ATR geometry. Here, the value of sensitivity of the medium mode starts to depend whether its excitation takes place below or above the angle of total internal reflection (TIR) for glass/water interface (~ 63° Deg.) Indeed, as follows from Fig. 3.5b, sensitivity of $PSLR_{wat}$ below the TIR angle (~46° Deg.) is also of the order of the period of the structure (305 nm/RIU for double 134 nm particle arrays), while for angles of incidence above TIR (73° Deg.) this parameter can exceed 400 nm/RIU. Note that such a difference of sensitivities was recorded for a largely dominating majority of samples of single and double nanodot arrays, independently of the geometry of the unit cell. Here, the samples typically demonstrate sensitivity in the range of 300-340 nm/RIU below the TIR angle and improved sensitivity of 400-420 nm/RIU above the TIR angle. On the other hand, as follows from Fig. 3.5b, substrate-related mode appears to be weakly sensitive to variations of RI (50-55 nm/RIU) independently of angle of incidence (below or above TIR).

Even when sensitivities of PSLR modes can be obtained within diffraction theory[38], a detailed consideration of the phenomenon should take into account not only the dependence of diffraction edge position on RI of the environment, but also accompanying effects such as a certain mismatch of actual PSLR positions with that of the Rayleigh cut-off wavelengths and evanescent near-fields in the case of ATR geometry. However, in the first approximation, this sensitivity should correlate with the sensitivity of the diffraction edge. The position of this Rayleigh cut-off wavelength for water and substrate modes in direct geometry can be derived as follows:

$$\pm\lambda_{R\_Dir}^{Wat} = an_{Wat}(sin\theta \pm 1) \quad (3.3a)$$

$$\pm\lambda_{R\_Dir}^{Sub} = a(n_{wat}sin\theta \pm n_{sub}) \quad (3.3b)$$

In direct geometry, sensitivities of medium $PSLR_{wat}$ and substrate $PSLR_{sub}$ modes to variations of refractive index of the aqueous medium can be expressed as follows:

$$S_{dir}(PSLR_{wat}) = \frac{\partial \lambda_{R\_Dir}^{wat}}{\partial n} = \frac{\partial}{\partial n}[an(sin\theta \pm 1)] = a\left(sin\theta \pm 1 + \frac{\delta sin\theta}{\delta n}\right) \quad (3.4a)$$

$$S_{dir}(PSLR_{sub}) = \frac{\partial \lambda_{R\_Dir}^{Sub}}{\partial n} = \frac{\partial}{\partial n}[a(nsin\theta \pm n_{sub})] = a\left(sin\theta + n\frac{\delta sin\theta}{\delta n}\right) \quad (3.4b)$$

where *n* is refractive index of ethanol/water mixture. Since the angle of light incidence at water/substrate interface θ can be derived through the angle of light incidence α at the air/water interface (this interface is located at the flow cell entrance window) by the Snell's law $n_{air} \cdot sin\alpha = n \cdot sin\theta$, two latter equations can be rewritten as:

$$S_{dir}(PSLR_{wat}) = a\left(sin\theta \pm 1 - \frac{n\, n_{air} sin\alpha}{n^2}\right) = a(sin\theta \pm 1 - sin\theta) = \pm a \quad (3.5a)$$

$$S_{dir}(PSLR_{sub}) = a\left(sin\theta - \frac{n\, n_{air} sin\alpha}{n^2}\right) = a(sin\theta - sin\theta) = 0 \quad (3.5b)$$

Thus, according to simplified diffraction theory, sensitivity of the medium mode ($PSLR_{wat}$) to RI in direct geometry is supposed to be of the order of the period of the structure (a nm/RIU), while the substrate mode should be insensitive to RI variations.
Similarly, sensitivities of medium $PSLR_{wat}$ and substrate $PSLR_{sub}$ modes in ATR geometry are mainly determined by positions of corresponding Rayleigh cut-off wavelength:

$$\pm\lambda_{R\_ATR}^{Wat} = a(n_{sub} sin\theta \pm n_{Wat}) \quad (3.6a)$$

$$\pm\lambda_{R\_ATR}^{Sub} = an_{sub}(sin\theta \pm 1) \quad (3.6b)$$

Therefore, these sensitivities can be expressed as follows:

$$S_{ATR}(PSLR_{wat}) = \frac{\partial \lambda_{R\_ATR}^{wat}}{\partial n} = \frac{\partial}{\partial n}[a(n_{sub} sin\theta \pm n)] = \pm a \quad (3.7a)$$

$$S_{ATR}(PSLR_{sub}) = \frac{\partial \lambda_{R\_ATR}^{Sub}}{\partial n} = \frac{\partial}{\partial n}[an_{sub}(sin\theta \pm 1)] = 0 \quad (3.7b)$$

Here, again, the sensitivity of the medium mode ($PSLR_{wat}$) in ATR appears to be linked to the period of the structure (*a* nm/RIU), while the substrate mode should be insensitive to these variations.

Experimental assessment of sensitivity of $PSLR_{wat}$ mode in direct geometry (Fig. 3.5a) and ATR geometry with incidence below TIR angle (Fig. 3.5b) confirm these theoretical predictions, as these sensitivities are in the range of 310-360 nm/RIU and 340-340 nm/RIU, respectively. However, a higher sensitivity of this mode in ATR geometry (400-420 nm/RIU) under angles exceeding the TIR angle is a pleasant surprise taking into account the fact that this sensitivity does not originate from diffraction theory

considerations. Results show that this effect is probably related to the involvement of evanescent wave under TIR, which can additionally react on RI variations. Another interesting issue is related to the observation of the dependence of substrate related modes $PSLR_{sub}$ on RIU variations for direct and ATR geometries (190-200 nm/RIU and 50-55 nm/RIU, respectively) as shown in the Fig. 3.5, although the diffraction theory cannot predict these dependencies. It is believed that such a discrepancy of experiment and theory is related to too simplified model used in calculations. In this model, the sensitivity of the diffraction edge is considered, which is not far from actual resonances for oblique angles, but still does not match them. Nevertheless, even if the deviation from Rayleigh wavelength is small, it changes fast with *n*, angle, etc, as the observed PSLR are very dispersive (Fig. 3.3 c, f; Fig. 3.4 c, f), providing non-zero sensitivities for substrate modes. In addition, the proposed theory does not take into account the excitation of evanescent wave under illumination of arrays at angles larger than 63° Deg. using ATR geometry, which can explain unexpectedly high sensitivity of medium mode under these conditions (Fig. 3.5b).

Let us now consider phase sensitivity of plasmonic surface lattice resonances. It should be noted that this parameter does not directly correlate with the spectral sensitivity. Indeed, as showed above, spectral sensitivity of $PSLR_{wat}$ is directly linked to the period of used metamaterial arrays and does not depend on width of depth of generated resonances. On the other hand, phase sensitivity is independent of the period of the arrays, but is determined by the sharpness of phase jump, which in turn is critically dependent on the depth of resonances ("light darkness" in the resonant minimum)[41]. As an example, one can expect high phase sensitivity for double 134-nm particle arrays, which provide very deep resonances under ATR geometry leading to extreme phase features (Fig. 3.4 b and e, respectively).

As shown in Figure 3.5c, the replacement of 80% solution of ethanol (80% ethanol / 20% water) by pure ethanol, corresponding to a change of RI by 4.4×10^{-3} RIU, leads to a dramatic shift of phase curve (Fig. 3.5c) and a huge (~205° Deg.) change of phase at the optimal wavelength of about 899 nm (inset to Fig. 3.5c). Based on this data, the phase sensitivity can be now estimated, which appears to be equal to 5.7×10^4 Deg. of phase per RIU. Taking into account the level of noises of phase-sensitive detection schemes, one can then estimate the low detection limit (LOD), which characterizes minimal variation of RI detectable by an optical transducer. It is clear that LOD should be very high for ellipsometry, as commercial ellipsometers are typically designed for optical characterization of films and not for sensing tests, and thus have a high level of noises. However, as shown in a recent study[46], resolution of phase measurements using an advanced photoacoustic modulator-based scheme of phase detection and a thermally stabilized flow cell system can be better than 5×10^{-3} Deg. Under this phase resolution, projected LOD is estimated to be lower than 8×10^{-8} RIU, which is better than in commercial amplitude-sensitive SPR units by almost 2 orders of power magnitude[20,21]. Notice that the minimal variation of RI that could be introduced into the system using calibrated ethanol-water mixtures was of the order of 4×10^{-3} RIU. Smaller variations of

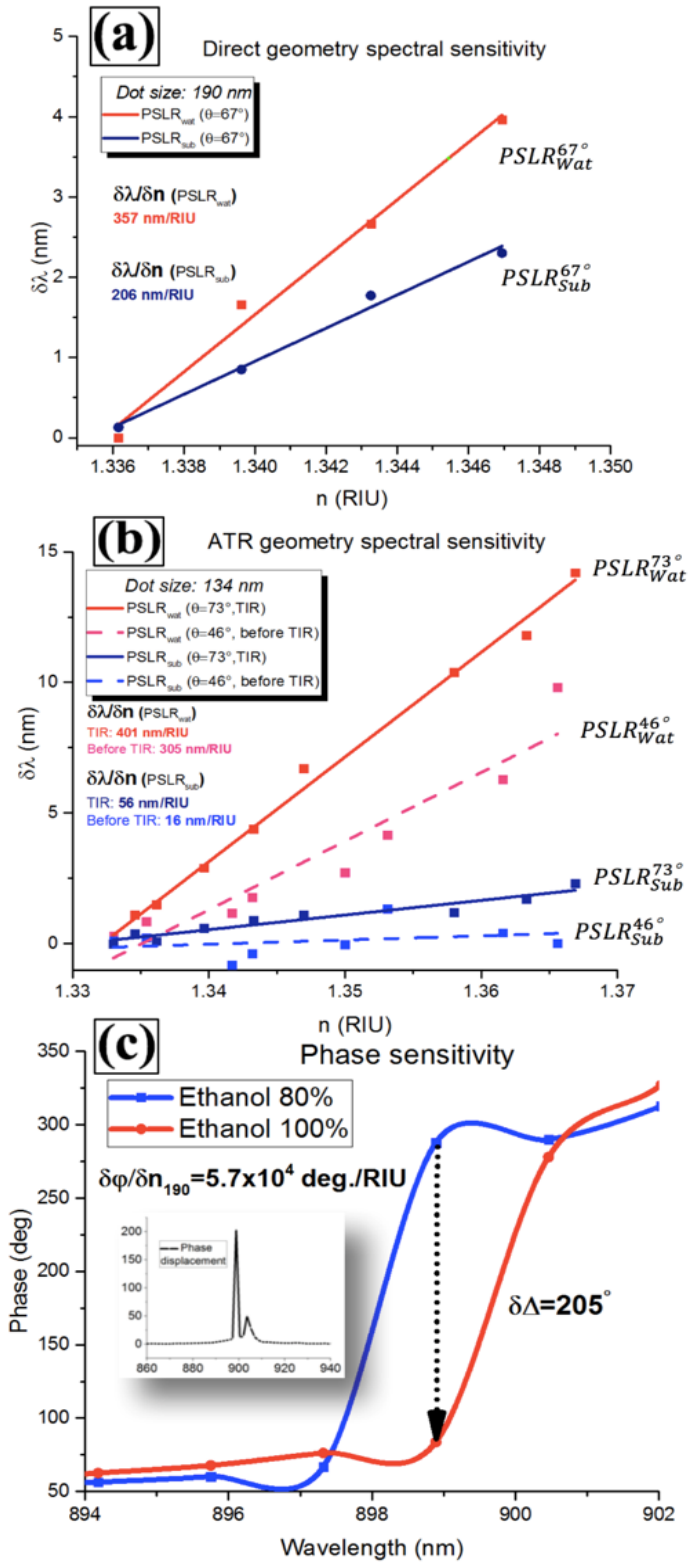

Fig. 3.5 Sensitivity measurements. (a) Direct geometry: Spectral response of medium $PSLR_{wat}$ (red) and $PSLR_{sub}$ (blue) modes excited over single 190 nm particle array (period 320 nm) to RI changes conditioned by pumping of different ethanol/water mixtures through the flow cell; (b) ATR geometry: spectral response of medium $PSLR_{wat}$ (red) and $PSLR_{sub}$ (blue) modes excited over double 134 nm particle array (period 320 nm) before (dashed) and after (solid) TIR to changes of RI. (c) Typical spectral dependences for Δ under the change of RI by 4.4×10^{-3} RIU. The inset shows the difference phase signal δΔ for phase curves indicated in the figure.

RI could not be resolved due to too high level of noises, conditioned by liquid pumping system and flow cell. As shown in Fig. 3.5c, such a variation of RI already exceeded the dynamic range of phase measurements, which inevitably lowered the estimation of phase sensitivity. In a previous study[45], phase sensitivity of similar metamaterial nanoparticle array was assessed using a gas model, which made possible the introduction of much smaller variations of RI of the medium by employing a calibrated mixture of gases with known difference of RI (Ar and N_2). In this case, the system was in the optimal dynamic range for the whole set of phase measurements, while the recorded sensitivity exceeded 10^6 Deg. of phase shift per RIU, giving access to ultrasensitive measurements of RI with the detection limit lower than 10^{-9} RIU.

Thus, ultra-narrow PSLRs over ordered nanodot array metamaterials can exhibit fairly good sensitivity (300-400 nm/RIU), conditioned by the periodicity of used structures and extremely high phase sensitivity, conditioned by a very low light intensity in the resonance minimum (nearly complete light darkness). It is clear that narrower PSLRs (2-20 nm FWHM) compared to LSPR (80-100 nm FWHM) and SPR (50 nm FWHM) can be used to improve the precision of biosensing tests using plasmonic biosensors. To take into account the sharpness of the resonance and thus examine system efficiency to sensitively measure small wavelength changes, one normally uses a characteristic "Figure of Merit" (FOM) parameter[88]: FOM=$(\Delta\lambda/\Delta n)(1/\Delta\omega)$, where $\Delta\omega$ is the width of resonance at FWHM and $\Delta\lambda$ is the resonance shift for a Δn refractive-index change. The essence of FOM is straightforward: it adequately quantifies the sensing potential of plasmonic modes in configurations similar to those used in commercial instruments. Typical FOMs do not exceed 8 and 23 for the sensors based on LSPR[24,25] and SPR[89], respectively. The employment of PSLRs enables one to increase these parameters up to 10, 100 and more. In particular, in these experiments FOM reached 183.8, which is in a good agreement with the earlier works there it reached ~ 200-250[45]. As another illustration, it was recently shown[90] that PSLRs in ordered metamaterial arrays of gold nanoparticles can offer a sensing performance that is at least an order of magnitude higher than uncoupled LSPRs associated with disordered particle arrays. Other studies experimentally demonstrated a high-performance RI-sensitive sensor based on PSLR, while its FOM reached 38 normal incidence[91]. However, the main advantage offered by PSLR is related to their phase sensitivity, which can be extremely high (over 10^6 Deg. of phase shift per RIU change). In general, the combination of ultrahigh point sensitivity (provided by phase interrogation) and fairly high sensitivity for a wider dynamic range of measurements (provided by spectral interrogation) looks like a very attractive basis for the development of versatile biosensing platform based on PSLR for characterization of biomolecular interactions.

3.5 Feasibility in biosensing

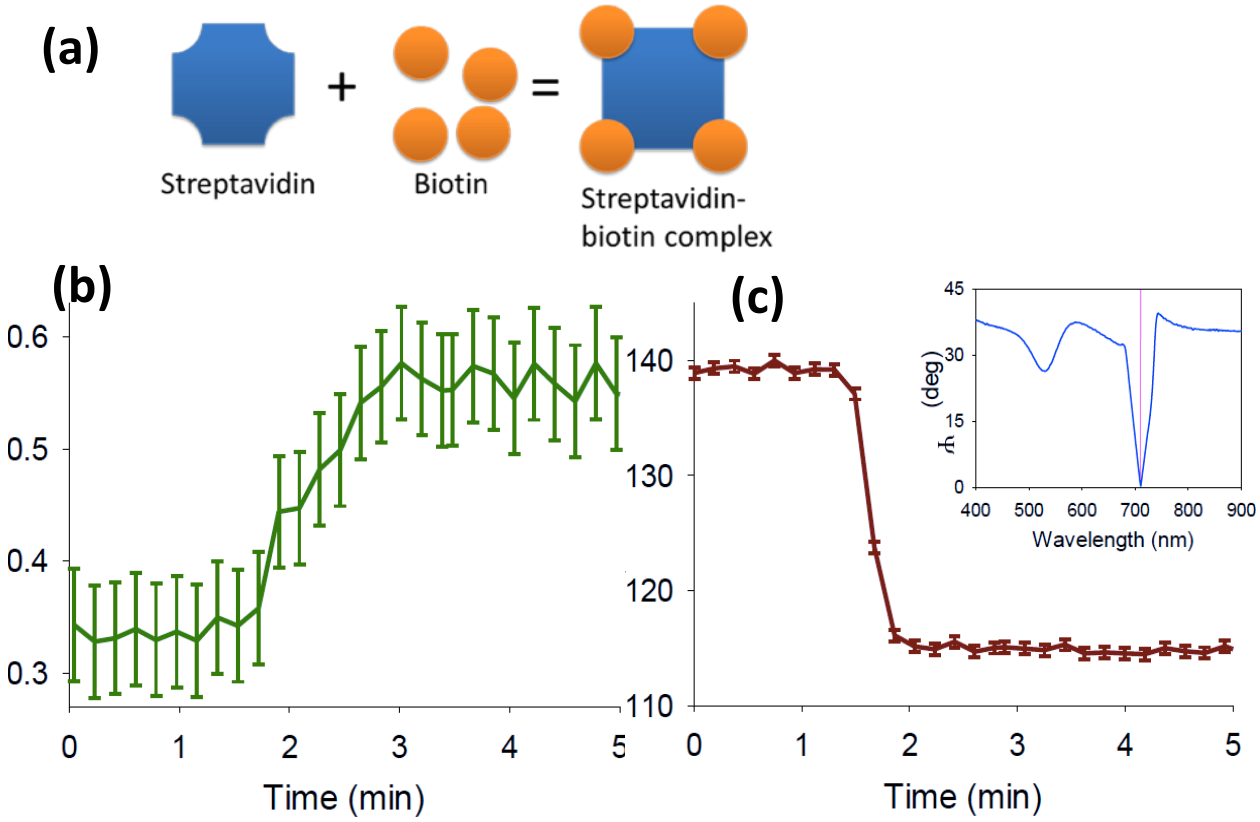

Fig. 3.6 Assessment of plasmonic metamaterials for biosensing using Streptavidin-Biotin affinity model. (a) Typical schematics of streptavidin-biotin binding; Evolution of Ψ (b) and Δ (c) for medium-related mode $PSLR_{wat}$ excited over double 134 nm particle array with time as SA molecules bind to functionalized Au dots measured at λ =710 nm and θ=53°. Inset: Ψ(λ) for the incidence angle of 53°.

In order to assess the applicability of plasmonic metamaterial structures to biosensing, a set of measurements was performed using a well-calibrated protocol based on the Streptavidin-Biotin affinity model[24]. In the experiment, variations of ellipsometric parameters Ψ and Δ at the resonant minimum were recorded, corresponding to the excitation of a medium-related mode $PSLR_{wat}$ for a sample of double 130-nm nanoparticles (these conditions were achieved for the light wavelength of 710 nm and angle of incidence of 53°). As demonstrated in Fig. 3.6, the attachment of SA led to changes in both reflectivity Ψ and phase Δ, which is consistent with the reaction of metamaterial system to the change of RI of the biological layer contacting plasmon-supporting gold. Here, the signal came to its saturation 3 minutes after the beginning of experiment, which corresponded to binding to all the biotin sites by SA molecules (as shown in Methodology section, this case corresponds to the attachment of 20-100 SA molecules per nanodot). It is important that this process was accompanied by ~25° change of phase Δ. Taking into account that the phase resolution of used ellipsometer was about 0.5 Deg., we can

estimate experimental sensitivity of about 1-4 molecules per nanodot or 100 fg/mm^2. As was shown previously[46], measurements for a thermally stabilized system with advanced phase detection can be better than 5×10^{-3} deg., which means that in principle one could resolve the attachment of 0.004-0.02 SA molecules per nanodot or <1 molecule attached per square micron area of the nanostructured devices or 1 fg/mm^2. This detection limit is 2-3 orders of power magnitude better than previously achieved for the conventional plasmonic nanosensors based on light intensity rather than phase changes[24,25].

3.6 Comparison of PSLR-based and a conventional SPR-based biosensors

In this part properties and sensitivities of two different plasmonic sensing configurations based on PSLR and SPR are compared[43]. Fig. 3.7a shows spectral dependences for Ψ and Δ when classical Kretschmann-Raether prism geometry of plasmon excitation over a thin Au film is employed. Here, a high-quality Au film with the thickness of 50 nm is used, which is nearly optimal for the excitation of SPR. One can see that the SPR effect is efficiently produced and the width of the resonance is about 30 nm FWHM. The generation of the resonance is accompanied by a jump of light phase Δ of about 100 Deg. near the very minimum of the resonant curve. In this case, light intensity in the minimum exceeds 8 Deg. corresponding to 15% light intensity compared to out-of-resonance conditions. Such a high light intensity in the SPR minimum can be explained by a relatively rough gold film surface, leading to efficient conditions of photon/plasmon coupling for a variety of wave numbers k of incident photons. The roughness of Au sensor can be decreased by the employment of alternative graphene-copper[86] or graphene-gold[92] architectures for plasmon excitation, but these novel geometries require a separate development of sensing protocols for graphene surface. It should be noted that even a rigorous optimization of conditions of gold film deposition cannot dramatically improve the depth of the resonance SPR feature and the reported values of minimal intensity in the SPR minimum always exceed 9-10%[27]. It is obvious that relatively high intensities in the SPR minimum should limit the sharpness of the phase jumps and its response to refractive index variations. The best reported phase sensitivities for SPR are of the order of (1-9) $\times 10^4$ Deg. of phase per RIU change[27,41].

Thus, Au films deposited on a substrate always have some surface roughness, which conditions a non-zero intensity of light in the resonance and a related smoothened jump of light phase. As was shown in Section 3.3, this limitation on the *light darkness* of plasmonic resonances can be overcome by the employment of 2D nanoparticle arrays enabling diffractive coupling of LPR. Fig. 3.7b shows an example of PSLR having extremely narrow width and nearly zero intensity of reflected light in resonance. It is also visible that phase experiences Heaviside-like jump under such a deep resonance.

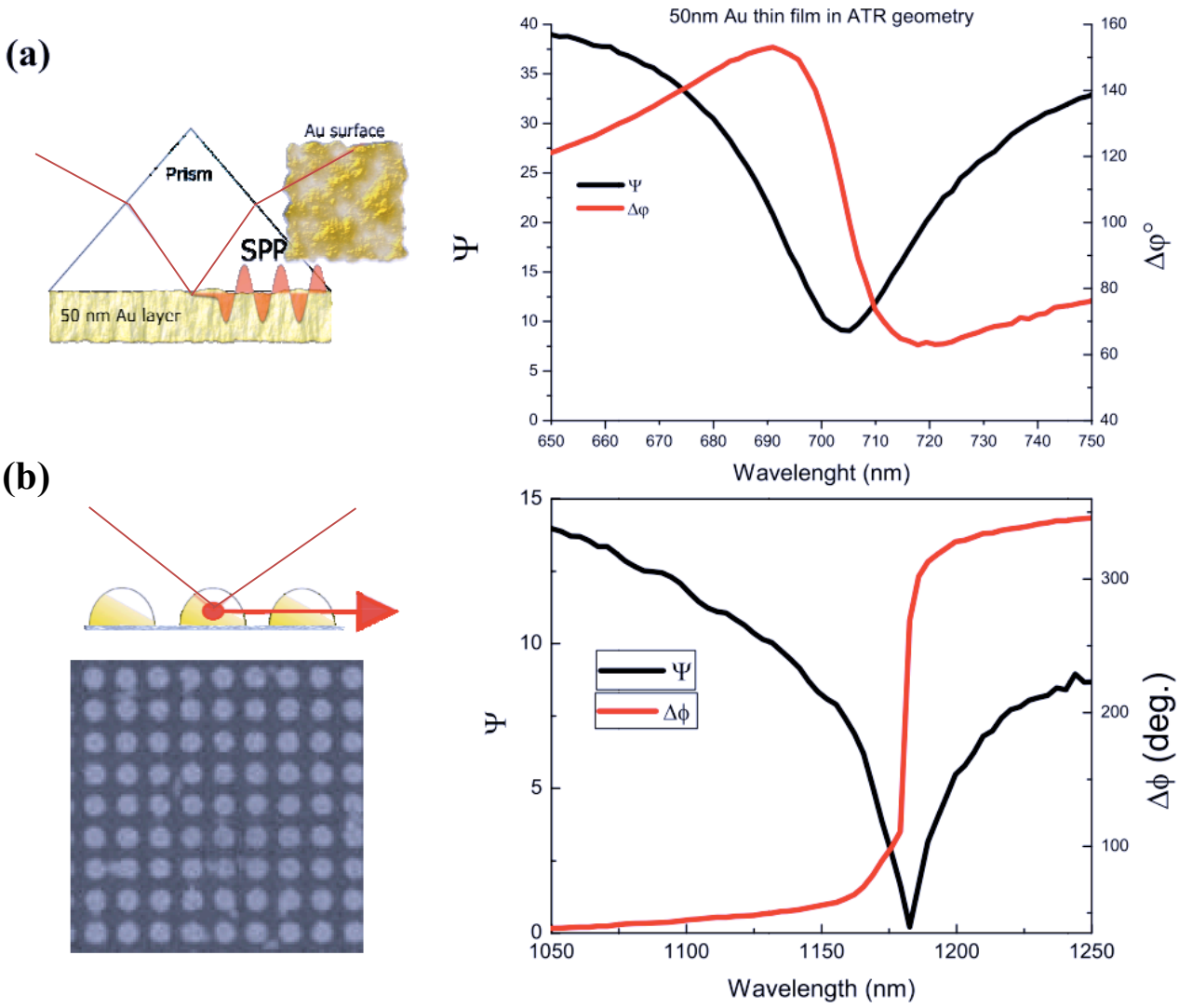

Fig. 3.7 Experimentally obtained spectral dependencies for amplitude intensity and phase characteristics of light in plasmonic resonance conditions. (a) Excitation of surface plasmon polaritons over a 50 nm Au thin film in Kretschmann-Raether prism geometry (classic SPR configuration). Finite film roughness limits minimal possible ψ value, leading to a smoothened phase jump in extremum point; (b) Diffractively coupled array of Au nanodots in direct illumination configuration. Clearly, PSLR peak is more pronounced, much narrower and minima is close to zero, resulting in a sharp phase jump in resonance conditions.

Let us now compare sensitivities of SPR and PSLR. Fig. 3.8a shows a shift of position of SPR (black) and PSLR (red) dips as a function of the refractive index of the medium, as conditioned by different concentrations of glycerin. It is visible that an increase of RI due to the glycerin addition leads to a red shift of the resonance for both configurations, while the resonant position linearly shifts under a relatively wide range of refractive index variations (~0.03 RIU). The slope of the linear dependence evidences the sensitivity of 400 nm/RIU for PSLR, which is consistent with the results of measurements described in Section 3.4 and sensitivity assessments using nanoperiodic plasmonic

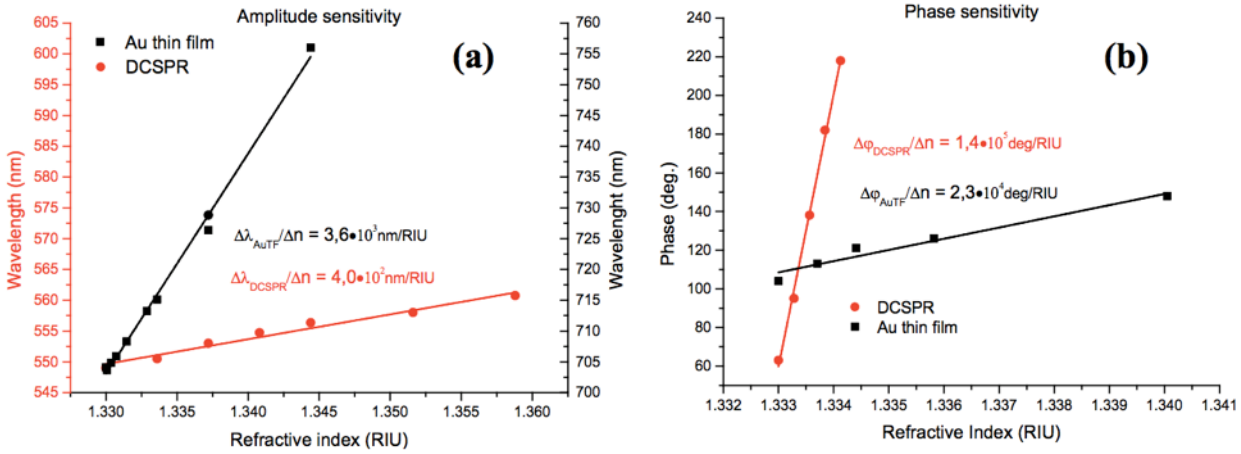

Fig. 3.8 Experimentally measured optical responses of the (a) spectral resonance peak position and (b) phase shift to a refractive index variation for conventional SPR device with 5 nm Au thin film (black) and diffractively coupled LSPR nanodot array (red).

transducers, including uncoupled plasmonic arrays[24,25] (200-300 nm/RIU) and nanohole arrays[31,32] (300-400 nm/RIU). As shown in Fig. 3.8a thin film-based SPR using the Kretschmann-Raether prism arrangement provides almost an order of magnitude higher spectral sensitivity (3600 nm/RIU), compared to PSLR. This result confirms previously discussed limitation of LSPR related to diffractive coupling nature of localized plasmons as the spectral sensitivity in diffractive phenomena is typically of the order of structure periodicity $\Delta\lambda/\Delta n \sim d$[38].

However, this diffraction-related limitation is not valid for phase sensitivities. Indeed, as shown in Fig. 3.7b, phase sensitivity in the case of SPR is rather moderate (2.3×10^4 Deg. of phase per RIU), which is explained by a relatively smoothened phase feature under thin film-based SPR (Fig. 3.7a). On the other hand, phase sensitivity in the case of PSLR can easily exceed 10^5 Deg. of phase per RIU (Fig. 3.8b), which is explained by a much lower light intensity in the minima of diffractively coupled resonances (Fig. 3.7b).

3.7 Summary

In this chapter, for the first time conditions of excitation and properties of diffractively coupled plasmonic surface lattice resonances over 2D metamaterial array of single and double nanoparticles in direct and ATR geometries were established. Medium-related $PSLR_{air}/PSLR_{wat}$ and substrate-related $PSLR_{sub}$ plasmonic modes, corresponding to the coupling of individual plasmon oscillations at medium- and substrate-related diffraction cut-off edges were identified.

It was shown that PSLR excited both in direct and ATR geometries can have extremely small width (down to a few nm FWHM). Sensitivities of these modes to variations of refractive index of adjacent sample dielectric medium were assessed. The determined spectral sensitivity of medium-related PSLRs (300-400 nm/RIU) is

conditioned by nanostructure periodicity, while substrate-related modes showed much lower sensitivity. It was also shown that PSLRs can provide extremely low intensity (down to 10^{-6} Deg.) in the resonance conditions (light darkness), leading to the generation of extremely sharp jump of phase of light in the very minimum of the resonance. The employment of this jump can give rise to very high phase sensitivity.

Sensitivities of PSLR and SPR in the Kretschmann-Raether geometry were directly compared. It was shown that despite much lower spectral sensitivity (400 nm/RIU compared to 3600 nm/RIU) PSLR can exhibit much higher phase sensitivity (>10^5 Deg./RIU compared to ~10^4 Deg./RIU). Thus, despite a considerable handicap of PSLR in terms of amplitude sensitivity compared to conventional SPR, the employment of phase sensitivity completely compensates this gap: phase sensitivity in the case of PSLR can drastically outperform the relevant parameter for SPR. To the best of my knowledge, PSLRs outperform all plasmonic counterparts in terms of phase sensitivity.

Finally, the feasibility of PSLR for biosensing was demonstrated using standard streptavidin-biotin affinity model. Combining advantages of nanoscale architectures, including drastic concentration of electric field, possibility for manipulations at the nanoscale and high phase and spectral sensitivities, $PSLR_s$ promise the advancement of current state-of-the-art plasmonic biosensing technology toward single molecule label-free detection. It is also important that PSLR nanosensor configurations are still compatible with miniaturized, cost-efficient plasmonic biosensing architectures such as ones based on integrated waveguides[93], Si-based[94] or Bragg reflector coupler-based[95] micro-platforms.

Chapter 4

3D plasmonic metamaterial sensor

CONTENTS

4.1 Introduction

As it was explained in Chapter 3, the spectral sensitivity of 2D plasmonic arrays is an order of magnitude lower compared to SPR. Indeed, the sensitivity of uncoupled nanoparticle array is typically 200-500 nm/RIU[25,47], while the sensitivity of nanohole array is 300-400 nm/RIU[31–34]. As shown in Chapter 3, despite extremely high quality of PSLR resonances and their high phase sensitivity, spectral sensitivity of PSLR is also of the same order 300-400 nm/RIU. The sensitivity problem of 2D periodic plasmonic arrays is related to diffractive nature of coupling light to plasmons and links the sensitivity to structure periodicity $\Delta\lambda/\Delta n \sim d$[38], which is typically of the order of hundreds of nm.

In this Chapter, for the first time conditions of excitation of plasmons in 3D geometry of plasmonic woodpile-based crystals are considered[96–98]. It is shown that such a transition from 2D to 3D nanoarchitectures can break the diffraction-related sensitivity limitation of 2D nanoperiodic arrays. Under these conditions, a novel plasmon mode can be excited, providing very high sensitivities in both spectral (>2600 nm/RIU) and phase ($>3 \times 10^4$ deg. of phase per RIU) interrogations.

This work was done in a framework of MINOS project in a collaboration with group of Prof. M. Farsari from IESL-FORTH, Crete. FORTH was responsible for structure fabrication, while LP3 provided design of structures and carried out optical characterisation and sensitivity tests. The results of these research were published in papers [Th-2], [Th-4] and [Th-5].

4.2 Materials and methods

4.2.1 Materials

The materials used here are a zirconium-silicon organic-inorganic hybrid materials doped with tertiary amine moieties. Their synthesis has been described elsewhere[99]. The main material components are methacryloxypropyl trimethoxysilane (MAPTMS), zirconium propoxide (ZPO, 70% in propanol) and 2-(dimethylamino) ethyl methacrylate. (DMAEMA) is added to act as a quencher, and to provide the metal-binding moieties. Michler's ketone, 4,4-bis(diethylamino) benzophenone (BIS) is used as a photoinitiator. MAPTMS is first hydrolysed using HCl solution (0.1 M) at a 1:0.1 ratio. After 5 minutes, the hydrolyzed MAPTMS is slowly added to the ZPO at 8:2 molar ratio. After stirring for 15 minutes, DMAEMA is added. The MAPTMS:DMAEMA molar ratio is 7:3. Finally, the photoinitiator, at a 1% w/w concentration is added to the mixture. After

stirring for a further 20 minutes, the composite is filtered using a 0.22 μ m syringe filter. The samples are prepared by drop-casting onto 100 micron-thick silanized glass substrates, and the resultant films are dried in an oven at 50 °C for 10 minutes before photopolymerization by DLW. After the completion of the component build process, the samples are developed for 20 minutes in a 30:70 solution of 1- propanol:isopropanol, and further rinsed with isopropanol. All chemicals are obtained from Sigma-Aldrich and used without further purification.

4.2.2 Fabrication of woodpile metamaterial structures

The structures fabricated are PhCs using the FCC woodpile geometry, with interlayer periodicity of 700 nm. General process is illustrated on Fig. 4.1a. The experimental setup employed for their fabrication has been described elsewhere[99,100]. A Ti: Sapphire femtosecond laser (Femtolasers Fusion, 800 nm, 75MHz, <20 fs) is focused into the photopolymerisable composite using a high numerical aperture focusing microscope objective lens (100×, N.A. = 1.4, Zeiss, Plan Apochromat). Sample movement is achieved using piezoelectric and linear stages, for fine and step movement, respectively (Physik Instrumente). The average power used for the fabrication of the high-resolution structures is 4.0 mW, measured before the objective, while the average transmission is 20%. The scanning speed is always set to 20 μ/s. The PhCs used for these experiments consisted of 7 unit cells, and average rod thickness (including the silver layer) was about 280 nm.

Metallization of woodpile metamaterial arrays. The metallization process followed here is a modification of the one described in ref. [100]. It consists of three steps: seeding, reduction and silver plating.

1) **Seeding.** The samples were immersed in a 0.05 mol/L $AgNO_3$ aqueous solution at room temperature for 38 hours minimum. This was followed by thorough rinsing with double distilled (d.d.) water, by immersing the sample twice in a water container, with fresh water for each immersion. They were left to dry at room temperature.

2) **Reduction.** An aqueous sodium borohydride ($NaBH_4$) solution 6.6 M was prepared some hours (>4 h) before the immersion of the samples. The solution was very well mixed and kept uncovered for a couple of hours to get rid of trapped air bubbles. The samples were subsequently dipped in the solution for 22 hours to reduce the silver ions and form silver nanoparticles. The samples were subsequently washed thoroughly in fresh d.d. water and left to dry.

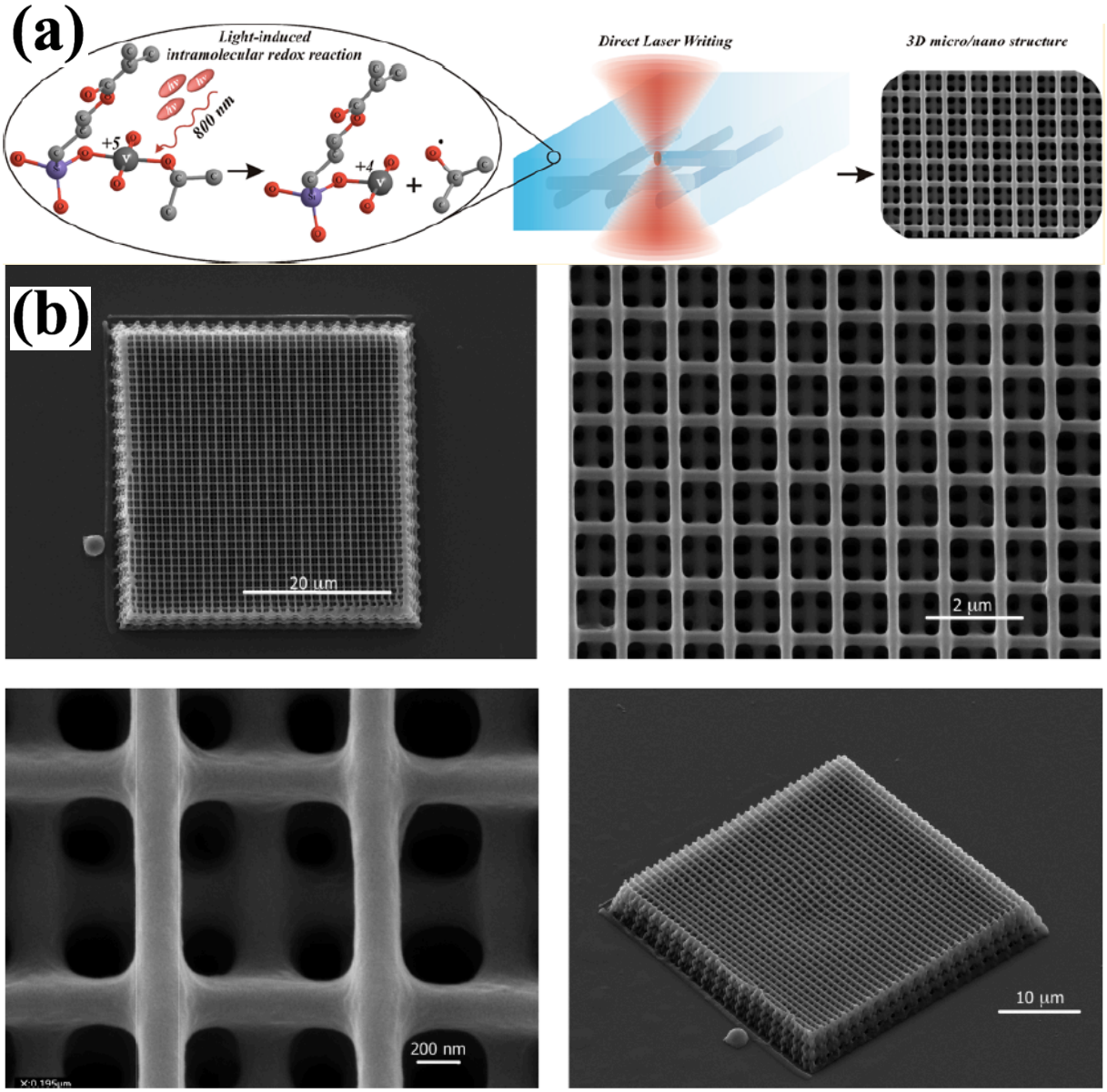

Fig. 4.1 (a) Woodpile structure manufacturing process. Photopolymerisable monomer composite is polymerized in focal spot under exposition of laser illumination;
(b) Several TEM images of final nanostructure.

3) **Silver plating.** A 0.2 M $AgNO_3$ aqueous solution was mixed with 5.6% NH_3 (28% in water) and 1.9 M glucose ($C_6H_{12}O_6$ > 98%) as a reducing agent, at volumetric ratio 5:3:8. The samples were immersed in the solution for a few minutes, and were removed before it became dark. In the meanwhile, a fresh solution was prepared to replace the old one. This process was repeated two times. The samples were subsequently washed twice by immersion in fresh d.d. water for a few minutes.

4.3 Conditions of excitation and properties of plasmons in 3D woodpile metamaterial

The design of proposed 3D plasmonic metamaterial is based on a classic woodpile photonic crystal geometry[101], consisting of layers of one-dimensional rods with a stacking sequence that repeats itself every four layers, as shown in Fig. 4.2(a, b). The distance between four adjacent layers is *c* and, within each layer, the axes of the rods are parallel to each other with a distance *d* between them (Fig. 4.2b). The adjacent layers are rotated by 90°. Between every other layer, the rods are shifted relative to each other by $d/2$. For the case of $\frac{c}{d} = \sqrt{2}$, the lattice can be derived from a face-centered-cubic (FCC) unit cell with a basis of two rods. Typical scanning electron microscopy (SEM) images of 3D woodpile structures are shown in Fig. 4.2c. The period of the structures and the diameter of metalized nanorods were 700 nm and 350 nm, respectively.

The experiments showed that woodpile-based structure does not transmit light evidencing a complete domination of plasmonic phenomena over interference effects in photon crystals[102]. The structure still can demonstrate diffraction effects, but all diffraction beams are of very small intensity, several orders of magnitude smaller than the intensity of reflected light. In tests, properties of light reflected from the structured in zero diffraction order are examined by using ellipsometry (Woollam M-2000 system). As shown in Fig. 4.3(a, b), the light reflected from the woodpile metamaterial leads to the generation of deep resonances, obviously related to the excitation of plasmon modes over the metamaterial matrix. The resonances are observed at 700 nm and 625 nm when the structure is in contact with air or water environments, respectively, and the relevant angles of light incidence are 60 deg. and 56 deg. Fig. 4.3(c, d) demonstrate the dependence for the reflectivity of p-polarized (r_p) and s-polarized (r_s) components of the light reflected from the metamaterial. One can see that the main resonant feature is generated in p-polarized light. Here, the resonances are characterized by a substantial absorption of light in the near-infrared region. It is important that for both air and water environments the light intensity in the resonances is very low. Indeed, the intensity within the r_p minimum does not exceed 10^{-6} % and 10^{-4} % for air and aqueous environments, respectively. As follows from the topological properties of phase[9,41], such “light darkness” at the resonances should lead to singularities of phase of reflected light. Indeed, one could observe very sharp phase jumps when the metamaterial was in contact with air (Fig. 4.3a). Although for the aqueous environment the phase jump is slightly smoothened, it is still prominent (Fig. 4.3b). The total phase variation Δ is about 240 deg. and 270 deg. in the case of air and water environments, respectively. For used parameters of the system the phase jump was much sharper for air ambience compared to the aqueous one. To confirm the observed effect, a different sample with the period of 750 nm was analysed (Fig. 4.4a) with the resonance found around 460 nm when the structure was in contact with air environment. In this case, the resonances were excited around 67 Deg. and peak shape and its behaviour appeared to be similar to the previous case.

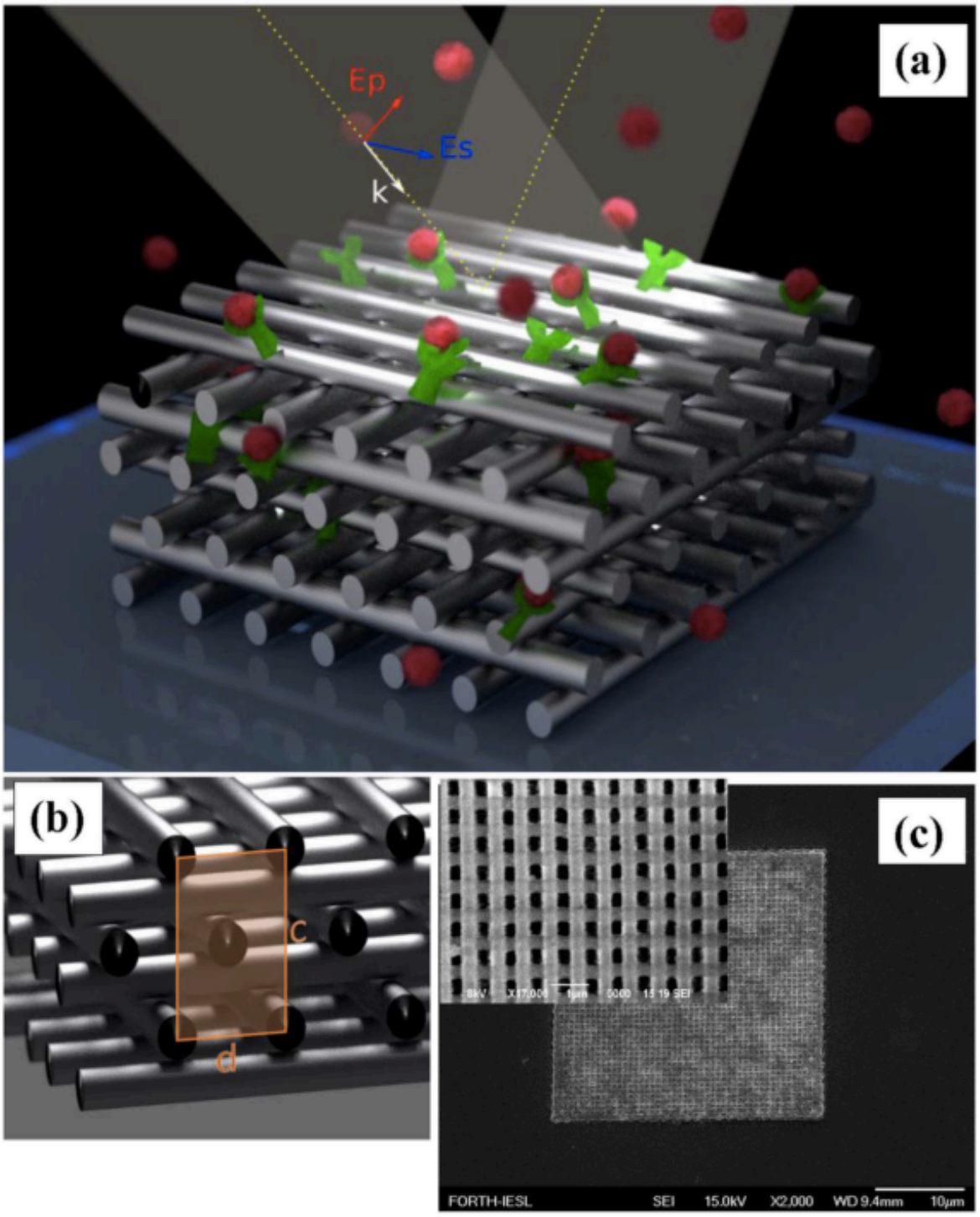

Fig. 4.2 3D plasmonic metamaterial based on Ag-coated woodpile crystal. (a) Schematic illustration of biosensing, using metamaterial. A receptor (green) is immobilized inside the metalized woodpile structure, while a selective donor-partner (red) binds into receptor sites, leading to a change of parameters for the reflected light; (b) Schematic representation of a woodpile crystal. Structure unit cell is highlighted in orange; (c) SEM image of woodpile metamaterial structure produced by a multiphoton laser polymerization, followed by Ag-based metallization process.

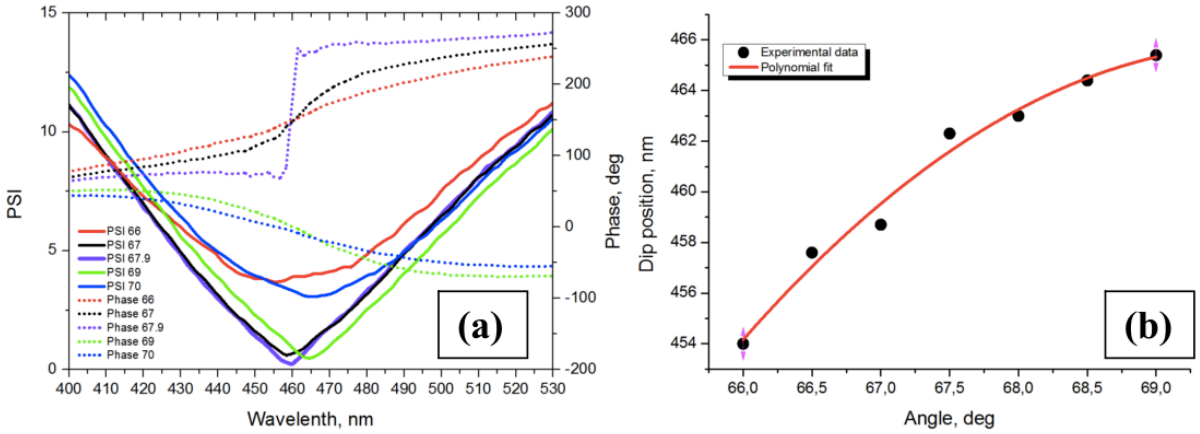

Fig. 4.4 (a) Experimental spectral dependencies of ellipsometric reflection Ψ and phase Δ for different angles of light incidence onto the metamaterial structure (metamaterial is in contact with air). (b) Dispersion curve describing conditions for the generation of resonances (combinations of the resonance angle of incidence and wavelength) constructed on the basis of experimental data.

In order to assess the potential of the 3D woodpile-based plasmonic crystals in biosensing, it is important to clarify the nature of the plasmon modes responsible for the observed resonances. First of all, elongated metal-coated woodpiles are expected to support delocalized (propagating) plasmons, which can be excited e.g., due to the presence of periodic modulations, similar to the case of nanohole arrays in thin metal films[31,32]. The excitation of such delocalized plasmonic mode is indeed confirmed by a characteristic ascending course for optical dispersion, shown in Fig. 4.4b, which is obtained on the basis of experimentally determined conditions of resonance generation (combinations of the resonance angle of incidence and wavelength). It is interesting that the whole range of optical energy variations appears to happen under a very narrow range of angles of incidence ($\Delta\theta$ <3° deg.), corresponding to a very narrow range of wave numbers $\Delta k \sim 0.1\ \mu^{-1}$. Out of this narrow range of angles, the plasmons are not excited and the resonances disappear, which contrasts to similar data for the generation of diffractively coupled PSLR (Chapter 3). On the other hand, the presence of nodes in woodpile contacts can favour the excitation of localized plasmons. In this case, the Finite-Difference Time-Domain (FDTD) approach can be used to determine the localization of the electric field caused by the LSPR excitation. Here, for relatively thin Ag coatings (<20 nm), metal-covered woodpile photonic crystals can be modelled as core-shells[103], but due to the excessive number of interfaces involved, the FDTD consideration is typically limited to 2D structures. In this case, the thickness of the metal coating (30–40 nm) is larger than the skin depth for the electromagnetic field (~20 nm for Ag in the visible range). Therefore, to a first approximation woodpiles may be treated as solid metal nanorods. Such an approach drastically simplifies FDTD simulations and makes possible the analysis of the electric distribution inside the 3D plasmon crystal matrix. FDTD package from Lumerical Solutions Inc. was employed, assuming that the angle of incidence of the p-polarized beam on the structure is 60°. The result of such a numerical description is given in Fig. 4.5c. One can see that the electric field is indeed concentrated at the lattice nodes,

corresponding to the positions of the transverse bars with respect to the light incidence plane. Such a concentration of the electric field can only be explained by the generation of localized plasmon resonances. For the first layer, the electric field is concentrated at the peaks of the nodes, while for the inner layers, the main point of field concentration shifts from the top of the nodes, which is probably explained by the inclined geometry of the illumination of the woodpiles by external light. As it follows from the analysis, a remarkable concentration of electric field takes place only for the top 8–10 woodpile layers. However, one has to notice that the approximation of Ag-coated woodpiles as solid metal nanorods presents an extreme case, which is characterized by maximum light absorption. The extrapolation of the FDTD approach to real structures having a finite thickness of metal coating is supposed to increase the penetration depth of the light electric field towards much deeper layers. A rigorous consideration of structures having precise experimental parameters is now in progress and will be published elsewhere. The general idea here is, that any structure may be macroscopically described by its complex optical constants. Moreover, optical response of these structures may be expressed using Fresnel complex coefficients. Employment of metamaterials allows one to engineer and program whose optical constants by will. An important consequence here, is that a well-established restriction for period-limited amplitude sensitivity may be surpassed.

It is known that hybrid metal/dielectric systems can be fairly well described by employing the effective medium approximation[33,104,105] (EMA). In fact, by using this approach one designs an effective medium with a complex index of refraction, which could provide a similar optical response to what is observed in the experiments[104]. In this case, the Maxwell-Garnett EMA approximation is typically applied to simulate isolated conductive elements[33,104,105], while the Bruggeman EMA approximation appears to be more efficient when metal elements are electrically connected[106]. EMA is typically applied to structures with the size of features $a \ll \lambda$, but surprisingly it is still valid for plasmonic systems with $a \sim \lambda$[104]. Since the 3D woodpile photonic crystal structure used in this study presents a combination of electrically connected metal-covered nanopile (nanorod) elements, the application of the Bruggeman approximation looks more adequate. Indeed, the tests showed that this approximation could provide a fairly precise description of the optical properties of silver-coated woodpile metamaterial structures. In this case, the effective dielectric constant of the hybrid medium (silver-coated piles with air filled gaps) is approximated by the following Bruggeman equation:

$$f\frac{\varepsilon_{Ag}(\omega)-\varepsilon_{eff}(\omega)}{\varepsilon_{Ag}(\omega)+2\varepsilon_{eff}(\omega)}+(1-f)\frac{\varepsilon_{Air}(\omega)-\varepsilon_{eff}(\omega)}{\varepsilon_{Air}(\omega)+2\varepsilon_{eff}(\omega)}=0 \qquad (4.1)$$

where ε_{Ag}, ε_{Air}, ε_{eff} are the dielectric constants of Ag, air, and the hybrid effective medium, respectively; f is the fraction of silver in the net volume of the structure. Using the General Oscillator model fit for Ag optical constants from experimentally obtained data (a part of

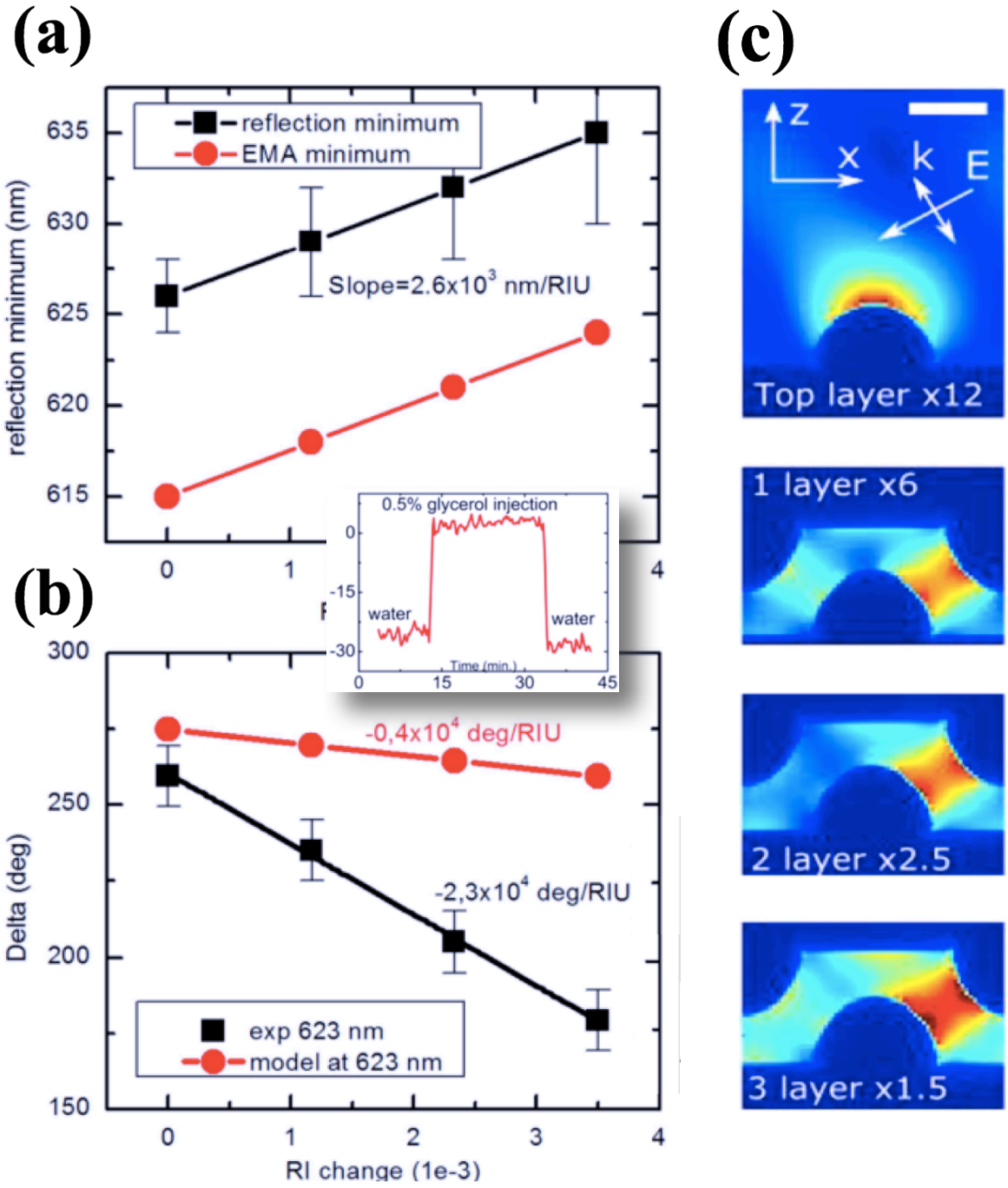

Fig. 4.5 Properties of resonances in 3D woodpile plasmonic crystal and the assessment of sensitivity in biosensing; Calibration curves for spectral (a) and phase (b) responses as a function of refractive index change caused by variation of glycerol concentration. Experimental and theoretical data are represented by black and red lines, respectively. The inset shows a typical shift of phase when 0.5% of glycerol is added to buffer water solution pumped through the metamaterial structure; (c) Electric field distribution inside the metamaterial structure obtained by FDTD simulation.

Woollam CompleteEase software), one could select parameters of the effective medium matching the experimental optical response, in terms of ellipsometric parameters Ψ and Δ. In the tests, this result was achieved by designing a hybrid Ag – dielectric medium with f = 0.1 (10% of Ag in air or water ambience; optical parameters were taken from Palik's book[107]). As shown in Fig. 4.3(a, b), despite some minor deviations of the theoretical curves from the experimental ones out of resonance (especially for water), the Bruggeman EMA approximation demonstrates a very good accuracy in characterizing both the position and the line shape of the resonances, as well as in the description of related phase jumps.

4.4 Sensitivity assessment

In order to estimate the sensitivity of plasmonic modes excited in 3D woodpile structures, a series of model sensing tests were carried out. A well-established glycerine model was used, in which different concentrations of glycerine are added to water in order to provide controllable changes of RI[9,45]. Aqueous solutions of glycerine were pumped through a flow cell by a peristaltic pump and brought into contact with the metamaterial structure. The block containing the metamaterial slide and the flow cell was placed onto the ellipsometer platform and examined. Figure 4.5a shows the response of spectral position of the resonance to variations of RI, obtained from the experiment and theoretical modelling using the Bruggeman EMA model. It can be seen that an increase of refractive index (RI) due to the glycerine addition leads to a shift of the resonance. Here, under a relatively large range of RI variations, the structure demonstrated almost linear dependence of the resonant minimum position on RI change. The spectral sensitivity is estimated to reach 2600 nm/RIU, which is almost one order of magnitude higher than in cases of NHA and LSPR counterparts. It is important that theoretical estimations by EMA model predict the same spectral sensitivity to RI variations, suggesting that the metallized woodpile arrays operate as an effective medium with an appropriate composition of metal (Ag woodpiles) and dielectric (water-filled gaps between woodpiles) constituents. As follows from Fig. 4.5b, the phase also demonstrates a linear dependence to RI changes within this range. In particular, the injection of a very small concentration of glycerol (0.5%) corresponding to a change of RI by 10^{-3} RIU caused a shift of phase by more than 30°, which was far beyond the noise level in the system. Thus, the phase sensitivity was higher in this case than 3×10^4 deg. of phase shift per RIU change, which is slightly lower that values obtained with DCLPR in 2D plasmonic nanodot arrays (>2×10^5 deg. of phase per RIU)[9,45], but comparable or better than relevant values for SPR for gold films[27] or hybrid metal film/graphene architectures[86,92]. Interestingly, modelling using the EMA approximation predicted a 3-fold lower sensitivity compared to the experiment. One may believe that such a discrepancy is explained by imperfections in the EMA approach, as it does not take into account topological phase properties.

Thus, plasmon modes excited over 3D plasmon crystal metamaterials can break the diffraction-related limitation of 2D periodic structures and provide spectral sensitivity of 2 600 nm/RIU, which is comparable with best values for thin film-based SPR in the Kretschmann-Raether prism geometry and outperforms relevant sensitivities of LSPRs and SPPs in alternative nanoscale architectures of nanoparticle (250–500 nm/RIU)[8,47,45,108] and nanohole (300–400 nm/RIU)[31,32] arrays, respectively. It is interesting that a certain increase of spectral sensitivity enhancement was earlier reported for NHA arrays under conditioning of their quasi-3D dimensionality[109,110]. In particular, the sensitivity could be increased up to 700–800 nm/RIU and 1100 nm/RIU under the addition of a second, physically separate level of isolated gold disks at the bottoms of the nanoholes[109], or by using metal-coated substrate-supported quasi-3D-dimentional half-sphere arrays[110], respectively. It is supposed that the photon crystal metamaterial structures, described in this work, present the next step of dimensional scaling toward true 3D nanoarchitectures, enabling the excitation of plasmon modes over the volume of the metamaterial matrix. It is believed that with the help of artificially created metallized woodpiles, an effective medium composed of metal (Ag-coated woodpiles) and dielectric (gaps between the woodpiles) sub-media. The illumination of such structures by light causes the excitation of delocalized plasmon oscillations (electric currents) over electrically connected elements of the medium (metallized woodpile structures), which leads to a drastic loss of effective reflectivity at an appropriate combination of angle of light incidence and the pumping wavelength. Such plasmon mode provides a much-improved response to refractive index variations, as the sensed dielectric environment becomes a part of the artificially formed effective metal-dielectric medium. The situation is in many respects similar to the previous article on plasmon nanorod metamaterials[46]. Here, by using a “forest” of densely packed long (~350–450 nm) gold nanorods, oriented perpendicularly to a glass substrate, a quasi-3D effective medium with metal and dielectric constituents was also created, although the thickness of this layer was much smaller (<450 nm). Plasmonic modes excited over such a “forest” also provided unexpectedly high response to RI variations (up to 30000 nm/RIU), which was in accordance with EMA-based estimations. In the plasmon crystal metamaterial case, it is expected a further enhancement of sensitivity above 10 000 nm/RIU with a proper optimization of the 3D plasmonic crystal geometry. In particular, the estimations and preliminary tests show that such a gain of sensitivity can be achieved through the decrease of plasmon crystal unit cell and slight modifications of its architecture. It is important that in contrast to plasmonic nanorod arrays[46] and other nanohole[31,32] or nanoparticle[8,47,45,108] structures plasmon modes excited in 3D photonic crystal structures can combine high spectral sensitivity and extremely promising characteristics of light phase conditioned by extreme darkness of the observed resonances. Indeed, the light darkness in resonances provided prominent phase singularities, yielding the sensitivity of more than 3×10^4 Deg. of phase per RIU which is enough to enable label-free single molecule detection[9].

One of the key advantages of the proposed metamaterial-based transducer geometry consists in the large area for biomolecule immobilization offered by the 3D matrix. This enables the implementation of new sensing geometries and strategies, not feasible with film-based SPR or 2D LSPR. Indeed, by functionalizing the woodpile blocks and immobilizing a receptor on their surfaces, one can follow the binding of a selective analyte with the receptor inside the woodpile matrix. The considerably increased surface area given by the metamaterial topography significantly increases the amount of biomaterial that can be incorporated into the matrix within the available probe depth, maximizing the "biological" sensitivity of the system. Furthermore, the distance between the woodpile blocks can be selected to match the size of biological species of interest, giving access to a further size selectivity option that is important for many tasks in immunoassays and virus and protein detection. In general, relatively large openings in the woodpile array could contribute to a good transport of biological species, which is not always the case when porous nanomaterials are used as bioimmobilization templates. In addition, a strong field enhancement at some points of the metamaterial matrix makes possible the involvement of a Surface Enhanced Raman Scattering channel, which can be used in parallel with the main optical transduction channel.

4.5 Summary

For the first time excitation of plasmons in 3D plasmonic crystal was studied. It is shown that employment of 3D nanoarchitectures of plasmon excitation can break the diffraction-related limitation of 2D periodic structures and thus obtain a much-improved spectral sensitivity (2600 nm/RIU), as well as a prominent phase response (3×10^4 Deg. of phase per RIU). The sensitivity enhancement was demonstrated using Woodpile-based photonic crystal metamaterials, but it is likely that similar effect can be obtained with alternative 3D architectures (nanorod etc) constituting effective metal/dielectric medium.

Thus, the proposed sensor nanoarchitecture matches earlier stated criteria for desired parameters of future sensor prototypes, namely the combination of ultrahigh point sensitivity (provided by the phase interrogation) and fairly high spectral sensitivity for a wider dynamic range of measurements (provided by the spectral interrogation).

Chapter 5

Nearfield plasmonic enhancement for sensing

CONTENTS

5.1 Introduction

Excitation of diffractively coupled localized surface plasmon resonances over a nanoparticle or nanodot array leads to a drastic localization and concentration of electric field on the nanoparticles, especially in the region between them (*hot spot*). Furthermore, by changing the distance between the nanoparticles and their profile, one can control the "efficiency" of such artificially created hot spots. This phenomenon may be used for enabling SERS channel. The knowledge of electric field distribution induced by plasmonic nanoarchitectures appears to be one of key factors to verify conditions of plasmonic inter-coupling and check the functionality of plasmonic nanodevices. However, despite relatively easy numerical modelling of electric field patterns, experimental measurements and mapping of plasmonic fields presents a real challenge. As the diffraction-limited resolution of far field optical methods is not sufficient to resolve nanoscale plasmonic geometries, one has to employ near-field or "indirect" techniques to accomplish the task. Indirect methods typically use field-affected additional parameter to resolve the pattern, including two-photon excitation of gold photoluminescence[111], breakdown melting of nanostructures[112], the use of photosensitive molecules[113], electron energy loss Transmission Electron Microscopy[114,115] etc. Each of these techniques has its advantages but none of them offer a proper combination of efficiency, control of incoming light, rapidity, commodity and high resolution.

As an alternative, Scanning Near-field Optical Microscopy techniques are promising for studies of optical near field properties of metallic nanostructures. Aperture SNOM has its resolution limited by the size of the optical aperture. The aperture size also limits the optical signal detection value, which can be a real problem for mapping with a reasonable acquisition time. Apertureless SNOM looks to be a more preferable option[116]. The idea to improve optical resolution by means of synchronous detection of scattering from the tip was first mentioned in 1994. Here, resolutions of about 0.5 um on the surface of compact disk using 3 nm metallic[117] and Si tips[116] were demonstrated. The latter result was later improved down to 10 angstrom resolution of mica slices using 5-nm tip and interferometric detection[76]. Surface-plasmon dephasing times extracted from the near-field spectra of the individual particles in uniform TiO_2 environment were also estimated[118].

Apertureless SNOM can also be used to map near-field properties of metallic nanostructures[119,120]. Some previous experimental studies suggested the use of interferometric background suppression provided by heterodyne or homodyne detection

to improve the signal/noise ratio. Such devices can be extremely sophisticated, while the evaluation of obtained optical near-field imaging results could be rather complicated[121] and provoke wrong interpretation[122].

In this Chapter, an alternative approach for near-field distribution mapping is considered, which does not use of any interferometric system. Here, plasmonic samples are illuminated in inverted configuration, implying the illumination of the sample through a glass and the collection of the signal using the same optical path. The measured optical signal is demodulated at harmonics of the fundamental tip oscillation frequency[121,123]. We show that such configuration enables to extract more precisely information of electric field distribution and intensity, arising from plasmonic nanostructures. It is important that the proposed configuration uses normal light incidence, which enables one to benefit from in-plane polarization control, separating measured signals from mechanical artefacts[124]. It should be noted that a manuscript describing results of this research is currently under preparation.

5.2 Materials and methods

5.2.1 AFM-Raman setup

SNOM device scheme is described in Figure 5.1. We have used an integrated atomic force microscope (NT-MDT) optically coupled to an inverted optical microscope (Olympus IX-71) and Cherny-Turner configuration optical spectrometer (SOL instruments). We used commercial platinum coated AFM tip (NT-MDT HA_NC/Pt) as nanoscale transducer. The He-Ne laser (632.8 nm) beam, passed through a half-lambda plate (thus allowing changing excitation polarization) and was focused on the sample with the tip in intermittent-contact mode via an oil-immersion objective (Olympus, 100x, 1.3NA). Backscattered light was collected by the same objective and detected by PMT (Hamamatsu) for SNOM measurements via fourth-harmonic Lock-in demodulation of tip oscillation. This method represents reasonable signal-to-noise ratio and almost complete background signal damping. For SERS measurements, the AFM tip was retracted from the laser spot (attenuated down to 0.01 mW to avoid fluorophore photobleaching) and backscattered light spectrum was analysed by the confocal Raman spectrometer (NT-MDT SPECTRA OMU52, cooled low noise CCD Andor detector).

5.2.2 Optical path adjustment

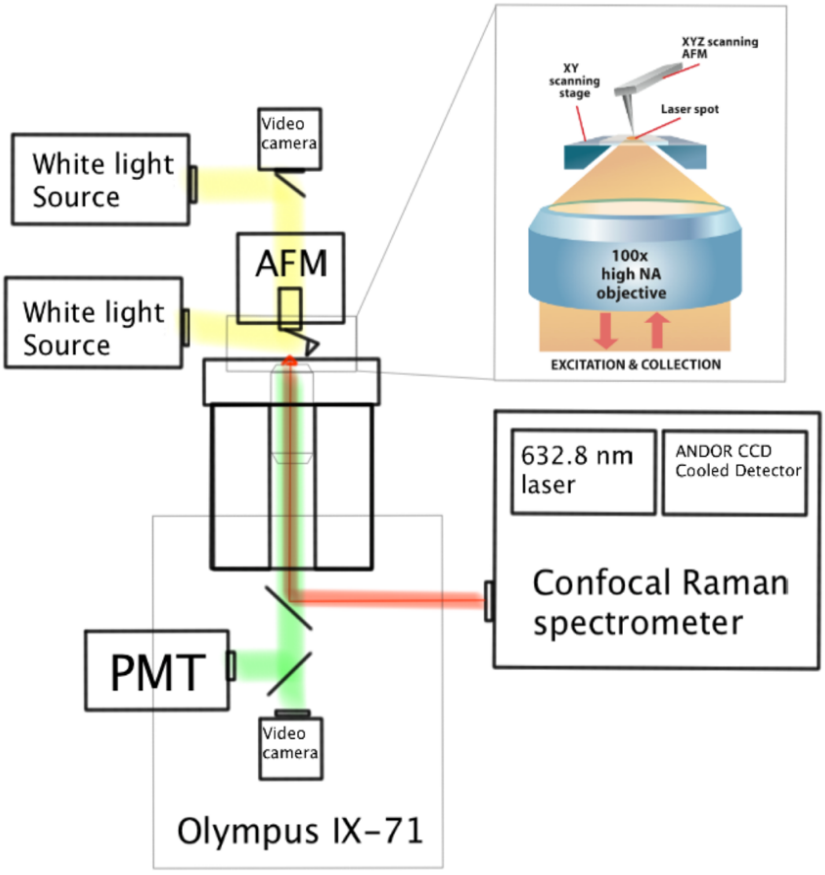

Fig. 5.1 aSNOM experimental setup. Sample is installed in the AFM and may be localized independently from incident light optical path and AFM tip position. Laser beam reflects from a mirror under the sample and is focus with high NA objective into a half-wavelength focal spot. On one part, scattered Raman light is collected through the same optical system and is driven to monochromator of the spectrometer. Dispersed beam is analysed by CCD cooled sensor. On the other part, same light is collected by PMT for aSNOM purposes.

In order to perform measurements, a precise system calibration is required. First, a 90% mirror is applied to reflect 10% of the beam collected from the sample and direct it to the PMT. Then, tip is scanned over a plane sample area and a fixed optical path. The resulted image will have a contrast, corresponding to the location of the tip apex. Having combined the objective focal spot with tip apex, one can independently change the position of the sample, using raster scanning in order to perform near-field aSNOM imaging. PMT amplification should be adjusted so that an empty sample area would have a zero signal value. For Raman measurement, a 100% mirror is applied, reflecting all coming light from the sample into the spectrometer. In this case, the tip is eliminated from the focal spot to avoid parasitic effects.

5.2.3 Sample fabrication

Au colloid films on glass slides were prepared by modification of the glass surface with a (3-aminopropyl)triethoxysilane (APTES). Cover glass 20 × 20 mm and 0.13-0.17 mm thick were rinsed with acetone, dried in nitrogen and treated with Piranha solution for 40 min at 60°C. The slides were then rinsed by water, dried and placed in 20% APTES (Sigma-Aldrich) solution in ethanol for 20 min. The modified glass slides were thoroughly rinsed with ethanol to remove non-reacted APTES, dried and incubated in 60-nm gold nanoparticles colloidal solution (Sigma-Aldrich) overnight. Gold-covered glass slides were rinsed with water and dried at 60°C for 1 hour. Rinsing with water and ethanol did not affect the gold film.

5.3 Near-field detection of nanoparticle assembles LSPR

aSNOM signal critically depends on scatterer parameters. Certain requirements are applied to the shape and material of the tip. As an example, Pt-covered tip was used in many experiments. Standard Si tip may have a smaller apex diameter and potentially better resolution, but light reflection from metals is significantly larger[1], which is a crucial factor for low intensity near-field scattering. Gold could be an obvious choice, as Au-coated tips are mass-produced and easily available on the market. However, tip-particle plasmonic interaction should be avoided in our experiment, as it can affect the final result. Ideally, the AFM tip should only scatter near-field and not modify it. Another important factor is a shape of apex. Traditional commercially available probes are made of crystal Si and tip apex shape represents a 4-slope pyramid (Fig. 5.2a). Moreover, AFM operation implies an additional tip inclination of about 20-30°. As a result, data obtained using a classic tip are typically highly inhomogeneous. For topography measurements, simple tip deconvolution may improve the quality of obtained data. However, in case of near-field imaging, intensity-distance dependence is non-linear and a correct interpretation of results becomes an extremely complicated task. Nevertheless, the employment of amorphous Si tip formed by e-beam sharpening (Fig. 5.2b) can solve the problem of tip symmetry and thus guarantee negligible tip parameters variation.

Detected aSNOM signal represents a mixture of background illumination and a scattered near-field part. Light intensity, enhanced by localized plasmon resonance and scattered from the tip varies while increasing the distance between the near-field source and the scatterer. Near-field component may be extracted by high order demodulation of detected optical signal. Determination of utilized harmonic is a trade-off between background suppression and reasonable signal-to-noise ratio for extracted near-field information[1,125]. Figure 5.2 represents experimentally measured near-field distributions

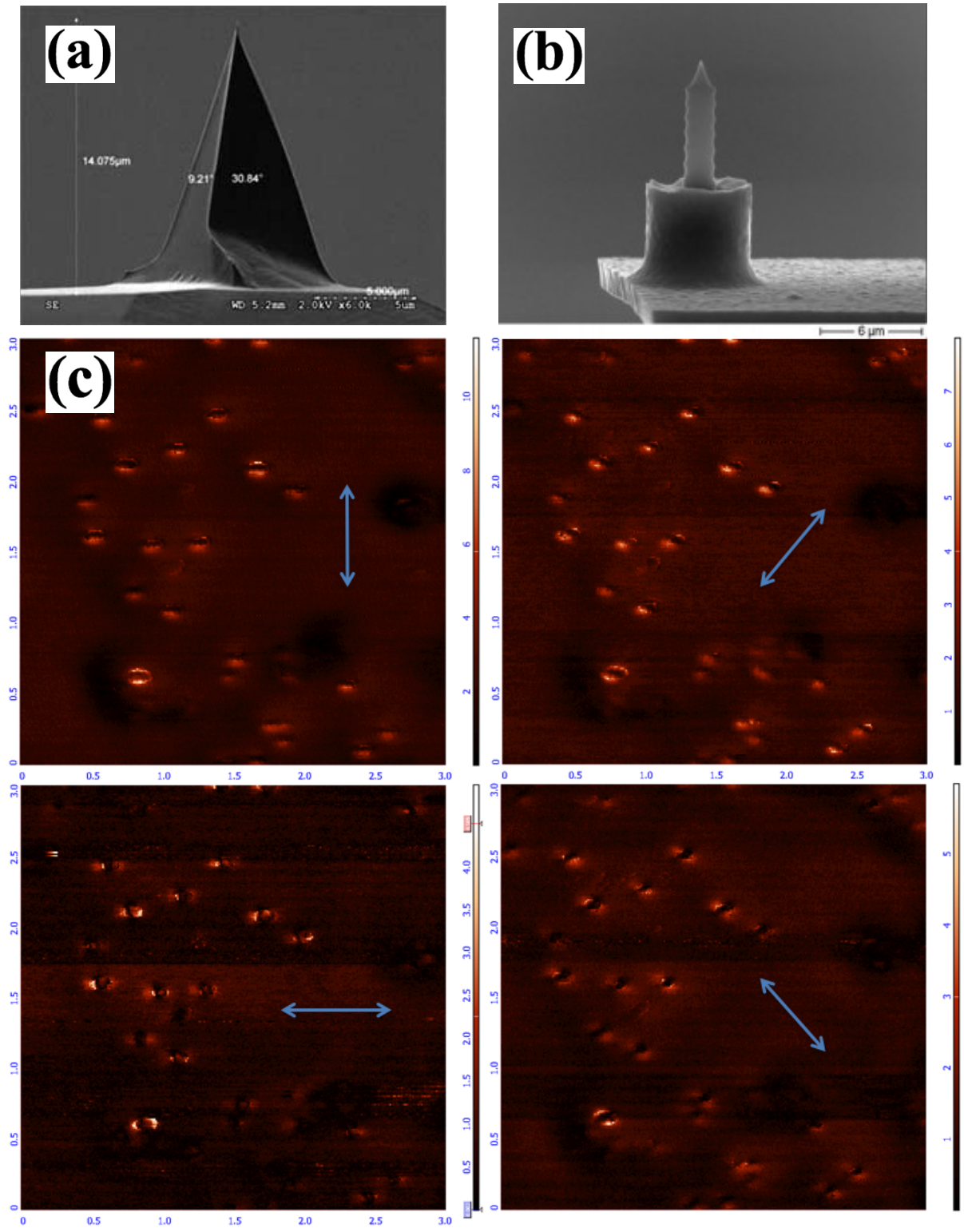

Fig. 5.2 (a) SEM image of classic well-established Si cantilever. Tip apex represents 4-slope pyramid; (b) Symmetrical e-beam shaped tip provides a uniform aSNOM measurements; (c) Example of aSNOM homogenous near-field distribution imaging, related only to the polarization of incident light and not affected by the tip apex irregular shape. Blue arrow corresponds to incident light polarization direction.

on the same sample area. Here, one can see a very bright and low-noise evanescent field patterns arising around spherical golden nanoparticles along the incident polarization directions. Since nearfield distribution uniformly changes with the 90-deg. polarization switch, it cannot be due to any artifact such as tip apex-related features. We believe that such in-plane polarization-sensitive configuration is a great advantage of inverted experimental setup, compared to alternative[126] side illumination geometries, where sample is illuminated from the side and the latter case does not have system versatility and lacks precise control of incoming polarization. 632.8 nm HeNe gas laser was used in order to excite plasmon resonance in gold nanoparticles. Knowing, that obtained data is mainly due to plasmonic resonance properties of Au nanoparticles, near-field imaging of any arbitrary nanoparticle orientation may now be measured.

5.4 Correlation between near-field imaging and Raman

Classic SERS substrate relies on electric field amplification power of single nano-sized plasmonic structures. The use of coupled nanoparticle system increases amplification possibilities of SERS. When a coherent monochromatic laser electromagnetic wave meets a pair of two closely located metallic nanoparticles (*duplet* or *dimer)*, free electron cloud of the particle start to react and oscillate in a direction of wave polarization. Depending on dimer spatial orientation and polarization of the incident wave, the induced dipoles can start to interact. Numerical simulations have clearly evidenced that if the polarization of the incoming electromagnetic field is along the dimer axis the field in the gap can be enhanced by several orders of magnitude[127]. Such configuration is called “hot spot”. It is widely accepted that Raman scattering intensity scales roughly with forth power of electric field[128]:

$$I_{SERS} \propto E^4 \tag{5.1}$$

A rigorous self-consistent formulation is required to describe origins of Raman scattering enhancement. SERS signal strongly depends on several parameters: the electromagnetic enhancement of plasmonic nanoobject and the number, distribution and orientation of probed molecules. The latter factor is known as chemical enhancement, which results from direct contact of the molecule with the metal surface, modifying effective polarizability of the system[129,130]. Relative contribution of SERS enhancement factors provoked many debates in the SERS community. There were some attempts for mass quantification of Raman signal[68,131,132], but these results are disputable. In cases of single-molecular approach[68,133] and high-concentrations studies[134] it was statistically demonstrated that only a small number of hot spots efficiently contribute to the overall SERS signal. For both these cases, calculations relied on numerical estimations of near-field intensities in hot spots were applied. To the best of my knowledge, these statistical

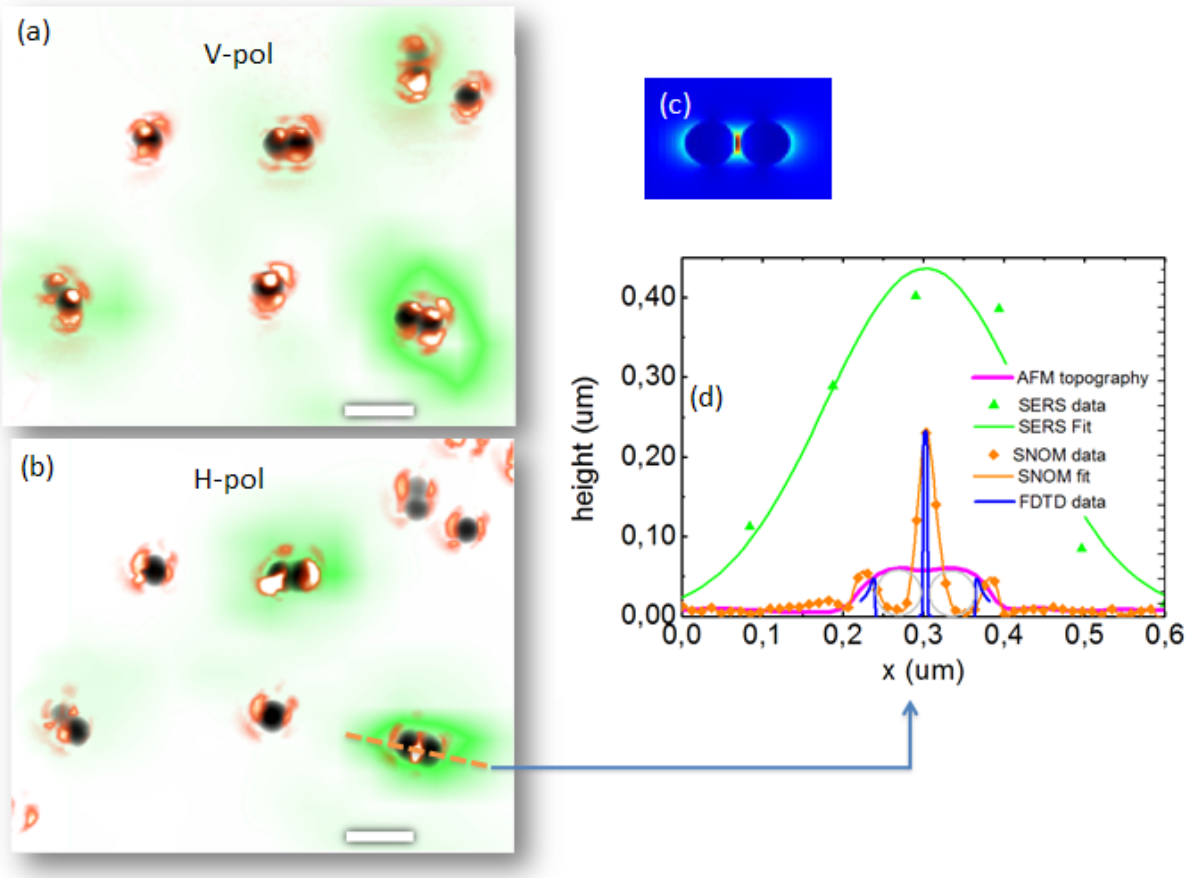

Fig. 5.3 (a) Combined AFM (in black), SERS intensity (in green) and SNOM intensity (in red) images for a vertical excitation polarization; (b) Combined AFM (in black), SERS intensity (in green) and SNOM intensity (in red) images for a horizontal excitation polarization; (c) FDTD calculation of the distribution of the electric field for two optically coupled gold nanoparticles (excitation: 632.8 nm, polarization along the dimer axis) (d) Different profiles of two dimers: topography (in purple), SERS intensity (in green), SNOM intensity (in orange) and calculated electric field intensity (in blue).

studies we never compared with experimental near-field measurements in individual hot spots. We believe that such lack of the comparative analysis can lead to strong misinterpretation of real SERS efficiency. As an example, enhanced Raman signal can come from dimmed 'cold' spots with extensive number of molecules and not from high-efficient hotspots with small amount of molecules[134]. To have a more quantitative idea about the contribution of each hot spot to the SERS signal, a sub-diffraction analytical tool is required.

Figure 5.3 shows a combined AFM+SNOM+SERS mapping of randomly distributed Au nanoparticles. Here, one can see several hotspots, based on a combination of two closely located nanoparticles. A cross-section (Fig. 5.3d) of nanoparticle dimer demonstrates enhancement of both Raman and near-field signals in case of the excitation light polarization oriented along the dimer. By AFM we determine the precise configuration (size of the nanoparticles, distance between them) of each hotspot. This

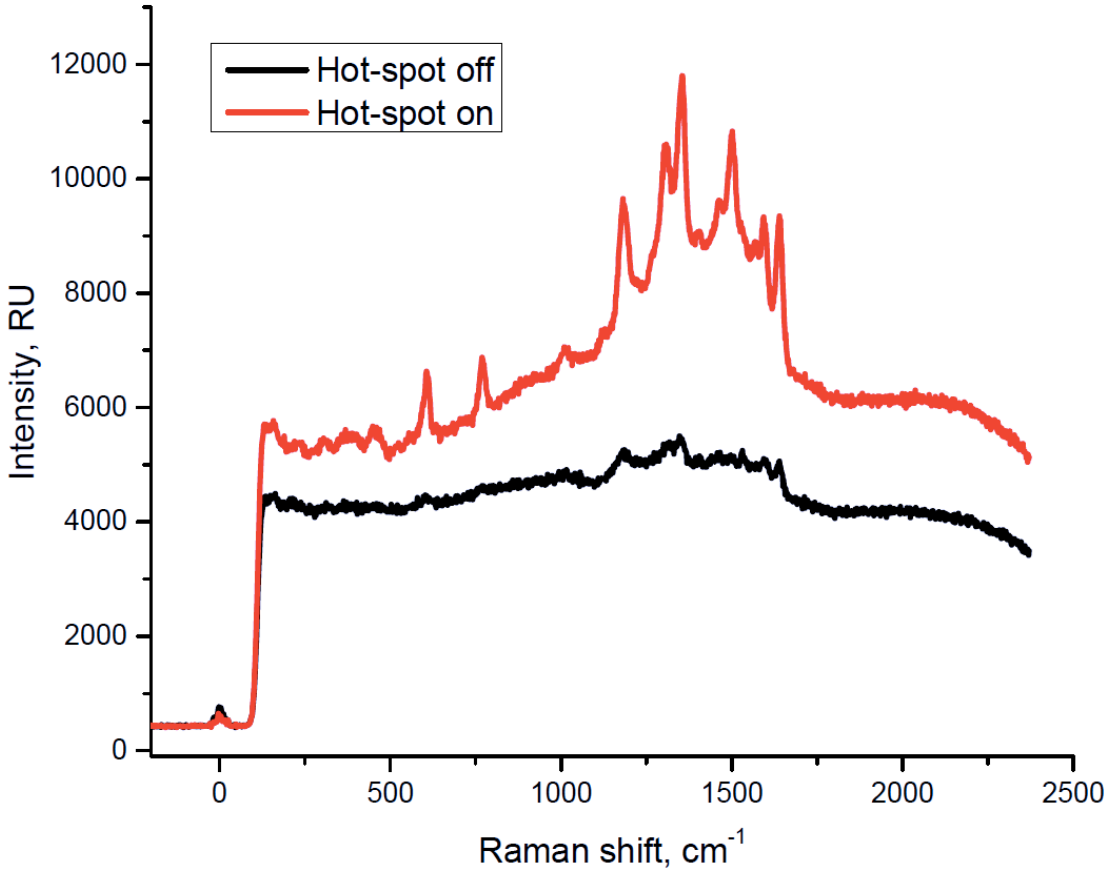

Fig. 5.4 Hot-spot Raman intensity enhancement. A red curve demonstrates enhanced Raman scattering from incident light oriented along the dimer orientation. A black curve illustrates perpendicular light polarization with respect to the dimer (hot-spot off). Measurements performed in R6G solution in order to integrate all biomolecular orientations and their spatial distributions. Exposition time 30s. 632.8nm HeNe gas laser with intensity 1mV, measured on the sample was used to excite Raman scattering.

information is used in FDTD modelling. The SNOM image clearly demonstrates a strongly enhanced electromagnetic field between the nanoparticles in accordance with the polarization of the incoming light. Raman signal intensity is represented in Figure 5.3 by green colour. It is visible that areas of Raman signal generation are localized closely to the nanoparticle positions. However, the level of Raman scattering is different, which is probably related to non-uninform dye distribution among the nanoparticles. It should be noted that a larger area of Raman mapping, compared to corresponding aSNOM and AFM data is caused by diffraction-limited resolution of optical spectrometer and thus, a relatively large Raman signal areas around the nanoparticle assemblies related entirely to the SERS signal from the molecules, which absorbed on the surface of nanoparticles.

Let us identify “hot spot off” as an arrangement of dimer with sample material when polarization of applied light is oriented perpendicularly to the dimer axis and a “hot spot on” when both have the same direction. FDTD calculations clearly demonstrate that the electromagnetic enhancement is much higher for a hot-spot on. This is exactly what we experimentally observed: both SERS and SNOM signals are much higher for a “hot spot

on" compared to the same "*off*" state. The accordance between FDTD simulations, SNOM measurements and SERS intensity is very good as can be seen in the profile of a hotspot on visualized in Figure 5.3.

It should be noted that the final SERS intensity strongly depends on the hot spot parameters. Indeed, two almost identical dimers (same distance between the nanoparticles and their profiles) can provide quite a different SERS intensity. This feature is related to the number of R6G molecules giving rise to the SERS signal and biomolecules distribution over a dimer. In order to get rid of this unknown distribution, one can simplify the task by putting sensor into solution with biomaterial – which is a standard approach for plasmonic biosensors. Thus, all molecular orientations and spatial position will be averaged in time and resulted data may be presented by histogram of Raman intensities versus number of detected single events of Raman enhancement. The largest detected Raman value would most probably correspond to the "hottest" near-field enhancement inside the hot-spot.

Fig. 5.4 shows averaged Raman data from a hot spot, placed in R6G-water solution. Despite the fact, that presence of uncoupled golden nanoparticles itself typically[1,130,132,135] amplifies detected Raman scattering by 10^6 (comparing to pure Raman with no presence of any enhancing structures), a "hot spot on" arrangement additionally amplifies R6G peaks for 1-2 orders of magnitude (peak over background value).

5.5 Summary

We developed an apertureless SNOM methodology for polarization-sensitive imaging of electric near-fields, induced by plasmonic nanoantennas. This result was achieved by a modification of aSNOM setup, which consisted in the application of inverted geometry of sample illumination and collection beams combined with a technique of a signal demodulation at high harmonic of tip modulation frequency (system is based on commercial NT-MDT system). By using newly developed aSNOM methodology together with Raman spectroscopy and AFM topography mapping, we demonstrated the visualisation of randomly distributed hot-spots, formed by Au NP dimers as well as the distribution of electric near-field and SERS signal from R6G dye. Our data illustrate a good correlation between Raman signal intensity and the near-field intensity of the hot spot. Based on this idea a direct pure experimental method is proposed to localize position and estimated "efficiency" of SERS hot spot. Raman scattering improvement is especially important in combination with PSLR sensors, as double-dot configurations has benefits of plasmon resonance spectral position tuning along with size-based biomaterial selectivity.

Conclusion

Recent developments in nanotechnology and metamaterial engineering opened access to a dramatic improvement of sensitivity of optical biosensors and their novel functionalities. Conventional plasmon biosensor, also referred to as Surface Plasmon Resonance biosensor, employs the excitation of surface plasmon polaritons in Kretschmann-Raether geometry. This approach provides very good sensitivity, but it does not match to many of modern trends in biosensing, including compatibility with hybrid bio-nanoarchitectures, size-based selectivity, spectral tunability, extremely strong localization of electric field beyond the diffraction limit, nanotweezing etc. In was recently shown that the employment of plasmonic metamaterials for biosensing can to drastically advance current state-of-the-art plasmonic biosensors.

This thesis considers novel promising metamaterials for biosensing and their assessment in sensing tasks. First metamaterial presents a periodic array of glass supported Au nanoparticles, which can provide diffractively coupled surface lattice resonances. For the first time conditions of excitation and properties of diffractively coupled plasmonic surface lattice resonances over 2D metamaterial array of single and double nanoparticles in direct and ATR geometries were studied in detail. Here, medium-related $PSLR_{air}$/$PSLR_{wat}$ and substrate-related $PSLR_{sub}$ plasmonic modes, corresponding to the coupling of individual plasmon oscillations at medium- and substrate-related diffraction cut-off edges, were identified. It was shown that PSLR excited both in direct and ATR geometries can have extremely small width (down to a few nm FWHM). Sensitivities of these modes to variations of refractive index of adjacent sample dielectric medium were assessed. It was found that the spectral sensitivity of medium-related PSLRs (300-400 nm/RIU) is conditioned by nanostructure periodicity, while the substrate-related modes showed much lower sensitivity. It was also shown that PSLRs can provide a very low intensity (down to 10^{-6} Deg.) in the resonance conditions (*light darkness*), leading to the generation of extremely sharp jump of phase of light in the very minimum of the resonance. The employment of this jump can give rise to very high phase sensitivity. Sensitivities of PSLR and SPR in the Kretschmann-Raether geometry were directly compared. It was shown that despite much lower spectral sensitivity (400 nm/RIU compared to 3600 nm/RIU), PSLR can exhibit much higher phase sensitivity (>10^5 Deg./RIU compared to ~10^4 Deg./RIU). To the best of my knowledge, PSLRs outperform all plasmonic counterparts in terms of phase sensitivity. The feasibility of PSLR for biosensing was demonstrated using standard streptavidin-biotin affinity model. Combining advantages of nanoscale architectures, including drastic concentration of electric field, possibility for manipulations at the nanoscale and high phase and spectral sensitivities, PSLR promise the advancement of current state-of-the-art plasmonic biosensing technology toward single molecule label-free detection.

Second, for the first time excitation of plasmons in 3D plasmonic crystal was studied. It is shown that employment of 3D nanoarchitectures of plasmon excitation can

break the diffraction-related limitation of 2D periodic structures and thus obtain a much-improved spectral sensitivity (2600 nm/RIU), as well as a prominent phase response (3 $\times$ 10^4 Deg. of phase per RIU). The sensitivity enhancement was demonstrated using Woodpile-based photonic crystal metamaterials, but it is likely that similar effect can be obtained with alternative 3D architectures constituting effective metal/dielectric medium. The proposed 3D sensor nanoarchitecture matches earlier stated criteria for desired parameters of future sensor prototypes and offers unique combination of ultrahigh point sensitivity (provided by the phase interrogation) and fairly high spectral sensitivity for a wider dynamic range of measurements (provided by the spectral interrogation). It is also important that the porous matrix of the woodpile structure can be used to match the size of biological species of interest, giving access to a further size-selectivity option, which is important for many tasks of immunoassays and protein detection.

Finally, an apertureless SNOM methodology for polarization-sensitive imaging of electric near-field, induced by plasmonic nanoantennas has been developed. This result was achieved by a modification of aSNOM setup, which consisted in the application of inverted geometry of sample illumination and collection beams combined with a technique of a signal demodulation at high harmonic of tip modulation frequency (system is based on commercial NT-MDT system). By using newly developed aSNOM methodology together with Raman spectroscopy and AFM topography mapping, we demonstrated the visualisation of randomly distributed hot-spots, formed by Au NP dimers as well as the distribution of electric near-field and SERS signal from R6G dye. Our data illustrate a good correlation between Raman signal intensity and the near-field intensity of the hot spot. Based on this idea a direct pure experimental method is proposed to localize position and estimated “efficiency” of SERS hot spot. Raman scattering improvement is especially important in combination with PSLR sensors, as double-dot configurations has benefits of plasmon resonance spectral position tuning along with size-based biomaterial selectivity.

An important consequence of this research, one can see in generalization of plasmonic phenomena for different geometries and conditions. Employment of metamaterials allows one to engineer programmable optical constants of matter and a controlled macroscopic optical response, provided by complex Fresnel coefficients. Next steps will be conducted to investigate new plasmonic metamaterials, which possesses unique optical properties, enabling to create diffraction-related complete *optical darkness*. Preliminary results showed abnormally high spectral sensitivities along with state-of-the-art phase sensitivity values, which outperform most known examples of well-established plasmonic sensors.

List of publications

[Th-1] *Artem Danilov, Gleb Tselikov, Fan Wu, Vasyl G. Kravets, Igor Ozerov, Frederic Bedu, Alexander N. Grigorenko, Andrei V. Kabashin.*
«Ultra-narrow plasmonics surface lattice resonances for biosensing applications»
Journal of Biosensors and Biolectronics, 2017.
DOI: 10.1016/j.bios.2017.12.001

[Th-2] *Andrey I. Aristov, Maria Manousidaki, Artem Danilov, Konstantina Terzaki, Costas Fotakis, Maria Farsari & Andrei V. Kabashin.*
3D plasmonic crystal metamaterials for ultra-sensitive biosensing.
Scientific Reports / Nature Publishing Group, 2016.
DOI: 10.1038/srep25380

[Th-3] *Artem Danilov, Gleb Tselikov, Fan Wu, Vasyl G. Kravets, Igor Ozerov, Frederic Bedu, Alexander N. Grigorenko, Andrei V. Kabashin.*
«Condition of excitation and sensitivity of diffractively-coupled surface lattice resonances over plasmonic nanoparticle arrays in ATR geometry»
Proc. SPIE 10521, Synthesis and Photonics of Nanoscale Materials XV, 1052109, 2018.
DOI: 10.1117/12.2295192

[Th-4] *Artem Danilov, Andrey I. Aristov, Maria Manousidaki, Konstantina Terzaki, Costas Fotakis, Maria Farsari & Andrei V. Kabashin.*
«Phase singularities in 3D plasmonic crystal metamaterials for ultrasensitive Biosensing»
Proc. SPIE 10093, Synthesis and Photonics of Nanoscale Materials XIV, 100930G, 2017.
DOI: 10.1117/12.2253024

[Th-5] *Artem Danilov, Andrey I. Aristov, Maria Manousidaki, Konstantina Terzaki, Costas Fotakis, Maria Farsari & Andrei V. Kabashin.*
«3D plasmonic metamaterials for enhanced spectral sensitivity ofoptical nanosensors»
Proc. SPIE 10080, Plasmonics in Biology and Medicine XIV, 100800C, 2017.
DOI:10.1117/12.2252918

[Th-6] *Artem Danilov, Vasyl G. Kravets, Gleb Tselikov, Alexander N. Grigorenko, Andrei V. Kabashin*.
«Phase-sensitive plasmonics biosensors: from bulk to nanoscalearchitechtures and novel functionalities»
Proc. SPIE 9737, Synthesis and Photonics of Nanoscale Materials XIII, 97370D, 2016.
DOI:10.1117/12.2214883

Bibliography

1. Novotny, L. & Hecht, B. *Principles of Nano-Optics*. (Cambridge University Press, 2006). doi:10.1017/CBO9780511813535

2. Liu, Y. & Zhang, X. Metamaterials: a new frontier of science and technology. *Chem. Soc. Rev.* **40,** 2494 (2011).

3. Maier, S. A. *Plasmonics: Fundamentals and Applications*. *Physics* (Springer, 2007). doi:10.1007/0-387-37825-1

4. West, P. R. *et al.* Searching for better plasmonic materials. *Laser Photonics Rev.* **4,** 795–808 (2010).

5. Ritchie, R. H., Arakawa, E. T., Cowan, J. J. & Hamm, R. N. Surface-plasmon resonance effect in grating diffraction. *Phys. Rev. Lett.* **21,** 1530–1533 (1968).

6. Kelly, K. L., Coronado, E., Zhao, L. L. & Schatz, G. C. The optical properties of metal nanoparticles: The influence of size, shape, and dielectric environment. *J. Phys. Chem. B* **107,** 668–677 (2003).

7. Kreibig, U. & Vollmer, M. Optical Properties of Metal Clusters. *J. Am. Chem. Soc.* **118,** 6098–6098 (1995).

8. Kravets, V. G., Schedin, F. & Grigorenko, A. N. Extremely narrow plasmon resonances based on diffraction coupling of localized plasmons in arrays of metallic nanoparticles. *Phys. Rev. Lett.* **101,** 1–4 (2008).

9. Kravets, V. G. *et al.* Singular phase nano-optics in plasmonic metamaterials for label-free single-molecule detection. *Nat. Mater.* **12,** 304–309 (2013).

10. Pendry, J. B. Negative refraction makes a perfect lens. *Phys. Rev. Lett.* **85,** 3966–3969 (2000).

11. Sakellari, I. *et al.* 3D Chiral Plasmonic Metamaterials Fabricated by Direct Laser Writing : The Twisted Omega Particle. **1700200,** 1–6 (2017).

12. Sakellari, I. *et al.* Direct laser writing of photonic nanostructures. **7392,** 1–9 (2009).

13. Prasad, P. N. *Introduction to Nanomedicine and Nanobioengineering*. (A JOHN WILEY & SONS, INC., 2012).

14. Wood, R. W. XLII. *On a remarkable case of uneven distribution of light in a diffraction grating spectrum*. *Philos. Mag. Ser. 6* **4,** 396–402 (1902).

15. Zenneck, J. Uber die Fortpflanzung ebener elektromagnetischer Wellen laengs einer ebenen Leiterflaeche und ihre Beziehung zur drahtlosen Telegraphie. *Ann. Phys.* **328,** 846–866 (1907).

16. Otto, A. Excitation of nonradiative surface plasma waves in silver by the method of frustrated total reflection. *Zeitschrift fur Phys.* **216,** 398–410 (1968).

17. Kretschmann, E. & Raether, H. Radiative Decay of Non Radiative Surface Plasmons Excited by Light. *Zeitschrift fur Naturforsch. - Sect. A J. Phys. Sci.* **23,** 2135–2136 (1968).

18. Homola, J. *Surface Plasmon Resonance Based Sensors*. *Springer Series on Chemical Sensors and Biosensors* **4,** (2006).

19. Gordon, J. G. & Ernst, S. Surface plasmons as a probe of the electrochemical interface. *Surf. Sci.* **101,** 499–506 (1980).

20. Liedberg, B., Nylander, C. & Lunström, I. Surface plasmon resonance for gas detection and biosensing. *Sensors and Actuators* **4,** 299–304 (1983).

21. Liedberg, B., Nylander, C. & Lundström, I. Biosensing with surface plasmon resonance - how it all started. *Biosens. Bioelectron.* **10,** (1995).

22. Melendez, J. *et al.* A commercial solution for surface plasmon sensing. *Sensors Actuators B Chem.* **35,** 212–216 (1996).

23. Huang, Y. H., Ho, H. P., Kong, S. K. & Kabashin, A. V. Phase-sensitive surface plasmon resonance biosensors: Methodology, instrumentation and applications. *Ann. Phys.* **524,** 637–662 (2012).

24. Haes, A. J. & Van Duyne, R. P. A nanoscale optical biosensor: sensitivity and selectivity of an approach based on the localized surface plasmon resonance spectroscopy of triangular silver nanoparticles. *J. Am. Chem. Soc.* **124,** 10596–10604 (2002).

25. Anker, J. N. *et al.* Biosensing with plasmonic nanosensors. *Nat. Mater.* **7,** 442–453 (2008).

26. Agranovich, V. M. & Mills, D. L. *Surface Polaritons: Electromagnetic Waves at Surfaces*.

27. Huang, Y. H., Ho, H. P., Kong, S. K. & Kabashin, A. V. Phase-sensitive surface plasmon resonance biosensors: Methodology, instrumentation and applications. *Ann. Phys.* **524,** 637–662 (2012).

28. Tudos, A. J. & Schasfoort, R. B. M. *Handbook of Surface Plasmon Resonance*. (2008).

29. Barnes, W. L., Murray, W. A., Dintinger, J., Devaux, E. & Ebbesen, T. W. Surface Plasmon Polaritons and Their Role in the Enhanced Transmission of Light Through Periodic Arrays of Subwavelength Holes in a Metal Film. *Phys. Rev. Lett.* **92,** 1–4 (2004).

30. Ghaemi, H. F., Thio, T., Grupp, D. E., Ebbesen, T. W. & Lezec, H. J. Surface plasmons enhance optical transmission through subwavelength holes. *Phys. Rev. B* **58,** 6779–6782 (1998).

31. Brolo, A. G., Gordon, R., Leathem, B. & Kavanagh, K. L. Surface plasmon sensor based on the enhanced light transmission through arrays of nanoholes in gold films. *Langmuir* **20,** 4813–4815 (2004).

32. Im, H. *et al.* Template-stripped smooth Ag nanohole arrays with silica shells for surface plasmon resonance biosensing. *ACS Nano* **5,** 6244–6253 (2011).

33. Garcia-Vidal, F. J., Martin-Moreno, L., Ebbesen, T. W. & Kuipers, L. Light passing through subwavelength apertures. *Rev. Mod. Phys.* **82,** 729–787 (2010).

34. De Abajo, F. J. G. Colloquium: Light scattering by particle and hole arrays. *Rev. Mod. Phys.* **79,** 1267–1290 (2007).

35. Schuck, P. Use of surface plasmon resonance to probe the equilibrium and dynamic aspects of interactions between biological macromolecules. *Annu. Rev. Biophys. Biomol. Struct.* **26,** 541–566 (1997).

36. Cooper, M. A. Optical biosensors in drug discovery. *Nat. Rev. Drug Discov.* **1,** 515–528 (2002).

37. Karlsson, R. SPR for molecular interaction analysis: A review of emerging application areas. *J. Mol. Recognit.* **17,** 151–161 (2004).

38. Born, M. *et al. Principles of Optics*. (Cambridge University Press, 1999). doi:10.1017/CBO9781139644181

39. Kabashin, A. V & Nikitin, P. I. Interferometer based on a surface-plasmon resonance for sensor applications. *Quantum Electron.* **27,** 653–654 (1997).

40. Kabashin, A. V., Kochergin, V. E., Beloglazov, A. A. & Nikitin, P. I. Phase-polarization contrast for surface plasmon resonance biosensors. *Biosens. Bioelectron.* **13,** 1263–1269 (1998).

41. Grigorenko, a N., Nikitin, P. I. & Kabashin, a V. Phase jumps and interferometric surface plasmon resonance imaging. *Appl. Phys. Lett.* **75,** 3917–3919 (1999).

42. Kabashin, A. V, Patskovsky, S. & Grigorenko, A. N. Phase and amplitude sensitivities in surface plasmon resonance bio and chemical sensing. **17,** 151–161 (2009).

43. Danilov, A., Kravets, V. G., Tselikov, G., Grigorenko, A. V. & Kabashin, A. V. Phase-sensitive plasmonics biosensors: from bulk to nanoscale architechtures and novel functionalities. in (eds. Kabashin, A. V., Geohegan, D. B. & Dubowski, J. J.) **9737,** 97370D (2016).

44. Kabashin, A. V., Kochergin, V. E. & Nikitin, P. I. Surface plasmon resonance bio- and chemical sensors with phase-polarization contrast. *Sensors Actuators, B Chem.* **54,** 51–56 (1999).

45. Kravets, V. G., Schedin, F., Kabashin, A. V & Grigorenko, A. N. Sensitivity of collective plasmon modes of gold nanoresonators to local environment. *Opt. Lett.* **35,** 956–958 (2010).

46. Kabashin, A. V *et al.* Plasmonic nanorod metamaterials for biosensing. *Nat. Mater.* **8,** 867–871 (2009).

47. Duval Malinsky, M., Kelly, K. L., Schatz, G. C. & Van Duyne, R. P. Nanosphere Lithography: Effect of Substrate on the Localized Surface Plasmon Resonance

Spectrum of Silver Nanoparticles. *J. Phys. Chem. B* **105,** 2343–2350 (2001).

48. Kawata, S., Inouye, Y. & Verma, P. Plasmonics for near-field nano-imaging and superlensing. *Nat. Photonics* **3,** 388–394 (2009).

49. Barnes, W. L., Dereux, A. & Ebbesen, T. W. Surface plasmon subwavelength optics. *Nature* **424,** 824–830 (2003).

50. Lal, S., Link, S. & Halas, N. J. Nano-optics from sensing to waveguiding. *Nat. Photonics* **1,** 641–648 (2007).

51. Shalaev, V. M. Optical negative-index metamaterials. *Nat. Photonics* **1,** 41–48 (2007).

52. Yao, J. *et al.* Optical Negative Refraction in Bulk Metamaterials of Nanowires. *Science (80-.).* **321,** 930–930 (2008).

53. Grigorenko, a. N., Roberts, N. W., Dickinson, M. R. & Zhang, Y. Nanometric optical tweezers based on nanostructured substrates. *Nat. Photonics* **2,** 365–370 (2008).

54. Sreekanth, K. V. *et al.* Extreme sensitivity biosensing platform based on hyperbolic metamaterials. *Nat. Mater.* **15,** 621–627 (2016).

55. Laor, U. & Schatz, G. C. The role of surface roughness in surface enhanced raman spectroscopy (SERS): the importance of multiple plasmon resonances. *Chem. Phys. Lett.* **82,** 566–570 (1981).

56. Meier, M., Wokaun, a. & Liao, P. F. Enhanced fields on rough surfaces: dipolar interactions among particles of sizes exceeding the Rayleigh limit. *J. Opt. Soc. Am. B* **2,** 931 (1985).

57. Carron, K. T., Fluhr, W., Meier, M., Wokaun, a. & Lehmann, H. W. Resonances of two-dimensional particle gratings in surface-enhanced Raman scattering. *J. Opt. Soc. Am. B* **3,** 430 (1986).

58. Purcell, E. M. & Pennypacker, C. R. Scattering and Absorption of Light by Nonspherical Dielectric Grains. *Astrophys. J.* **186,** 705 (1973).

59. DeVoe, H. Optical Properties of Molecular Aggregates. I. Classical Model of Electronic Absorption and Refraction. *J. Chem. Phys.* **41,** 393–400 (1964).

60. DeVoe, H. Optical Properties of Molecular Aggregates. II. Classical Theory of the Refraction, Absorption, and Optical Activity of Solutions and Crystals. *J. Chem. Phys.* **43,** 3199–3208 (1965).

61. Zou, S., Janel, N. & Schatz, G. C. Silver nanoparticle array structures that produce remarkably narrow plasmon lineshapes. *J. Chem. Phys.* **120,** 10871–10875 (2004).

62. Markel, V. A. Divergence of dipole sums and the nature of non-Lorentzian exponentially narrow resonances in one-dimensional periodic arrays of nanospheres. *J. Phys. B At. Mol. Opt. Phys.* **38,** (2005).

63. Chu, Y., Schonbrun, E., Yang, T. & Crozier, K. B. Experimental observation of narrow

surface plasmon resonances in gold nanoparticle arrays. *Appl. Phys. Lett.* **93,** 2006–2009 (2008).

64. Auguié, B. & Barnes, W. L. Collective Resonances in Gold Nanoparticle Arrays. *Phys. Rev. Lett.* **101,** 143902 (2008).

65. Schmitt, M. & Popp, J. Raman spectroscopy at the beginning of the twenty-first century. *J. Raman Spectrosc.* **37,** 20–28 (2006).

66. Pettinger, B., Picardi, G., Schuster, R. & Ertl, G. Surface-enhanced and STM-tip-enhanced Raman spectroscopy at metal surfaces. *Single Mol.* **3,** 285–294 (2002).

67. Ru, E. C. Le & Etchegoin, P. G. *Principles of Surface-Enhanced Raman Spectroscopy and related plasmonic effects*. *Vasa* (2009). doi:10.1016/B978-0-444-52779-0.00003-9

68. Nie, S. Probing Single Molecules and Single Nanoparticles by Surface-Enhanced Raman Scattering. *Science (80-.).* **275,** 1102–1106 (1997).

69. Porter, M. D., Lipert, R. J., Siperko, L. M., Wang, G. & Narayanan, R. SERS as a bioassay platform: fundamentals, design, and applications. *Chem. Soc. Rev.* **37,** 1001 (2008).

70. Gopalakrishnan, A. *et al.* Nanoplasmonic structures for biophotonic applications: SERS overview. *Ann. Phys.* **524,** 620–636 (2012).

71. Kneipp, J., Kneipp, H., Wittig, B. & Kneipp, K. One- and Two-Photon Excited Optical pH Probing for Cells Using Surface-Enhanced Raman and. *Nano Lett.* **7,** 3–7 (2007).

72. Stuart, D. A. *et al.* In vivo glucose measurement by surface-enhanced Raman spectroscopy. *Anal. Chem.* **78,** 7211–7215 (2006).

73. O'Keefe, J. A. Resolving Power of Visible Light. *J. Opt. Soc. Am.* **46,** 359 (1956).

74. Ash, E. A. & Nicholls, G. Super-resolution aperture scanning microscope. *Nature* **237,** 510–512 (1972).

75. Kim, J. H. & Song, K. B. Recent progress of nano-technology with NSOM. *Micron* **38,** 409–426 (2007).

76. Zenhausern, F., Martin, Y. & Wickramasinghe, H. K. Scanning Interferometric Apertureless Microscopy: Optical Imaging at 10 Angstrom Resolution. *Science (80-.).* **269,** 1083–1085 (1995).

77. Zayats, A. V. *Nano Optics*.

78. Hillenbrand, R. & Keilmann, F. Complex optical constants on a subwavelength scale. *Phys. Rev. Lett.* **85,** 3029–3032 (2000).

79. Thackray, B. D. *et al.* Narrow Collective Plasmon Resonances in Nanostructure Arrays Observed at Normal Light Incidence for Simplified Sensing in Asymmetric Air and Water Environments. *ACS Photonics* **1,** 1116–1126 (2014).

80. Danilov, A. *et al.* Ultra-narrow surface lattice resonances in plasmonic metamaterial arrays for biosensing applications. *Biosens. Bioelectron.* **104,** 102–112 (2018).

81. Law, W.-C. *et al.* Wide dynamic range phase-sensitive surface plasmon resonance biosensor based on measuring the modulation harmonics. *Biosens. Bioelectron.* **23,** 627–632 (2007).

82. Nikitin, A. G., Kabashin, A. V & Dallaporta, H. Plasmonic resonances in diffractive arrays of gold nanoantennas: Near and far field effects. *Opt. Express* **20,** 27941–27952 (2012).

83. Zhou, W. & Odom, T. W. Tunable subradiant lattice plasmons by out-of-plane dipolar interactions. *Nat. Nanotechnol.* **6,** 423–427 (2011).

84. Zhou, W., Hua, Y., Huntington, M. D. & Odom, T. W. Delocalized lattice plasmon resonances show dispersive quality factors. *J. Phys. Chem. Lett.* **3,** 1381–1385 (2012).

85. Wang, D., Yang, A., Hryn, A. J., Schatz, G. C. & Odom, T. W. Superlattice Plasmons in Hierarchical Au Nanoparticle Arrays. *ACS Photonics* **2,** 1789–1794 (2015).

86. Kravets, V. G. *et al.* Graphene-protected copper and silver plasmonics. *Sci. Rep.* **4,** 1–8 (2014).

87. Quidant, R., Ren, B. & Sailor, M. J. Virtual Issue on Plasmonic-Based Sensing. *ACS Photonics* **4,** 2382–2384 (2017).

88. Mayer, K. M., Hafner, J. H. & Antigen, A. À. Localized surface plasmon resonance sensors. *Chem. Rev.* **111,** 3828–3857 (2011).

89. Zhang, L.-M. & Uttamchandani, D. Optical chemical sensing employing surface plasmon resonance. *Electron. Lett.* **24,** 1469 (1988).

90. Offermans, P. *et al.* Universal scaling of the figure of merit of plasmonic sensors. *ACS Nano* **5,** 5151–5157 (2011).

91. Li, Y. *et al.* Plasmonic induced triple-band absorber for sensor application. *Opt. Express* **23,** 17607 (2015).

92. Zeng, S. *et al.* Graphene-Gold Metasurface Architectures for Ultrasensitive Plasmonic Biosensing. *Adv. Mater.* **27,** 6163–6169 (2015).

93. Sheridan, A. K., Harris, R. D., Bartlett, P. N. & Wilkinson, J. S. Phase interrogation of an integrated optical SPR sensor. *Sensors Actuators, B Chem.* **97,** 114–121 (2004).

94. Patskovsky, S., Kabashin, A. V, Meunier, M. & Luong, J. H. T. Silicon-based surface plasmon resonance sensing with two surface plasmon polariton modes. *Appl. Opt.* **42,** 6905–6909 (2003).

95. Nemova, G., Kabashin, A. V. & Kashyap, R. Surface plasmon-polariton Mach-Zehnder refractive index sensor. *J. Opt. Soc. Am. B* **25,** 1673 (2008).

96. Danilov, A. *et al.* 3D plasmonic metamaterials for enhanced spectral sensitivity of optical nanosensors. in (eds. Vo-Dinh, T. & Lakowicz, J. R.) **10080,** 100800C (2017).

97. Danilov, A. *et al.* Phase singularities in 3D plasmonic crystal metamaterials for ultra-

sensitive biosensing. in *Proc. of SPIE Vol.* (eds. Geohegan, D. B., Dubowski, J. J. & Kabashin, A. V.) **10093,** 100930G (2017).

98. Aristov, A. I. *et al.* 3D plasmonic crystal metamaterials for ultra-sensitive biosensing. *Sci. Rep.* **6,** 25380 (2016).

99. Malinauskas, M., Farsari, M., Piskarskas, A. & Juodkazis, S. Ultrafast laser nanostructuring of photopolymers: A decade of advances. *Phys. Rep.* **533,** 1–31 (2013).

100. Kenanakis, G. *et al.* Three-dimensional infrared metamaterial with asymmetric transmission. *ACS Photonics* **2,** 287–294 (2015).

101. Ho, K. M., Chan, C. T. & Soukoulis, C. M. Existence of a photonic gap in periodic dielectric structures. *Phys. Rev. Lett.* **65,** 3152–3155 (1990).

102. Romanova, a. S., Korovin, a. V. & Romanov, S. G. Effect of dimensionality on the spectra of hybrid plasmonic-photonic crystals. *Phys. Solid State* **55,** 1725–1732 (2013).

103. Li, J., Hossain, M. M., Jia, B., Buso, D. & Gu, M. Three-dimensional hybrid photonic crystals merged with localized plasmon resonances. *Opt. Express* **18,** 4491–4498 (2010).

104. Kravets, V. G., Schedin, F. & Grigorenko, A. N. Plasmonic blackbody: Almost complete absorption of light in nanostructured metallic coatings. *Phys. Rev. B - Condens. Matter Mater. Phys.* **78,** 97–99 (2008).

105. Malassis, L. *et al.* Topological darkness in self-assembled plasmonic metamaterials. *Adv. Mater.* **26,** 324–330 (2014).

106. Luo, R. Effective medium theories for the optical properties of three-component composite materials. *Appl. Opt.* **36,** 8153–8 (1997).

107. Palik, E. D. *Handbook of Optical Constants of Solids*. *Journal of Modern Optics* (1998).

108. Shen, Y. *et al.* Plasmonic gold mushroom arrays with refractive index sensing figures of merit approaching the theoretical limit. *Nat. Commun.* **4,** 1–9 (2013).

109. Stewart, M. E. *et al.* Quantitative multispectral biosensing and 1D imaging using quasi-3D plasmonic crystals. *Proc. Natl. Acad. Sci.* **103,** 17143–17148 (2006).

110. Li, Y. *et al.* Surface plasmon coupling enhanced dielectric environment sensitivity in a quasi-three-dimensional metallic nanohole array. *Opt. Express* **18,** 3546–3555 (2010).

111. Viarbitskaya, S. *et al.* Tailoring and imaging the plasmonic local density of states in crystalline nanoprisms. *Nat. Mater.* **12,** 426–432 (2013).

112. Dickreuter, S. *et al.* Mapping of plasmonic resonances in nanotriangles. *Beilstein J. Nanotechnol.* **4,** 588–602 (2013).

113. Tabatabaei, M. *et al.* Optical properties of silver and gold tetrahedral nanopyramid

arrays prepared by nanosphere lithography. *J. Phys. Chem. C* **117,** 14778–14786 (2013).

114. Yurtsever, A. & Zewail, A. H. Direct visualization of near-fields in nanoplasmonics and nanophotonics. *Nano Lett.* **12,** 3334–3338 (2012).

115. Nelayah, J. *et al.* Mapping surface plasmons on a single metallic nanoparticle. *Nat. Phys.* **3,** 348–353 (2007).

116. Zenhausern, F., O'Boyle, M. P. & Wickramasinghe, H. K. Apertureless near-field optical microscope. *Appl. Phys. Lett.* **65,** 1623–1625 (1994).

117. Inouye, Y. & Kawata, S. Near-field scanning optical microscope with a metallic probe tip. *Opt. Lett.* **19,** 159 (1994).

118. Klar, T. *et al.* Surface-plasmon resonances in single metallic nanoparticles. *Phys. Rev. Lett.* **80,** 4249–4252 (1998).

119. Keilmann, F. & Hillenbrand, R. Near-field microscopy by elastic light scattering from a tip. *Philos. Trans. R. Soc. A Math. Phys. Eng. Sci.* **362,** 787–805 (2004).

120. Rang, M. *et al.* Optical near-field mapping of plasmonic nanoprisms. *Nano Lett.* **8,** 3357–63 (2008).

121. Esteban, R. *et al.* Direct Near-Field Optical Imaging of Hiher Order Plasmonic Resonances. *NanoLetters* **8,** 3155 (2008).

122. Hecht, B., Bielefeldt, H., Inouye, Y., Pohl, D. W. & Novotny, L. Facts and artifacts in near-field optical microscopy. *J. Appl. Phys.* **81,** 2492–2498 (1997).

123. Raschke, M. B. & Lienau, C. Apertureless near-field optical microscopy: Tip-sample coupling in elastic light scattering. *Appl. Phys. Lett.* **83,** 5089–5091 (2003).

124. Bek, A., Vogelgesang, R. & Kern, K. Optical nonlinearity versus mechanical anharmonicity contrast in dynamic mode apertureless scanning near-field optical microscopy. *Appl. Phys. Lett.* **87,** 1–3 (2005).

125. Novotny, L. From near-field optics to optical antennas. *Phys. Today* **64,** 47–52 (2011).

126. Kim, D.-S. & Kim, Z. H. Polarization-Selective Imaging of the Enhanced Local Field at Gold Nanoparticle Junctions. *J. Korean Phys. Soc.* **52,** 17–20 (2008).

127. Halas, N. J., Lal, S., Chang, W. S., Link, S. & Nordlander, P. Plasmons in strongly coupled metallic nanostructures. *Chemical Reviews* **111,** 3913–3961 (2011).

128. Pettinger, B. Single-molecule surface- and tip-enhanced raman spectroscopy. *Mol. Phys.* **108,** 2039–2059 (2010).

129. Lombardi, J. R. & Birke, R. L. The theory of surface-enhanced Raman scattering. *J. Chem. Phys.* **136,** (2012).

130. Le Ru, E. C. & Etchegoin, P. G. Quantifying SERS enhancements. *MRS Bull.* **38,** 631–640 (2013).

131. Kneipp, K. *et al.* Population Pumping of Excited Vibrational States by Spontaneous Surface-Enhanced Raman Scattering. *Phys. Rev. Lett.* **76,** 2444–2447 (1996).

132. Le Ru, E. C., Etchegoin, P. G. & Meyer, M. Enhancement factor distribution around a single surface-enhanced Raman scattering hot spot and its relation to single molecule detection. *J. Chem. Phys.* **125,** 1–13 (2006).

133. Kneipp, K. *et al.* Single Molecule Detection Using Surface-Enhanced Raman Scattering (SERS). *Phys. Rev. Lett.* **78,** 1667–1670 (1997).

134. Fang, Y., Seong, N.-H. & Dlott, D. D. Measurement of the distribution of site enhancements in surface-enhanced Raman scattering. *Science* **321,** 388–392 (2008).

135. Le Ru, E. & Etchegoin, P. *Principles of Surfance Enhanced Raman Spectroscopy and related plasmonic effets*. *Elsevier* **1,** (2009).

Résumé

Cette thèse considère de nouvelles architectures prometteuses des métamatériaux plasmoniques pour biosensing, comprenant: (I) des réseaux périodiques 2D de nanoparticules d'Au, qui peuvent supporter des résonances des réseaux de surface couplées de manière diffractive; (II) Reseaux 3D à base de cristaux plasmoniques du type d'assemblage de bois. Une étude systématique des conditions d'excitation plasmonique, des propriétés et de la sensibilité à l'environnement local dans ces géométries métamatérielles est présentée. On montre que de tels réseaux peuvent combiner une très haute sensibilité spectrale (400 nm / RIU et 2600 nm / RIU, ensemble respectivement) et une sensibilité de phase exceptionnellement élevée (> 10^5 deg./RIU) et peuvent être utilisés pour améliorer l'état actuel de la technologie de biosensing the-art. Enfin, on propose une méthode de sondage du champ électrique excité par des nanostructures plasmoniques (nanoparticules uniques, dimères). On suppose que cette méthode aidera à concevoir des structures pour SERS (La spectroscopie du type Raman à surface renforcée), qui peut être utilisée comme une chaîne d'information supplémentaire à un biocapteur de transduction optique.

Mots-clés: biocapteurs plasmoniques, métamatériaux plasmoniques, PSLR, SPP, LSPR, SERS, aSNOM

Abstract

This thesis consideres novel promissing architechtures of plasmonic metamaterial for biosensing, including: (I) 2D periodic arrays of Au nanoparticles, which can support diffractively coupled surface lattice resonances; (II) 3D periodic arrays based on woodpile-assembly plasmonic crystals, which can support novel delocalized plasmonic modes over 3D structure. A systematic study of conditions of plasmon excitation, properties and sensitivity to local environment is presented. It is shown that such arrays can combine very high spectral sensitivity (400nm/RIU and 2600 nm/RIU, respectively) and exceptionally high phase sensitivity (> 10^5 deg./RIU) and can be used for the improvement of current state-of-the-art biosensing technology. Finally, a method for probing electric field excited by plasmonic nanostructures (single nanoparticles, dimers) is proposed. It is implied that this method will help to design structures for SERS, which will later be used as an additional informational channel for biosensing.

Keywords: plasmonic biosensors, plasmonic metamaterials, Plasmonic Surface Lattice Resonances, Surface Plasmon Resonance, Localized Surface Plasmon Resonance, Surface Enhanced Raman Spectroscopy, apertureless Scanning Near-filed Optical Microscopy